ACERP
Advanced Ceramics Progress

ISSN 2423-7477
e-ISSN 2423-7485

Advanced Ceramics Progress

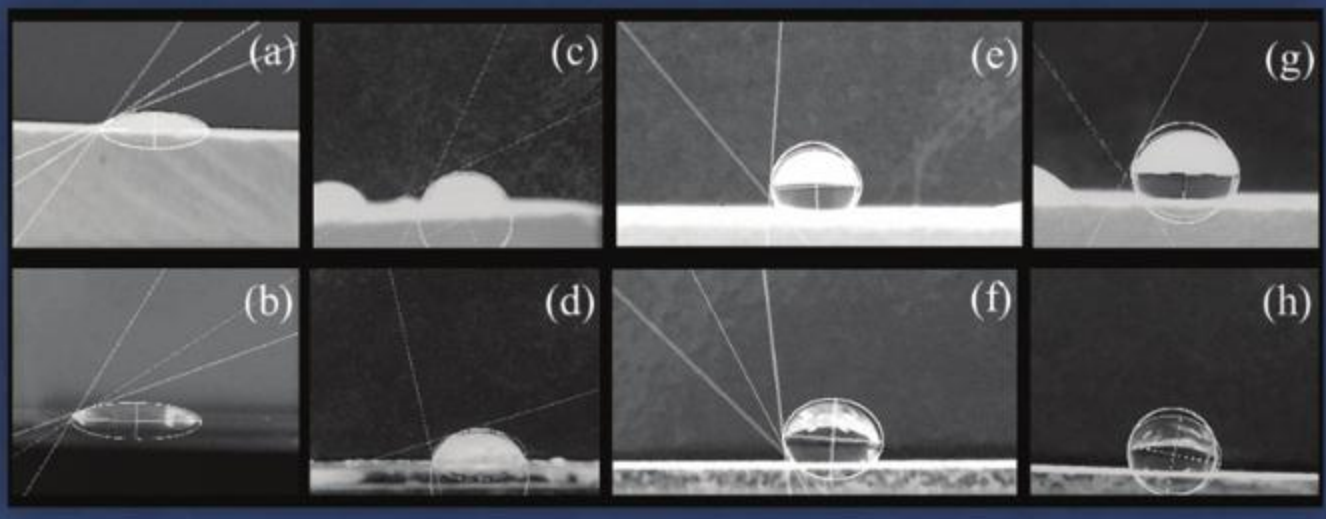

Materials and Energy
Research Center

Iranian Ceramic Society

In The name of God

Advanced Ceramics Progress

Advanced **Cer**amics **P**rogress (ISSN 2423-7477) (e-ISSN 2423-7485)

Web Site: www.acerp.ir, E-mail: office@acerp.ir
Tel: +98 (0) 26 36280040-7 ext.: 173, Fax: +98 (0) 26 36201888
Tel:+98 (0)21 88771626-7 ext.: 8931, Fax: +98 (0)21 88773352

Materials and Energy Research Center (MERC); Iranian Ceramic Society (ICERS)

AIMS AND SCOPE

Advanced Ceramics Progress (ACERP) as an ISC international journal is devoted to elucidating the fundamental aspects of chemistry and physics occurring at a wide range of oxide and nonoxide ceramics and composite materials and their processing, microstructure, properties, and applications. The journal provides a unique venue for publishing new exciting research, focusing on dynamic growth areas in this field.

INSTRUCTIONS FOR AUTHORS

Submission of manuscript represents that it has neither been published nor submitted for publication elsewhere and is result of research carried out by author(s).
Authors are required to include a list describing all the symbols and abbreviations in the paper. Use of the international system of measurement units is mandatory.

- On-line submission of manuscripts results in faster publication process and is recommended. Instructions are given in the ACERP web site: www.acerp.ir
- Hardcopy submissions must include MS Word and jpg files.
- Manuscripts should be typewritten on one side of A4 paper, double-spaced, with adequate margins.
- References should be numbered in brackets and appear in sequence through the text. List of references should be given at the end of the paper.
- Figures' captions are to be indicated under the illustrations. They should sufficiently explain the figures.
- Illustrations should appear in their appropriate places in the text.
- Tables and diagrams should be submitted in a form suitable for reproduction.
- Photographs should be of high quality saved as jpg files.
- Tables, illustrations, figures and diagrams will be normally printed in single column width (8 cm). Exceptionally large ones may be printed across two columns (17 cm).

PAGE CHARGES AND REPRINTS

ACERP subscribers do not need to make any payment for publication and reprints.

AUTHORS CHECKLIST

- Author(s), bio-data including affiliation(s) and mail and e-mail addresses.
- Manuscript including abstract, key words, illustrations, tables, figures with figures' captions and list of references.
- MS Word files of the paper.

Advanced **Cer**amics **P**rogress,
P.O. Box 31787-316, Karaj, Alborz, I. R. Iran
Materials and Energy Research Center, Imam Khomeini Blvd, Meshkin Dasht, Karaj, Alborz, I. R. Iran
P.O. Box 14155-4777, Tehran, I. R. Iran
No. 5, Ahuramazda St., Alvand Ave., Argentine Sq., Tehran, I. R. Iran

www.merc.ac.ir - www.acerp.ir

ISSN: 2423-7477; e-ISSN: 2423-7485

Advanced Ceramics Progress: Vol. 9, No. 3, (Summer 2023) 1-56

CONTENTS

Advanced Ceramics Progress: Vol. 9, No. 3, (Summer 2023) 1-15

Materials and Energy Research Center
MERC

Contents lists available at ACERP

Advanced Ceramics Progress

Journal Homepage: www.acerp.ir

Original Research Article

Investigating the Role of Pouring Temperature, Heat Treatment and Mold Preheating Temperature on the Hardness and Microstructure of the Inner Surface of Al-15Mg_2Si In Situ Composite Pipe Fabricated by Centrifugal Casting Method

Ali Zeinali [a]*, Masoud Rajabi [b], Mohammad Reza Rahimipour [c], Mohsen Ostad Shabani [d]

[a] *PhD Student, Department of Materials Engineering, Faculty of Engineering, Imam Khomeini International University (IKIU), Qazvin. Iran.*
[b] *Associate Professor, Department of Materials Engineering, Faculty of Engineering, Imam Khomeini International University (IKIU), Qazvin, Iran.*
[c] *Professor, Department of Ceramic, Materials and Energy Research Center, Karaj, Iran.*
[d] *Assistant Professor, Department of Ceramic, Materials and Energy Research Center, Karaj, Iran.*

* Corresponding Author Email: AliZeinali45582@gmail.com (Mohammad Almasi Kashi) URL: https://www.acerp.ir/article_181826.html

ARTICLE INFO

Article History:

Received 20 June 2023
Received in revised form 28 October 2023
Accepted 10 September 2023

Keywords:

Solidification,
Alloy,
Reinforcement,
Optimization,
Design Expert

ABSTRACT

This study aims to place Mg_2Si reinforcing particles in the inner wall of aluminum matrix composite tube and optimize the microstructure and hardness of the mentioned wall using temperature parameters. Upon application of Al-Si alloy, creation of in-situ Mg_2Si particles in this alloy system, and production of the pipe as a result of the low density of Mg_2Si particles based on the centrifugal casting method, these reinforcing particles would be accumulated in the inner wall of the pipe. In this study, the effect of dissolution, aging, mold preheating, and pouring temperature on the hardness of the inner wall of Al-15 wt. % Mg_2Si alloy was investigated, and the most optimal manufacturing conditions as well the interaction among the variables were determined using Design Expert software to achieve the highest hardness. Of note, the most effective variable among the mentioned variables was heat treatment temperature, and the best temperature was about 535 °C. According to the findings, the best pouring temperature was obtained as around 700 °C; hence, a higher temperature is needed to preheat the mold to obtain reinforcement with uniform placement.

https://doi.org/10.30501/acp.2023.403234.1127

1. INTRODUCTION

Compared to the ordinary alloys and unreinforced materials, composite materials have significant features owing to which, application of these advanced materials in different industries has increasingly grown. The main objectives of the developing composite materials can be summarized as follows: reducing the weight, elevating the strength-to-weight ratio, enhancing the elastic modulus, decreasing the thermal expansion coefficient as well as improving the thermal shock resistance, yield strength, creep resistance at high temperatures, fatigue properties at high temperature, and wear properties. Composites have a combination of properties that do not exist in metal, ceramic, and polymer materials alone;

Please cite this article as: Zeinali, A., Rajabi, M., Rahimipour, M.R., Ostad Shabani, M., "Investigating the Role of Pouring Temperature, Heat Treatment and Mold Preheating Temperature on the Hardness and Microstructure of the Inner Surface of Al-15Mg_2Si In Situ Composite Pipe Fabricated by Centrifugal Casting Method", ***Advanced Ceramics Progress***, Vol. 9, No. 3, (2023), 1-15. https://doi.org/10.30501/acp.2023.403234.1127

therefore, composites give us design power and this feature makes them unique.

The in-situ process is one of the common methods for producing cast aluminum matrix composites, which is thermodynamically stable where the reinforcing phase is basically formed in situ from the matrix by germination and growth. Special attention has been paid to these composites in recent years owing to their stable interface, ease of production, diverse mechanical properties, and low price. Unlike non-in-situ methods that always face problems such as non-wetting of reinforcing particles, control of the interface between particles and the ground, improper distribution of the particles, and agglomeration of the reinforcing particles, the in-situ method creates stable interfaces between the particles and the ground while its properties are mechanically suitable, and the manufacturing method is also simple [1].

1.1. Introduction of Al-Mg2Si Composite

Aluminum alloys are the most widely used light materials for use in the automotive industry to lighten the weights, enhance efficiency in fuel consumption, and reduce CO_2 gas. In the last 50 years, the amount of using aluminum alloys and other light alloys in different industrial applications has notably increased. Significant amounts and types of aluminum alloys are commonly used in the automotive industry in different parts such as engine cylinders, body, chassis, manifold, wheels, and decor. Due to the decrease and limitations in energy resources and the increase in the consumption of goods and energy in the world today, increasing applications of aluminum alloys owing to their lightweight and easy production and shaping (compared to other metals such as steel) in industries have gained more significance than before. In general, efficiency enhancement of aluminum alloys is classified into two groups: 1) increasing productivity by controlling the production process and 2) increasing productivity by improving the alloy characteristics. Al-Si alloys with a high percentage of Mg are cast-in-situ composites that have an Al matrix and hard Mg_2Si particles as the reinforcement. The Al-Mg_2Si alloys enjoy several advantages such as uniform distribution of reinforcing phase, high wettability of particles, and low cost of production that make them very suitable alternatives to the Al-Si alloys used in aerospace and automotive industries and other industries as well. Among the reinforcing materials that are used in the form of particles in metal-based composites, Mg_2Si has the lowest density; hence, it has a high potential to be used as a reinforcement in aluminum-based composites to reduce weight. In addition, the Mg_2Si compound is a semiconductor that has an FCC structure with lattice parameter a=0.6351 nm. This intermetallic composition is characterized by the melting temperature of 1083°C, density of $99.1*10^3$ Kg m^{-3}, high hardness value of 4500 NMm^{-2}, low thermal expansion coefficient of 7.5*10-6 k^{-1}, and relatively high elastic modulus of 120 GPa. It should be noted that in terms of properties and freezing behavior, there are many similarities between Mg_2Si and Si and between Al-Mg_2Si and Al-Si systems as well [2].

1.2. Centrifugal Casting

One of the new methods for shaping materials is centrifugal casting, which has been effectively used in different industries. In this method that functions based on the application of centrifugal force, the mold is movable and rotating, and the melt is added to it during the rotation of the mold which is generally made of steel, graphite, and stainless steel. This method is employed to produce a variety of parts such as all types of gas and water lines pipes, annular parts, pipe wall insulation, engine cylinders, pistons, train wheels, etc. In this method, the force is more concentrated in the outer wall part and by moving towards the inner wall, the centrifugal force is reduced, which leads to the accumulation of heavier particles in the outer wall and tendency of the lighter particles to be accumulated in the inner part of the final piece. The advantages of this method compared to the traditional casting method are briefly listed as follows: high manufacturing speed; high quality of the final part in terms of dimensional accuracy, suitable final surface, and low porosity on the surface; fast freezing with high metallurgical quality; and simple method as well as low machining required.

Upon using Al-Si alloy, creating in-situ Mg_2Si particles in this alloy system, and producing pipes through centrifugal casting method, these reinforcing particles will be accumulated in the inner wall of the pipe due to the low density of Mg_2Si particles. The tribological properties of the inner wall of the pipe could be improved by optimizing the microstructure and morphology of Al-Mg_2Si with additives and heat treatment cheaply and efficiently [3].

All metals capable of static casting can benefit from centrifugal casting for manufacturing; for example, alloy and carbon steels, heat and corrosion-resistant steels, gray cast iron, steel with a high percentage of alloy elements, non-ferrous metals, as well as non-metallic materials such as ceramics, glass, plastics and in general, any material that turns into a liquid phase can be manufactured based on this method [4]. In the centrifugal casting process, the fluidity behavior of the melt plays an important role in determining the quality of the final product. Viscosity is one of the important physical characteristics of the melt, which has an important effect on the flow behavior of the melt as well as the flow patterns inside the mold [5]. Many parameters are effective in the centrifugal casting process, including melt temperature, mold temperature, mold thermal conductivity, mold rotation speed, mold size, temperature and loading time in the mold, to name a few [6]. The rotation speed of the mold is one of the most important influencing parameters, which is directly related to the freezing speed of the molten metal. When

the cylindrical mold is filled by the melt at different speeds, different flow patterns namely Ekman, Cote, and Taylor flows are formed [7]. The solidification rate of the molten metal in centrifugal casting is of high importance because of its great impact on the determination of mechanical and microstructural properties. The solidification rate of pure metal in centrifugal casting is measured by grain size and in Al-Si alloys by Secondary Dendritic Arm Spacing (SDAS). Areas with higher solidification speed have small equiaxed grains while areas with lower solidification speed have grains with higher roughness than others [8].

Zhai et al. [۹] employed the centrifugal casting method to create an FGM composite reinforced with in-situ particles of Mg2Si and added Si to increase the hardness of the pipe's inner wall. The results showed that with the accumulation of Mg_2Si and Si particles in the inner wall, the hardness improved significantly.

1.3. Mold Rotation Speed

An important factor in centrifugal casting is to maintain the inner circular shape against gravity, longitudinal tearing, and stresses during rapid solidification of the molten metal against the mold surface. Compared to other parameters, the mold rotation speed is the main and most influential parameter affecting the solidification rate and particle distribution in alloys under centrifugal force.

Upon increasing the rotation speed of the mold, the shrinkage defect decreases while the tensile strength increases [10]. As the mold rotation speed increases, the thickness of the Mg_2Si-rich layer decreases, but the volume fraction of the Mg_2Si-rich layer increases, and the segregation of reinforcement particles intensifies [11]. Arefkhani et al. investigated the effect of mold rotation speed on the microstructure and hardness of Al-WC composite made by the centrifugal casting method. The best rotation speed of the mold for proper positioning of the reinforcement and creating the highest hardness was determined to be 1500 rpm [۱۲]. Nirumand et al. investigated the effect of mold rotation speed on the hardness and mechanical properties of Al-15 wt. %Mg_2Si alloy made by centrifugal casting method. Upon increasing the mold rotation speed, the thickness of the area containing the reinforcement decreased while its compression and hardness increased [۱۳].

1.4. Pouring Temperature

If the temperature of the molten metal or its fluidity is too high, the molten metal will not reach the speed of the mold quickly and the solidification time will also increase. Changing the pouring temperature affects the microstructure and distribution of particles in the casting. Low melt temperatures lead to maximum grain refinement and coaxial structures while higher temperatures promote columnar growth in many alloys. However, it should be noted that scientific considerations limit the used temperature range. Increasing the pouring temperature causes an increase in the grain Size and Dendritic Arm Distance (SDAS), particle separation, and solidification time. The pouring temperature must be high enough to satisfactorily flow the metal while avoiding the formation of rough structures and the increased risk of hot tearing due to overheating.

Morgan et al. [۱۴] investigated the effect of centrifugal casting parameters on the microstructure of Al-SiC composite. The results showed that increasing the pouring temperature leads to the production of denser pieces with better mechanical properties. Slower metal feeding speed and mold rotation speed reduce heat accumulation and metal volume before solidification.

Different factors were found to be effective in the separation of particles and their distribution in the part obtained from centrifugal casting including the pouring temperature, mold temperature, and G number ($G=\omega^2 R/g$ where R is the radius of the tube in meters, ω the rotation speed of the mold in revolutions per second, and g the centrifugal force). At the pouring temperature of 720 °C, mold temperature of 90 °C, and G > 60, the reinforcement particles accumulate in the inner layer. However, under the same conditions except for G < 40, the reinforcement layer is not formed, and the particles are spread on the cross-section [۱۵].

Increasing the pouring temperature leads to an improvement in the tensile strength and reduction in both hardness and tribological properties [۱۶].

Asan et al. [۱۷] investigated the effect of mold preheating temperature, pouring temperature, and pouring height on the mechanical properties of $Al_{12}Si$ alloy. According to their results, the most important parameters involved in their test were the pouring temperature, pouring height, and mold preheating temperature. The results showed that increasing the pouring temperature and decreasing the pouring height play a key role in maintaining the fluidity of the melt and better filling the mold and the properties of the final part.

Yisi et al. [۱۸] investigated the effect of pouring temperature on the microstructure of Al-5 wt. % Mg_2Si semi-solid hypoeutectic composite. The results showed that lowering the pouring temperature improved both α-Al structure and eutectic cell (α-Al+Mg_2Si) and reduced the formation of dendritic phases.

1.5. Mold Temperature

The temperature of the mold is an important parameter that affects the heat transfer rate of the melt and consequently the freezing rate in centrifugal casting. A change in the freezing speed causes a change in the mechanical properties of the centrifugal casting parts. At high freezing speeds, the possibility of creating shrinkage porosity becomes more than usual. On the contrary, when freezing happens gradually, the possibility of creating shrinkage porosity decreases. For this purpose, it is recommended to preheat the centrifugal casting molds up

to a higher temperature range.

1.6. Heat Treatment Of Aluminum Alloys

The dissolution operation is normally performed at a high temperature close to the eutectic temperature of the alloy, which can homogenize the casting microstructure, dissolve intermetallics such as Al_2Cu, Mg_2Zn, and Mg_2Si, and make the eutectic Si spherical [۱۹-۲۰]. In Al-Si-Mg alloys, Mg_2Si dissolves easily due to the high penetration rate of magnesium in aluminum while the microstructure and amount of magnesium affect the dissolution process [۱۹,۲۱].

Zedi et al. [۲۲] performed the dissolution operation at 520 °C for 6 hours and aging operation at 200 C for 6 hours in Al-10 wt. % Mg_2Si alloy. They reported the formation of the Mg_2Si phase from long rods to pseudo-short and spherical fibers changed shape. In a study, the effect of heat treatment on the morphology of primary and eutectic Mg_2Si was investigated. The results showed that the initial Mg_2Si morphology did not change much with the increase in the heat treatment temperature. In addition, since the penetration started from these areas into the background, the sharp corners were rounded and the eutectic Mg_2Si network was partially broken.

After the dissolution operation for 6 hours at 520 °C and 6 hours of aging at 200 °C, the morphology of eutectic Mg_2Si changed from long rods to short and round fibers. Moreover, the morphology of a part of eutectic Mg_2Si became spherical and crushed and the tensile strength improved by 26 % compared to the state without heat treatment.

2. MATERIALS AND METHODS

Figure 1 shows the flow chart of this research.

2.1. Primitive Material

In this research, Iralco pure aluminum ingot with 99.85% purity, magnesium ingot with 99.8% purity, and silicon with 99% purity were used to make Al-15%wt Mg_2Si in-situ composite.

2.2. Composite Manufacturing Method

To make Al-15%wt Mg_2Si (Al-9.5 Mg-5.5 Si) composite, aluminum was first melted in an induction furnace at 700 °C and then, the preheated silicon and magnesium pieces were added to it and kept at this temperature for 15 minutes. Next, it was molded and cooled down by room temperature. To make 2 Kg of this alloy, 1750 g of aluminum, 200 g of magnesium (including waste), and 115 grams of silicon are required. Due to the creation of a vortex in the casting in the induction furnace, there is no need to stir the resulting alloy.

To check the microstructure of the resulting alloy and ensure the proper formation of Mg_2Si as well as the absence of iron in the aluminum background, the obtained alloy was sampled, polished, and etched.

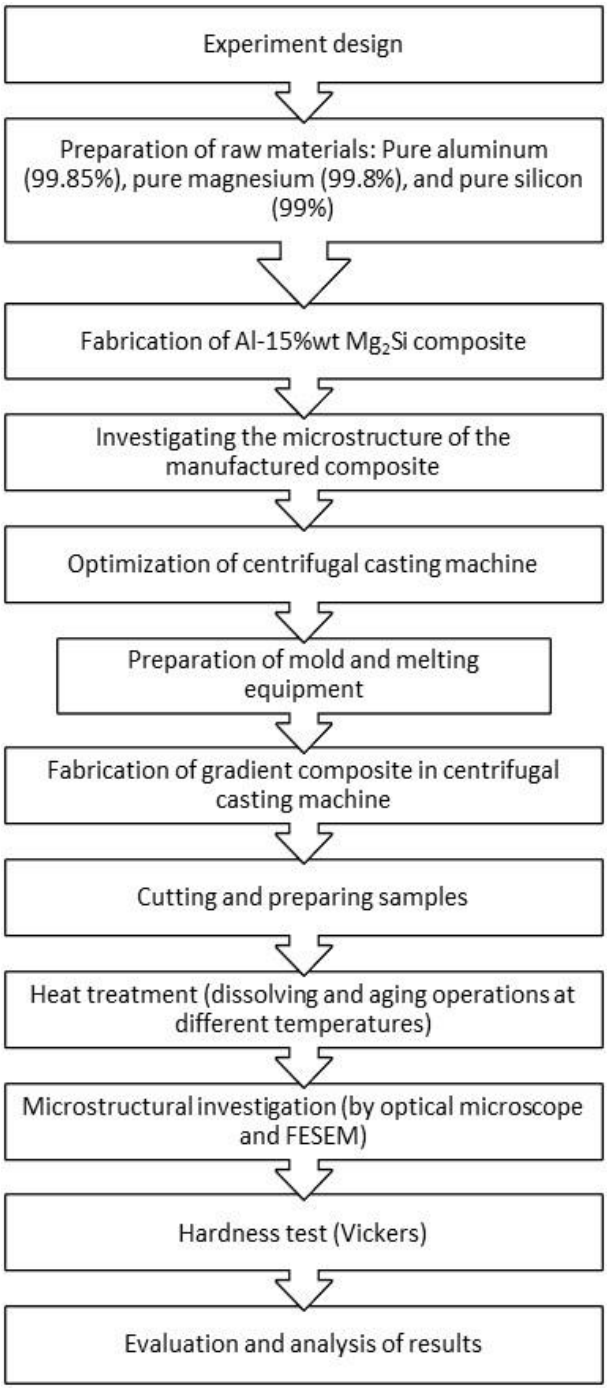

Figure 1. The flowchart of the path of this research

Finally, the prepared samples were examined by an optical microscope. The resulting alloy was used in centrifugal casting and remelted. For this purpose, a vertical centrifugal casting machine with the rotation speed of 1500 rpm was used. Followed by preheating the mold (at two temperatures of 150 and 300 °C), the said melt was cast at different pouring temperatures inside the rotating mold.

2.3. Construction Equipment

2.3.1. Induction Furnace

To make Al-15 wt. % Mg_2Si composite and to remelt the alloy for use in the centrifugal machine and tube forming, a medium frequency induction furnace was used.

2.3.2. Centrifugal Casting Machine

The mold of the device is made of cast iron with the inner diameter of 5 cm and length of 12 cm. The end of the mold was blocked by a cap with a muscle. A 1 HP single-phase electric motor was used to create rotational movement in the mold. To control the rotation speed of the mold, changing the ratio of the pulleys of the motor head and the shaft was used. The mold rotation speed can be calculated using Equation (1) [٢٣].

$$N2 = N1 * D1/D2 \quad (1)$$

In Equation (1), N1 is the nominal speed of the motor (inserted on the electric motor), D1 the diameter of the motor, D2 the diameter of the motor installed on the mold shaft, and N2 the rotation speed of the mold.

Given that the desired rotation speed of the mold was considered fixed in this research and according to the nominal speed of the machine (900 rpm), two 6 and 10 cm pulleys were used to achieve the rotation speed of 1500 rpm. Figure 2 shows the image of the centrifugal casting machine used in this research.

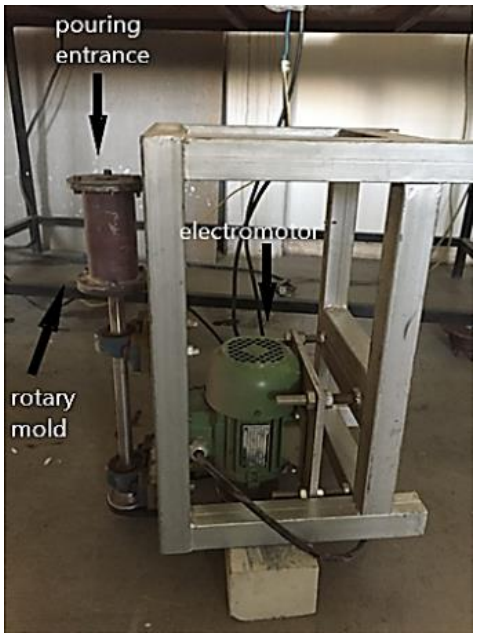

Figure 2. Side view of the centrifugal casting machine

2.3.3. Cutting Samples

To prepare the samples for the hardness test as well as microstructural investigations, it was necessary to prepare the inner surface of the composite pipes, which was done by cutting the samples with a band saw in larger dimensions and then sizing the samples with a grinding stone.

2.4. Preparation of Samples for Metallography

For this purpose, heat-treated samples are prepared at different temperatures and after that, sanding papers from P-80 to P-1500 were used to observe the microstructure by optical microscope and Scanning Electron Microscope (SEM). Polishing the samples was done using coarse sandpaper under water flow and was continued until the softest sandpaper. After changing each sandpaper, the sample was rotated 90 degrees. As the sandpaper became softer, the pressure applied to the samples on the polishing machine decreased, and this continued until the last deep scratches on the samples disappeared. Finally, to polish the surface of the samples, the samples were polished with felt and aluminum oxide on the polishing machine.

To observe the morphologies of the Mg_2Si particles and Mg_2Si phase in the alloy based on the characteristics of the Al-15 wt. % Mg_2Si alloy and that of the Mg_2Si phase, there was a need for deep etching. For this purpose, the samples were deeply etched in an aqueous solution containing 10% by weight of sodium hydroxide (NaOH) for 8 minutes [٢٤]. After that, the samples were washed with 90% ethanol and dried with a hair dryer.

2.5. Preparing the Mount

The shape and size of the pieces cut from the pipe were taken into account while carrying out the hardness test on the samples at ambient temperature, hence inevitable use of mounts. For this purpose, epoxy resin and hardener were used at the ratio of 2:1. After stirring for 5 minutes, this mixture was poured into a mount mold and heated at 70°C for further 30 minutes to solidify.

2.6. Equipment for Analyzing and Checking Mechanical Properties

After preparing the samples in the metallography laboratory, the microstructure of the composite was examined by an optical microscope. The samples were examined from 50 to 500 times magnification. Also, the cross-section of the samples was examined in terms of the thickness from the outer wall to the inside, and the distribution of the reinforcing phase (Mg_2Si) along the thickness was examined and photographed. Further, Image J software was used to measure different phases and microstructure measurements.

2.7. Field Emission Microscope (FESEM)

The field emission microscope device of Razi Metallurgy Research Institute was used due to its high resolution and quality that make it suitable to investigate the morphology of the reinforcement. The EDX analysis was also used to check the chemical composition of the

surface of the parts.

2.8. Design expert software

Design Expert is a test design and results analysis software that works with the response surface method and provides powerful tools to ideally test your process, mixture, or combination of factors and components. The matching of the experimental and predicted results is done by ANOVA analysis and at the end, the prediction equations of the results can be extracted. Design Expert 10 software was also utilized in this study to design the experiment and analyze the results.

Akbarpour et al. investigated and optimized the hardness of Cu/SiC composite using the RSM method, and their experimental results were in good agreement with the predicted results [۲۵].

3. RESULTS AND DISCUSSION

Figure 3 shows the cross-section of the sample along the thickness. As shown in this figure, the Al-15 wt. % Mg_2Si gradient composite was successfully fabricated through the centrifugal casting method, and the reinforcing particles were placed in the inner wall of the cylinder. According to the deep etching and in order to determine the morphology of the reinforcement, the middle parts that contain the aluminum matrix and are empty of the reinforcement are corroded by the etching solution. These parts in this figure are depicted in dark color, showing the accumulation of the reinforcement in a dense manner in the inner wall.

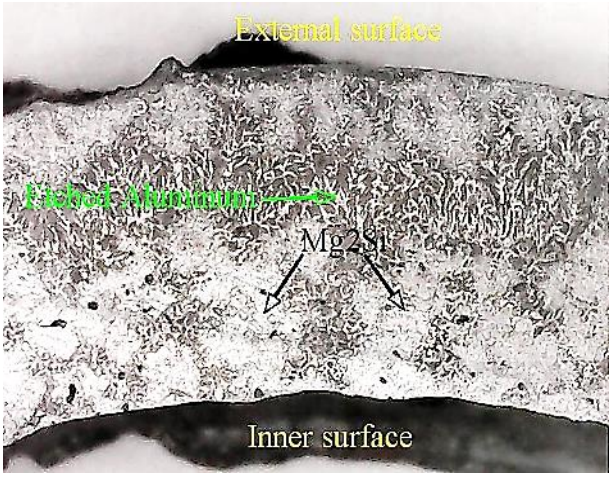

Figure 3. Image of a cross-section of the cylinder along the thickness of Al-15 wt. % Mg_2Si composite

The design of the experiment was done using Design Expert 10 software and based on the Central Composite Design mode, the variables and levels of which are listed in Table 1. It should be noted that the tests were performed in two blocks with preheated molds at two different temperaturees.

TABLE 1. Table of variables and levels of each variable

Name	units	Low	High	-alpha	+alpha
melt T	°C	650	750	600	800
heat treatment T	°C	500	570	465	605
Aging T	°C	170	210	150	230

The design table of the conducted tests is according to Table 2.

TABLE 2. Test design table and results

Std	Block	Run	Factor 1 B: Melt T °C	Factor 2 D: Heat Treat. T °C	Factor 3 E: Aging T °C	Response Hardness HV
1	300C (Block 1)	1	650	500	210	101
2	300C (Block 1)	14	650	500	170	77
3	300C (Block 1)	9	750	500	170	132
4	300C (Block 1)	4	750	500	210	103
5	300C (Block 1)	18	650	500	170	78
6	300 C (Block1)	24	650	500	210	100
7	300C (Block 1)	15	750	500	210	106
8	300C (Block 1)	5	750	500	170	125
9	300C (Block 1)	13	650	570	170	120
10	300C (Block 1)	19	650	570	210	127
11	300C (Block 1)	21	750	570	210	96
12	300C (Block 1)	23	750	570	170	100
13	300C (Block 1)	16	650	570	210	128
14	300C (Block 1)	17	650	570	170	115
15	300C (Block 1)	7	750	570	170	105
16	300C (Block 1)	20	750	570	210	96
17	300C (Block 1)	22	700	535	190	104
18	300C (Block 1)	8	700	535	190	104
19	300C (Block 1)	11	700	535	190	108
20	300C (Block 1)	3	700	535	190	105
21	300C (Block 1)	10	700	535	190	104
22	300C (Block 1)	2	700	535	190	104
23	300C (Block 1)	6	700	535	190	103
24	300C (Block 1)	12	700	535	190	100
25	150C (Block 2)	32	700	535	190	102
26	150C (Block 2)	33	700	535	190	103
27	150C (Block 2)	35	800	535	190	71
28	150C (Block 2)	25	800	535	190	71
29	150C (Block 2)	34	700	535	190	104
30	150C (Block 2)	31	700	535	190	104
31	150C (Block 2)	27	700	465	190	98
32	150C (Block 2)	29	700	535	150	101
33	150C (Block 2)	30	700	535	230	103
34	150C (Block 2)	28	700	535	190	97
35	150C (Block 2)	26	700	535	190	97

As observed in Table 2, 35 samples were made with different levels of variables, and the hardness of each sample was measured. It should be noted that the accuracy and correctness of the results were checked using ANOVA, and the predicted results matched the experimental results by 89.9 %. The final equation (Equation 2) is used to predict the results for hardness and is shown in the following:

Hardness = (2)
-4246.32931
+9.15665 * melt T
+2.84456 * heat treatment T
+4.10392 * aging T
-7.25000E-003 * melt T * heat treatment T
-7.93750E-003 * melt T * aging T
-2.67856E-003 * melt T^2
+2.19494E-003 * heat treatment T^2
+3.87126E-003 * aging T^2

Figures 4-8 demonstrate the cross-sectional images of the samples along the thickness with different pouring temperatures. At four pouring temperatures (650, 700, 750, and 800 °C), the samples were made with a mold preheat temperature of 300 °C, and a series of samples were made according to the test design (pouring temperature 700 °C) in a mold with the preheating temperature of 150 °C. On the outer surface of the samples, as expected, there is a small amount of reinforcement, and the presence of small amounts of reinforcement in the outer wall is the result of the recoil of the reinforcement particles caused by the melt turbulence and collision with heavier particles such as excess silicon. During the rotation of the mold, several Mg_2Si particles are directed to the outer wall, and another reason is the limited time of the reinforcement (low freezing range) to move in the melt and reach the inner wall due to rapid freezing. The points close to the mold have the highest freezing speed, thus limiting the time for the movement of the reinforcement, which is why there are more amounts of reinforcement in the outer wall in the sample with the pouring temperature of 650 °C. As we move towards the inner wall of the tube, the amount of reinforcement increases, which are mainly primitive Mg_2Si particles. The reason for the presence of more reinforcing particles in the form of primary Mg_2Si is because during freezing, the first phase that germinates is primary Mg_2Si, which kinetically has enough time to germinate and be placed in the inner wall. In Figures 5, 6, and 7, the pouring temperature ranges from 700 to 750 °C, which provides more opportunity for the reinforcement to move in the melt and reach the inner wall during freezing due to the higher fluidity and greater freezing range. In Figure 8, with an increase in the pouring temperature up to 800 °C, the particles in the inner wall will not be well distributed mainly due to the high fluidity of the melt as well as the reduction of friction between the melt and the mold. This prevents the speed of the melt from reaching the speed of the mold in a short time, and the centrifugal force does not play a role well during freezing. As a result, the reinforcement is not placed well in the inner wall [۲۶]. In addition, the clustering of the reinforcing particles is evident, which originates from the high temperature of the pour.

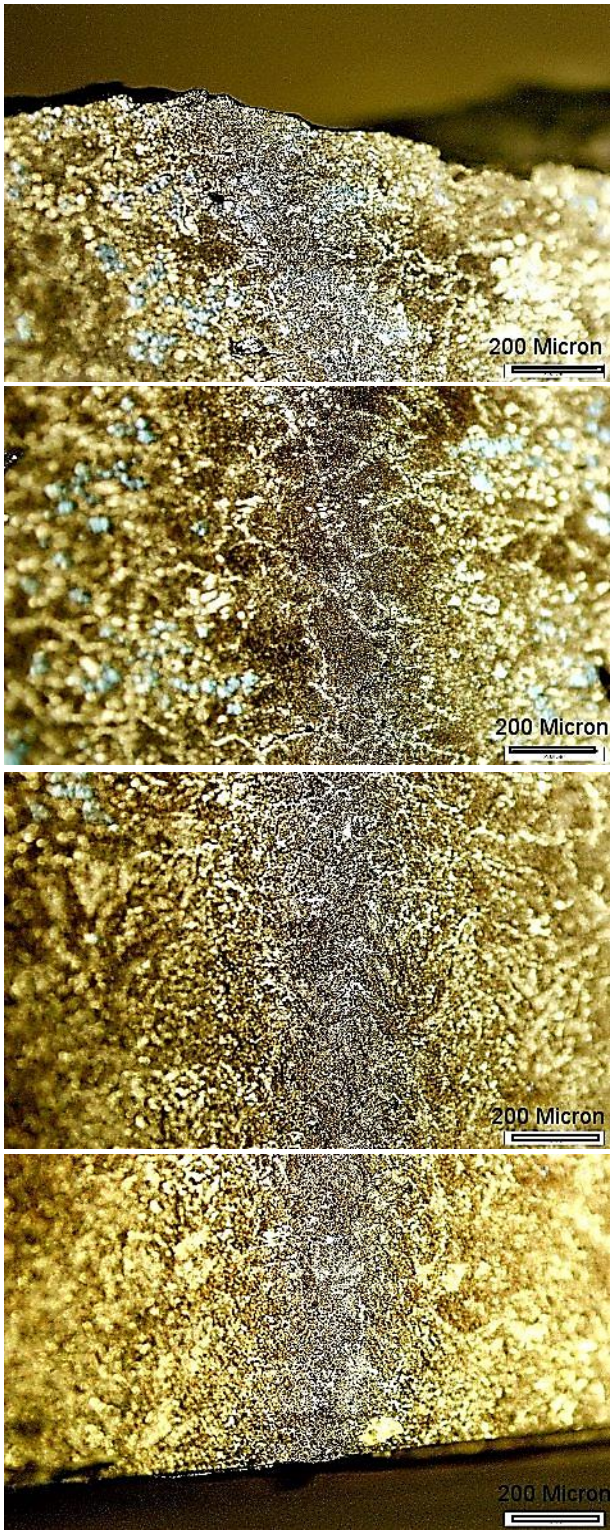

Figure 4. Distribution of reinforcing particles along the thickness from the outer wall to the inside (up to down) for the pouring temperature of 650 °C

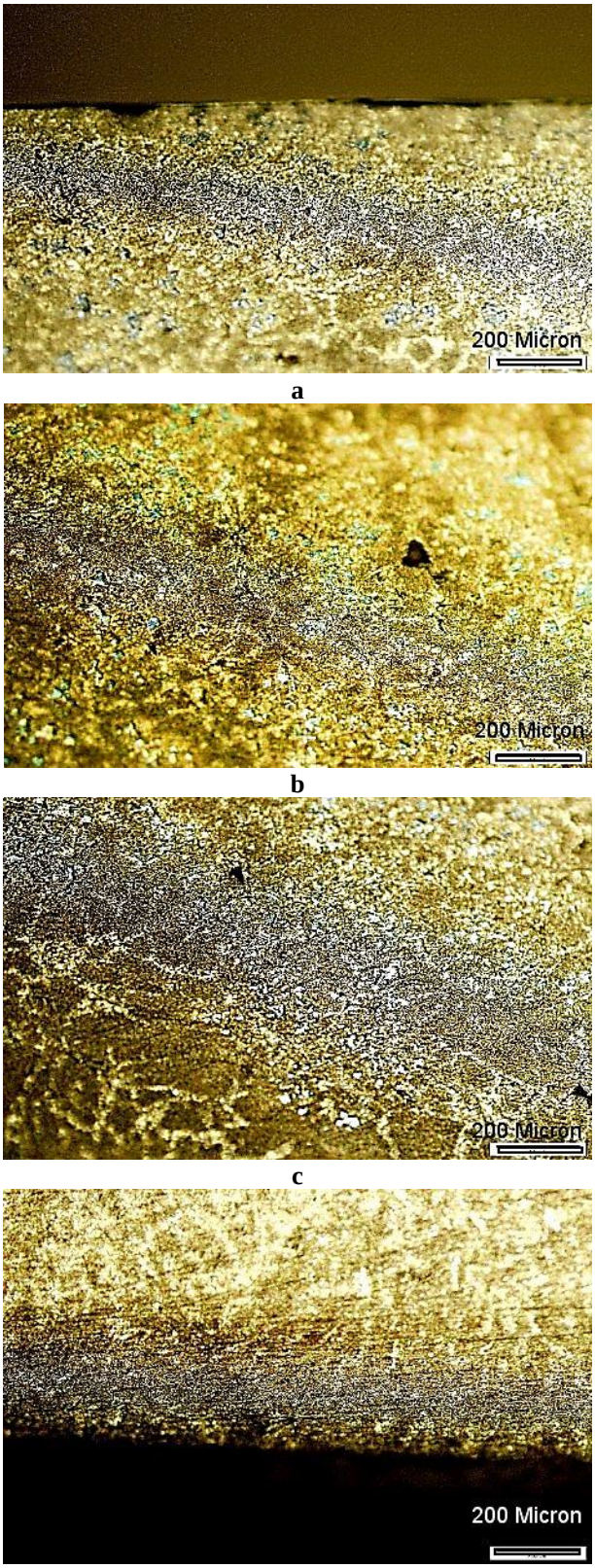

Figure 5. Distribution of reinforcing particles along the thickness from the outer wall to the inside (a to d) for the pouring temperature of 750 °C

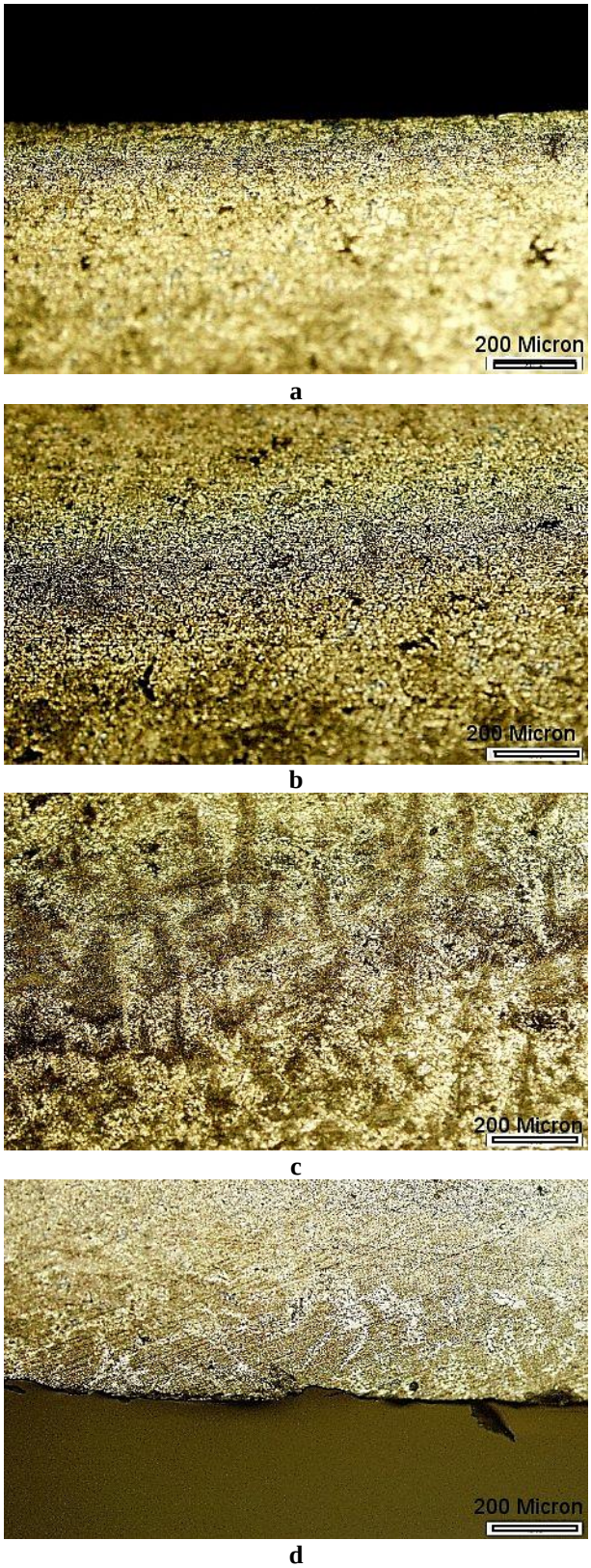

Figure 6. Distribution of reinforcing particles along the thickness from the outer wall to the inside (a to d) for the pouring temperature of 700 °C and preheat 300 °C

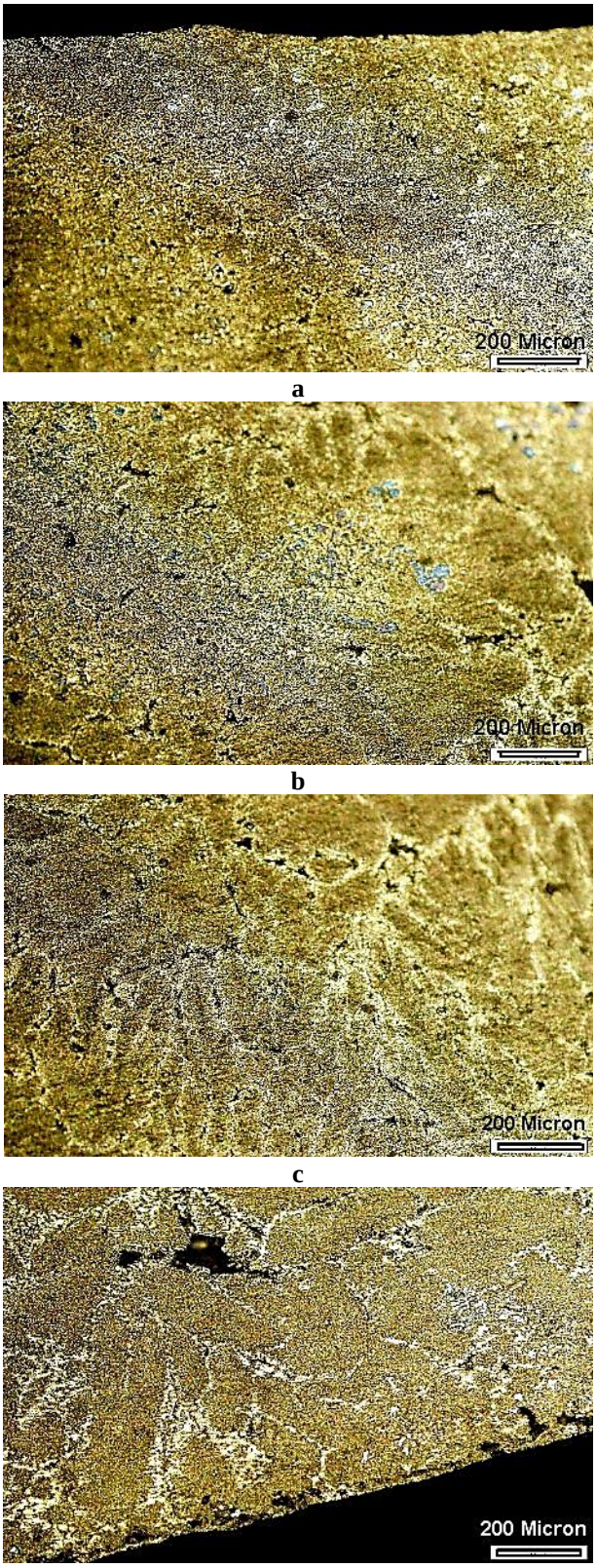

Figure 7. Distribution of reinforcing particles along the thickness from the outer wall to the inside (a to d) for the pouring temperature of 700 °C and preheat 150 °C

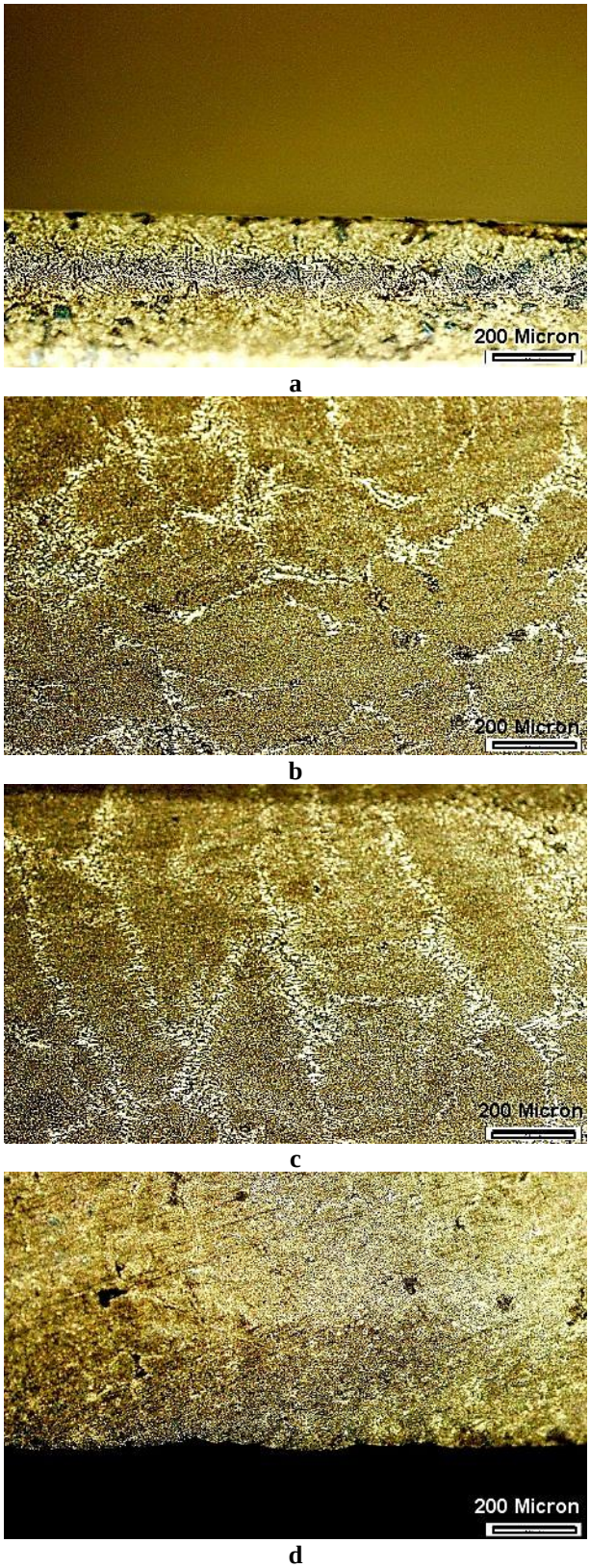

Figure 8. Distribution of reinforcing particles along the thickness from the outer wall to the inside (a to d) for the pouring temperature of 800 °C

Depending on the amount and shape of the reinforcement particles in the inner wall, the hardness values of the samples vary. For example, at the temperature of 650 °C, the non-uniform distribution of the reinforcement and its lower density in the inner wall can have the opposite effect on hardness.

The role of heat treatment in modifying the morphology and consequently optimizing the mechanical properties is undeniable. According to the conducted studies, the amount of wear resistance and in some cases, the amount of hardness increased by performing heat treatment. In Al-Mg_2Si composites, there are three types of reinforcing phases namely the primary and secondary Mg_2Si as well as the eutectic Mg_2Si where the primary Mg_2Si phase appears as polygonal or rough blocks, and the eutectic phase appears as feather or rods. The secondary Mg_2Si appears in the form of fine particles in the aluminum matrix, which is generally obtained after aging in hardenable alloys. Conducting dissolution heat treatment (properly) and rapid quenching led to the loss of rough reinforcing particles, and the rounding of the sharp corners of the primary Mg_2Si, as well as the polymorphic phase or eutectic rods with long rods, turned into a fine fibrous phase or particles, hence improvement in both toughness and wear properties. At higher pouring temperatures, the size of the primary Mg_2Si particles is larger than and the distance between the eutectic compounds is greater than the others. As the pouring temperature decreases, the size of the primary Mg_2Si particles and distance between eutectic arms decrease. This change in morphology will lead to an increase in both hardness and brittleness and a decrease in the ductility and toughness.

Figure 9 shows the light microscope images of the microstructure of the inner surface of the pipe made by the above composite with a pouring temperature of 650 °C, a dissolution temperature of 500 °C, and an aging temperature of 210 °C. Due to the low dissolution temperature and the lack of complete dissolution, it can be seen that the primary Mg_2Si phase retains its rough shape and sharp corners to a large extent, and the eutectic Mg_2Si is still present in the structure in the form of long rods. Also, due to the low pouring temperature, we see the porosity caused by premature freezing as well as the massive accumulation of reinforcing particles are seen, which could lead to the non-uniformity of the hardness distribution on the surface of the part and the high and low hardness with a large difference in different parts of the surface are seen. Similar results were reported by Rajaravi et al. [27].

Figure 10 shows the light microscope images of the microstructure of the inner surface of the above composite with a pouring temperature of 650 °C, a dissolution temperature of 570 °C, and an aging temperature of 210 °C. It can be seen that due to the high dissolution temperature and the proper dissolution of the reinforcing particles in the matrix, the sharp corners of the primary Mg_2Si particles are rounded and the eutectic phase has changed from the state of long rods to the form of microscopic fibers and particles.

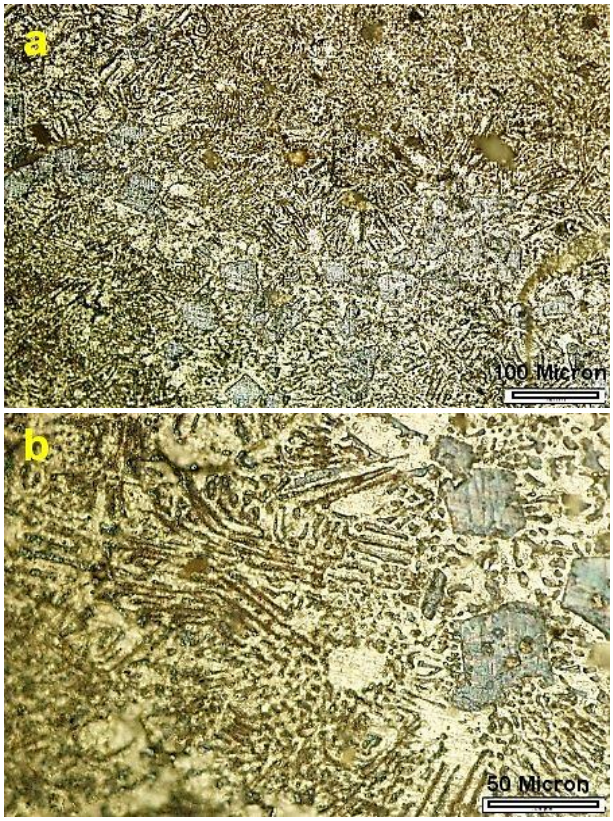

Figure 9. Light microscope image of the inner surface of the sample with a pouring temperature of 650 °C and a dissolution temperature of 500 °C and an aging temperature of 210 °C a) magnification 200x b) magnification 500x

Figure 11 shows the morphology of the reinforcement on the inner surfaces of two samples with a pouring temperature of 700 °C and dissolution and aging temperatures of 535 and 190 °C at two different preheat temperatures.

According to the lower preheat temperature of the mold in sample B (150 °C), it can be seen that the size of the primary Mg_2Si reinforcing particles is smaller compared to the second sample with a preheat temperature of 300 °C (A) which comes from the smaller freezing range and also the larger freezing rate. Also, in sample B, due to the limited range of freezing, more solidification porosity is observed.

Figure 12 shows the comparison of the microstructure of the internal surfaces of two samples at two pouring temperatures of 750 and 650 °C with the same heat treatment process (dissolution temperature of 570 and aging temperature of 210 °C) and the same mold preheating temperature.

It is evident from the images that the distribution of the primary Mg_2Si phase in the sample with a higher pouring

temperature is more uniform in comparison with the inner surface of the sample, and the average size of the primary Mg_2Si particles in the sample with a higher pouring temperature is smaller.

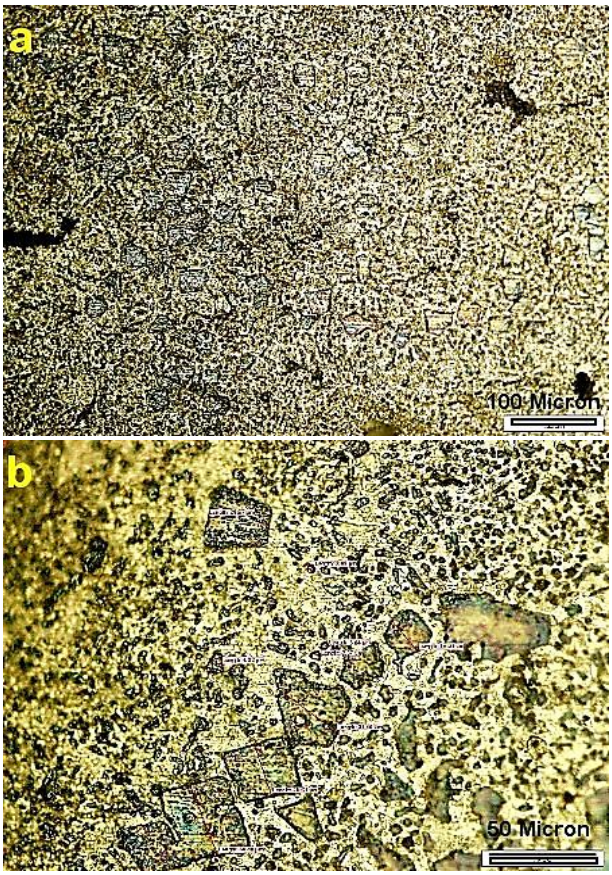

Figure 10. Light microscope image of the inner surface of the sample with a pouring temperature of 650 °C and a dissolution temperature of 570 °C and an aging temperature of 210 °C a) magnification 200x b) magnification 500x

Figure 13 shows the FESEM image of the sample poured at a temperature of 750 °C and a dissolution temperature of 570 °C.

As can be seen from this figure, the morphology of the reinforcing particles (primary Mg_2Si) has changed from rough to polygonal with rounded and spherical corners. The EDS analysis of the reinforcement is also shown in Figure 14.

According to the microstructure images and hardness tests, the highest hardness value is obtained in the sample with the heat treatment temperature of 535 °C and pouring temperature near 700 °C, which depends on the amount, shape, and size of the reinforcement in the inner wall.

Figure 15 shows the simultaneous effect of heat treatment temperature (dissolution) and pouring temperature on the hardness of the inner wall of different samples.

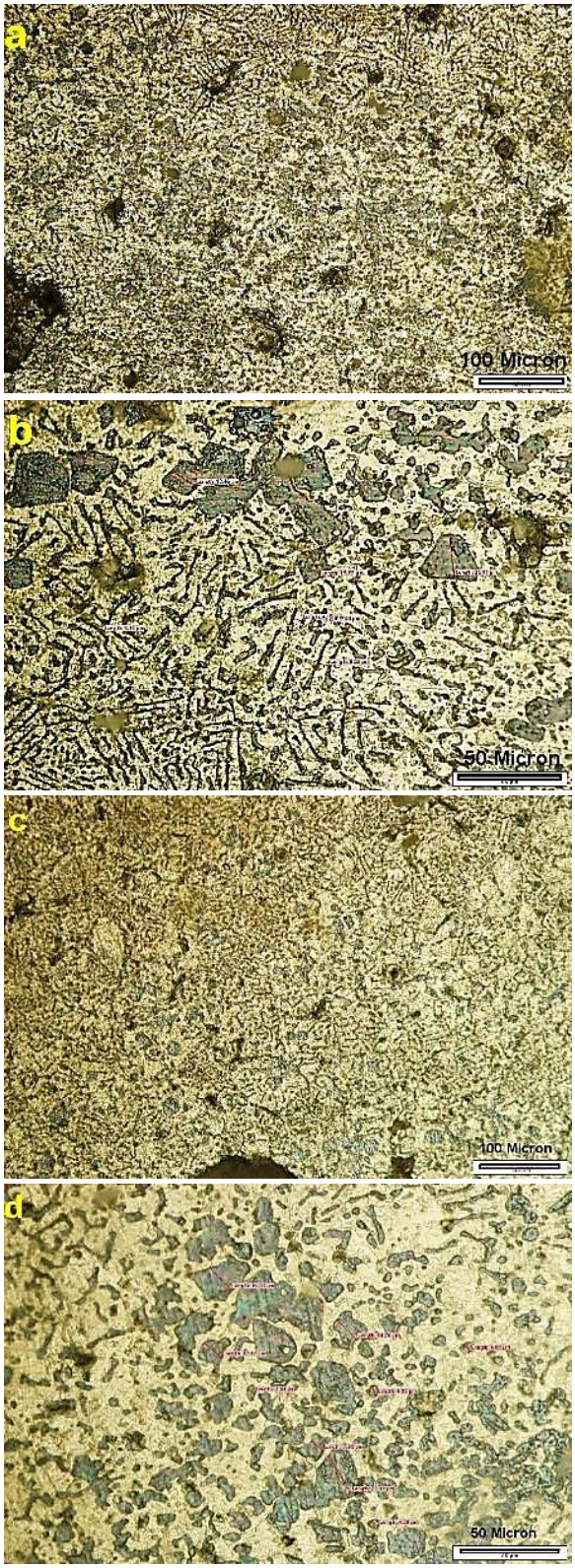

Figure 11. Light microscope image of the inner surface of the sample with a pouring temperature of 700 °C, a dissolution temperature of 535 °C, and an aging temperature of 190 °C a and b) mold temperature 300 °C c and d) mold temperature 150 °C

According to this shape, as the temperature of the heat treatment increases, the hardness of the samples improves significantly, which originates from the modification of the morphology, disappearance of thebrittle corners of the reinforcement, and improvement in the interface between the reinforcement and the ground.

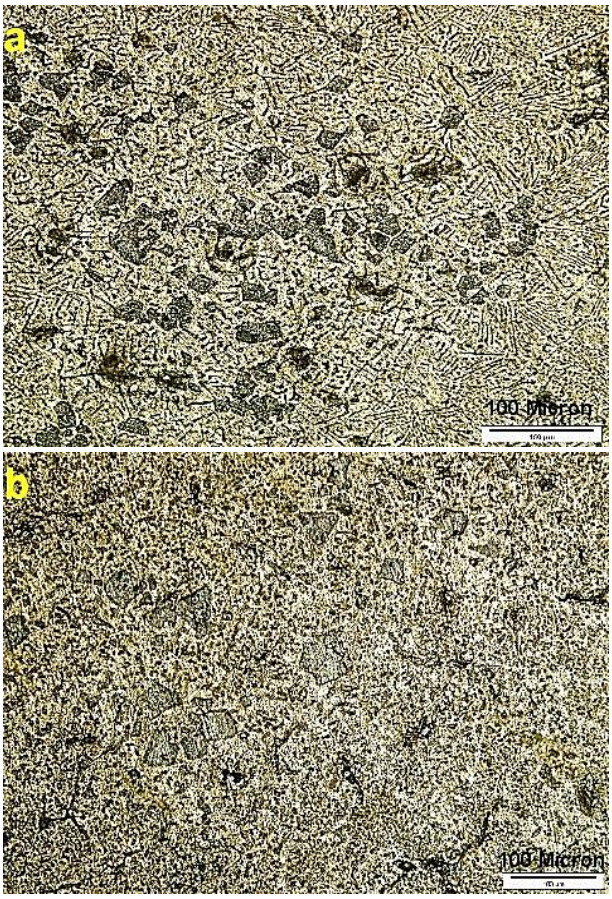

Figure 12. The microstructure of the internal surfaces of two samples at two pouring temperatures of 750 and 650 °C with the same heat treatment process (dissolution temperature of 570 and aging temperature of 210 °C) and the same mold preheat temperature a) 750 °C b) 650 °C

As the pouring temperature increases, the hardness first increases and then decreases. As the pouring temperature increases, on the one hand, the shape and size of the reinforcing particles become larger and rougher than usual, which leads to a decrease in hardness. On the other hand, at low pouring temperatures, due to the small freezing range and insufficient opportunity for the reinforcement to be placed in the inner wall, the reinforcements are not well distributed in this area. Internally, the hardness is low. It should be noted that at high temperatures, with the increase in the fluidity and decrease in melt viscosity, the friction between the mold and melt decreases, and the melt does not reach the speed of the mold in a short time, hence lack of effective placement of the reinforcement in the inner wall and a reduction in hardness.

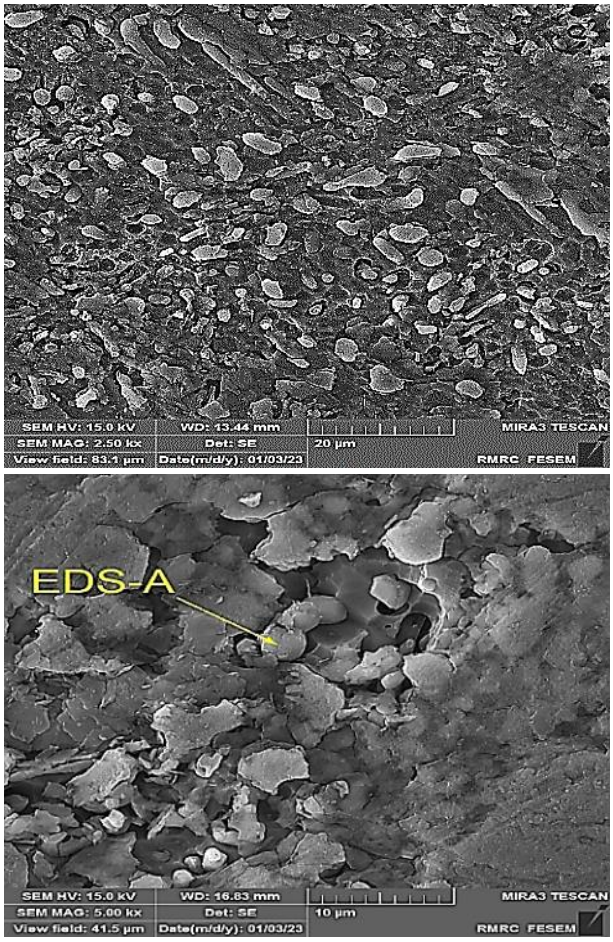

Figure 13. FESEM image of the reinforcement located on the inner surface of the sample poured at 750 °C and dissolution temperature of 570 °C

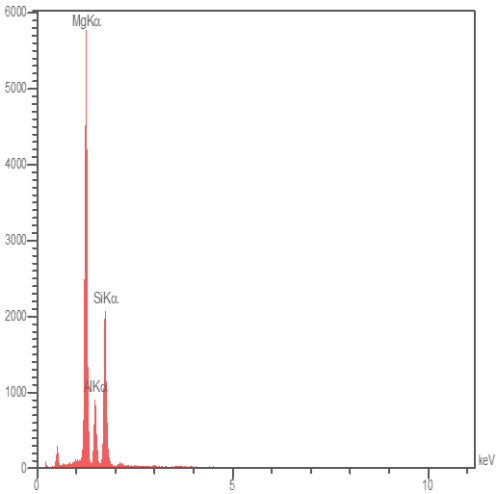

Figure 14. EDS analysis of the reinforcing particle shown in Figure 13

Figure 16 shows the simultaneous effect of aging temperature and pouring temperature on the hardness of the inner wall of different samples. As seen in the figures, hardness improves with the increase in the pouring temperature up to 700 °C and then it decreases [۲۸].

Of note, the change in the aging temperature does not have much effect on the hardness, which seems normal given the application of pure aluminum. According to Figures 15 and 16, the slope of the RSM diagram is higher for the heat treatment variable, which indicates the greater effect of this parameter on the response (hardness) than that of other variables.

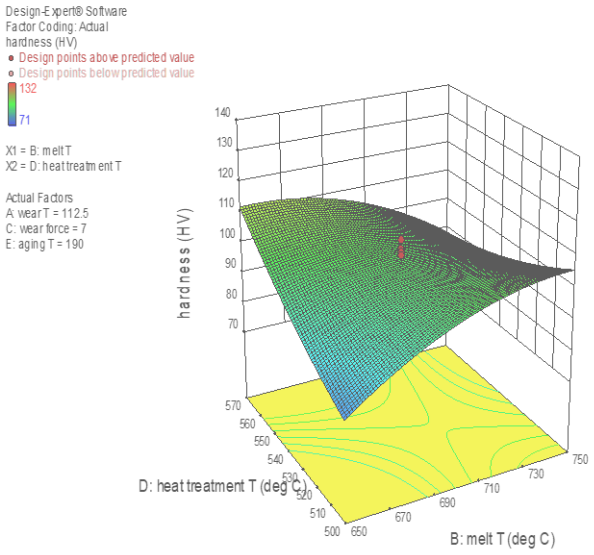

Figure 15. The simultaneous effect of pouring temperature and heat treatment (dissolution) temperature on the inner wall hardness of Al-15 wt. % Mg_2Si gradient composite tube

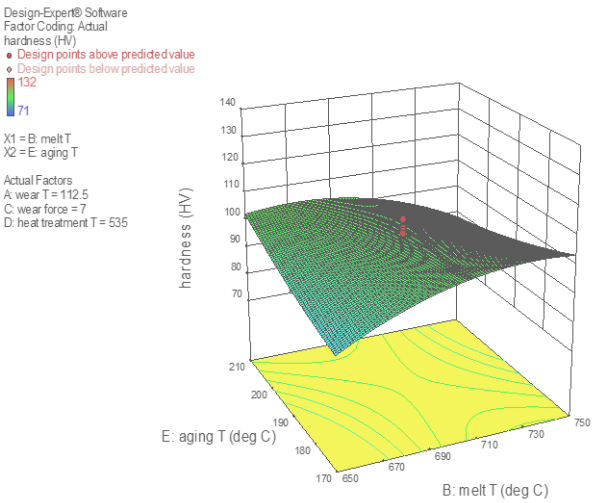

Figure 16. The simultaneous effect of aging temperature and pouring temperature on the hardness of the inner wall of Al-15 wt. % Mg_2Si gradient composite pip

According to Table 3 derived from Design Expert the values with the P-VALUE less than 0.05 have a significant effect while those greater than 0.1 do not have a significant effect on the desired response (hardness). In order to check the mutual effect of different variables, the P-VALUE of those two variables should be taken into consideration. According to the ANOVA table, the two variables of pouring and dissolution temperatures can be identified as the variable affecting the response (hardness). It should be mentioned that the effect of aging treatment is not much significant, as discussed earlier.

TABLE 3. ANOVA table

Source	Sum of Squares	DF	Mean Square	F Value	p-value Prob > F	
Block	804.82	1	804.82			
Model	5735.55	20	286.78	89.19	< 0.0001	Significant
A-melt T	15.89	1	15.89	4.94	0.0446	
B-heat treatment T	277.37	1	277.37	86.26	< 0.0001	
C-aging T	3.38	1	3.38	1.05	0.3243	
AB	2575.56	1	2575.56	801.00	< 0.0001	
AC	1008.06	1	1008.06	313.51	0.1543	
BC	5.06	1	5.06	1.57	0.2317	
A^2	1023.06	1	1023.06	318.17	< 0.0001	
B^2	112.26	1	112.26	34.91	< 0.0001	
C^2	72.87	1	72.87	22.66	0.0004	
Residual	41.80	13	3.22			
Lack of Fit	7.80	4	1.95	0.52	0.7263	Not Significant
Pure Error	34.00	9	3.78			
Corr. Total	6582.17	34				

Regarding the mutual effects of the variables, pouring and heat treatment temperatures were introduced as the variables that have significant mutual effects.

4. CONCLUSIONS

1. The experimental results of this study were in good agreement with those anticipated by ANOVA (above 89%).
2. Among the variables introduced in this study, the temperature of heat treatment (dissolution) had the greatest effect on the hardness of the Al-15Mg_2Si composite, and the best result was obtained at the temperature of about 535 °C.
3. The preheat temperature of the mold did not have much effect on the hardness of the final piece. The best distribution of reinforcing particles was obtained in the temperature range of 700 to 750 °C.

ACKNOWLEDGEMENTS

The authors would like to thank “Imam Khomeini International University” and, “Materials and Energy Research Center” for financial support of this work.

REFERENCES

1. K. K. Chawla, "***Composite Materials***", 2nd ed., (1998), New York, Springer.https://scholar.google.com/citations?view_op=view_citation&hl=en&user=ZvbtR0IAAAAJ&citation_for_view=ZvbtR0IAAAAJ:u5HHmVD_uO8C
2. A. Honarbakhsh, R. Khorshidi. M. Emamy. H. R. Jafari. (2011) ‘The Evolution of Heat Treatment on the Tensile Properties of Na-Modified Al-Mg_2Si In Situ Composite’. http://dx.doi.org/10.4028/www.scientific.net/AMR.311-313.283
3. Kaufman J. "***Aluminium Alloy Castings Properties, Processes, and Applications***", (2004). ASM International. Materials Park, USA. https://www.asminternational.org/aluminum-alloy-castings-properties-processes-and-applications/results/-/journal_content/56/05114G/PUBLICATION/
4. Shailesh Rao A, P G Mukunda, “Influence of teeming temperature of molten metal of Tin during centrifugal casting”, (2013), 51-54. https://doi.org/10.1179/174313309X436673
5. 5.Xiu, D., Yu, Q., Li, X., & An, G. "Mold filling behavior of melts with different viscosity under centrifugal force field", (2002), ***J. Mater. Sci. Technol***, 149. https://jmst.org/CN/Y2002/V18/I02/149
6. Zagórski, R., & Œleziona, J., "Pouring mold during the centrifugal casting process", (2007), ***Archives of Materials Science***, 442- 442. http://api.semanticsxholar.org/corpusid:136646360
7. Das, A., and Fan, Z. "Morphological development of solidification structures under forced fluid flow: experimental observation", (2003), ***Materials Science and Technology***, 573-580.https://cronfa.swan.ac.uk/Record/cronfa34623
8. Kumar, S., Sarma, V. S., & Murty, B. S. "Functionally Graded Al Alloy matrix in-situ composites", (2010), ***Metallurgical and Materials Transactions A***, 242-254. http://dx.doi.org/10.1007/s11661-009-0063-3
9. Yanbo, Zhai., and Ziuteng, Ma., and Zhen, Mei. “Centrifugal Forming Mechanism of Al Gradient Composites Reinforced with Complementary Primary Si and Mg_2Si Particles.”, (2014), ***Rare Metal Materials and Engineering*** 43(4): 0769-0774. https://doi.org/10.1016/S1875-5372(14)60081-3
10. Meiling Xin a ., Zhaodong Wang A., Bing Lu a ., Yong Li. “Effects of different process parameters on microstructure evolution and mechanical properties of 2060 AleLi alloy during vacuum centrifugal casting”. (2022), ***Journal of materials research and technology***. 54-68. https://doi.org/10.1016/j.jmrt.2022.08.147
11. Xue Sheng., Xiaoming Qian., Longzhou Meng., Zhaodong Wang. “Numerical Simulation of Density Segregation of Al Alloy During Centrifugal Casting”. ***2nd International Conference on Advanced Materials and Mechatronics (ICAMM 2022)***. https://doi.org/10.1088/1742-6596/2343/1/012012
12. M. Arefkhani, M. Razavi*, M.R. Rahimipour, A. Faeghinia. “The Effect of Rotation Speed on the Microstructure and Hardness of Synthesized Al-WC Nano-Composite by Centrifugal Casting”, (2016), ***Advanced Ceramics Progress***, Vol. 2, No. 4, 1-6. https://www.acerp.ir/article_70031_133f2af9dae6a8f98238833f8fc1842a.pdf
13. Mohamad Nirumand, Yaser Vahidshad, Massoud Emamy , Karen Abrinia. “Design and manufacturing of Al-Mg_2Si cylindrical functionally graded composites using in-situ centrifugal casting”, (2020), vol 8, No. 4, 1749-1757. https://doi.org/10.22068/jstc.2022.542863.1756
14. S Senthil Murugan ., S Balu Mahandiran ., M Vigneshkumar ., P Ashoka Varthanan ., S Sakthivel ., V Vicknesh. “Microstructural Analysis of Al-Sic Composites Fabricated Through Centrifugal Casting Process”.(2022), ***International Conference on Advancements in Materials and Manufacturing Engineering***. 291-296. https://doi.org/10.1063/5.0108070
15. Subhash Chandra Ram., Kausik Chattopadhyay.,and Awani Bhushan. “A literature review on Al-Si alloy matrix based in situ Al-Mg_2Si FG-composites: Synthesis, microstructure features, and mechanical characteristics”.(2022), Institution Of Mechanical Engineers. https://doi.org/10.1177/09544062221124064
16. Verma, R.K., Parganiha, D. & Chopkar, M. 2021. “A review on fabrication and characteristics of functionally graded aluminum matrix composites fabricated by centrifugal casting method”. ***SN Applied Sciences***. https://doi.org/10.1007/s42452-021-04200-8.
17. Yunus Emre ASAN., Murat ÇOLAK. 2022. “Modeling the Effect of Pour Height, Casting and Mold Heating Conditions for the Analysis of Fluidity of Different Section Thicknesses in Die Mold Casting of Al12Si Alloys. ***Journal of Science and Technology***. 14-27. http://doi.org/10.18185/erzifbed.1199648
18. Yi Si., Wanshan Di., Miao Liu., Yuexiang Zhao. “Effects of pouring temperature and electromagnetic stirring on the semi-solid microstructure of hypoeutectic Mg_2Si/Al composite”. (2020), ***IOP Conference Series: Earth and Environmental Science***. 692. http://doi.org/10.1088/1755-1315/692/3/032120
19. Shivkumar, S., Ricci, S., Keller, C. & Apelian, D. "Effect of solution treatment parameters on tensile properties of cast aluminum alloys". (1990), ***Journal of Heat Treating***, 63-70. https://doi.org/10.1007/BF02833067
20. Ogris, E., Wahlen, A., Lüchinger, H. & Uggowitzer, P. J. "On the silicon spheroidization in Al-Si alloys". , (2002), ***Journal of Light Metals***, 263-269. http://dx.doi.org/10.1016%2FS1471-5317(03)00010-5
21. Zhang, D. L., Zheng, L. H. & StJohn, D. H. "Effect of a short solution treatment time on microstructure and mechanical properties of modified Al–7wt.%Si–0.3wt.%Mg alloy". (2002), ***Journal of Light Metals***, 27-36. http://dx.doi.org/10.1016/S1471-5317(02)00010-X
22. Li, Zedi., and Li, Chong., and Liu, Yongchang., and Yu, Liming., and Gou, qianying., and Li, Huijun. “ Effect of heat treatment on microstructure and mechanical property of Al-10%Mg_2Si alloy.”, (2016), ***Journal of Alloys and Compounds*** 663: 16-19. https://doi.org/10.1016/j.jallcom.2015.12.128
23. A. Oyewole., A.M. Sunday. 2011. “Design and fabrication of a centrifugal casting machine”. ***International journal of engineering science and technology***. 8204-8210. https://journal.ump.edu.my/ijame/article/download/5019/1374/23363

24. M. Tebib., F. Ajersch., A.M. Samuel., and X.-G. Chen. “Solidification and Microstructural Evolution of Hypereutectic Al-15Si-4Cu-Mg Alloys with High Magnesium Contents”, (2013), ***The Minerals, Metals & Materials Society and ASM Internationa***l. 4282-4295. https://doi.org/10.1007/s11661-013-1769-9
25. M. R. Akbarpour , F. S. Torknik. “Modelling and Optimization of Densification and Hardness of Cu/SiC Nanocomposites based on Response Surface Methodology (RSM)”, (2021), ***Advanced Ceramics Progress***, vol 7, No.4, 28-35. https://doi.org/10.30501/acp.2022.325167.1080
26. Prasad, K. K., Murali, M. S., & Mukunda, P. G. (2010). Analysis of fluid flow in centrifugal casting. ***Frontiers of Materials Science in China***, 103-110. https://doi.org/10.1007/s11706-010-0005-4
27. C. Rajaravi., B. Gobalakrishnan., and P. R. Lakshminarayanan. “Effect of pouring temperature on cast Al/SiCp and Al/TiB2 metal matrix composites”, (2019), ***Journal of the Mechanical Behavior of Materials***. 162-168. https://doi.org/10.1515/jmbm-2019-0018
28. D.M. Wankhede., B.E. Narkhede., S.K. Mahajan., C.M. Choudhari. 2018. “Influence of pouring temperature and external chills on mechanical properties of aluminum silicon alloy castings”. ***Materials Today: Proceedings***. 17627- 17635. https://doi.org/10.1016/j.matpr.2018.06.081

Advanced Ceramics Progress: Vol. 9, No. 3, (Summer 2023) 16-30

Materials and Energy Research Center
MERC

Contents lists available at ACERP

Advanced Ceramics Progress

Journal Homepage: www.acerp.ir

Original Research Article

Influence of B_4C Nanoparticles on Corrosion Characteristics of Ni Matrix Nanocomposite Coatings Fabricated via Pulse Electroplating Technique

Mohammad Kaveh [a], Mohammad Sajjadnejad [b*], Abbas Mohassel [b], Nader Setoudeh [c]

[a] *MSc, Department of Materials Engineering, School of Engineering, Yasouj University, Yasouj, Iran.*
[b] *Assistant Professor, Department of Materials Engineering, School of Engineering, Yasouj University, Yasouj, Iran.*
[c] *Associate Professor, Department of Materials Engineering, School of Engineering, Yasouj University, Yasouj, Iran.*

* Corresponding Author: m.sajjadnejad@yahoo.com; m.sajjadnejad@yu.ac.ir (Dr. Mohammad Sajjadnejad) URL: https://www.acerp.ir/article_206098.html

ARTICLE INFO

Article History:

Received: 06 December 2023
Revised: 09 April 2024
Accepted: 01 September 2024

Keywords:

Ni-B_4C Nanocomposite,
Pulse Electrodeposition,
Microstructure,
Corrosion,
Potentiodynamic Polarization

ABSTRACT

The Ni-B_4C nanocomposite coatings were fabricated via pulse electrodeposition on a copper substrate, and the effects of pulse current density, duty cycle, and pulse frequency on the microstructure, morphology, and corrosion characteristics were assessed. Field emission scanning electron microscopy (FESEM), energy-dispersive X-ray spectroscopy (EDS), X-ray diffraction (XRD), potentiodynamic polarization, and electrochemical impedance spectroscopy (EIS) tests were employed. The baseline electrodeposition conditions were set at i = 1 A/dm², γ = 50%, and f = 10 Hz. Embedding B_4C nanoparticles (NPs) into the nickel matrix significantly reduced the nickel crystallite size for the primary (111) and (200) crystal planes. Increasing the pulse current density from 1 to 4 A/dm² caused a substantial decrease in the incorporation rate of B_4C NPs, from 5.5 to 2.9 vol.%. However, an increase in the duty cycle from 25 to 50% and the pulse frequency from 1 to 10 Hz raised the incorporation rate to 5.5 vol.% and 4.6 to 3.9 vol.%, respectively. Surprisingly, the incorporation of B_4C led to an increase in the corrosion current density from 2.301 to 4.541 µA/cm². Increasing the pulse current density from 1 to 4 A/dm² and the duty cycle from 25 to 50% notably decreased the corrosion current density from 4.541 to 1.375 µA/cm² and from 7.243 to 4.541 µA/cm², respectively. Conversely, the minimum corrosion current density of 0.599 µA/cm², deposited at 1 Hz, increased significantly to 4.541 µA/cm² at 10 Hz, while the B_4C NPs content increased from 3.9 to 5.5 vol.%, possibly due to a more uniform distribution of B_4C NPs at 1 Hz. The Ni-B_4C specimen deposited at 1 Hz exhibited a higher Rct compared to the pure nickel sample under baseline conditions, indicating strong consistency between the EIS and potentiodynamic results.

https://doi.org/10.30501/acp.2024.429141.1141

1- INTRODUCTION

In recent years, coatings have been extensively applied to various substrates to significantly enhance surface characteristics such as mechanical properties, wettability, adhesion, lubrication, as well as scratch, wear, and corrosion resistance [1-4]. Several coating fabrication techniques have been utilized, including plasma spray [5], sol-gel [6-8], high-velocity oxygen fuel (HVOF) [9], chemical vapor deposition (CVD) [10], physical vapor deposition (PVD) [11], electrophoretic deposition [12] and electrodeposition [12-17], to improve surface and tribology as well as corrosion properties.

Electrodeposition is well known as a fundamental technique for fabricating metal matrix composite (MMC)

Please cite this article as: Kaveh, M., Sajjadnejad, M., Mohassel, A., Setoudeh, N. "Influence of B_4C nanoparticles on Corrosion Characteristics of Ni Matrix Nanocomposite Coatings Fabricated via Pulse Electroplating Technique", ***Advanced Ceramics Progress***, Vol. 9, No. 3, (2023), 16-30. https://doi.org/10.30501/acp.2024.429141.1141

coatings [18]. It is also regarded as one of the most efficient approaches, offering advantages such as easy preparation, versatility, and low cost for producing composite coatings based on both metallic and non-metallic components [19, 20]. These coatings are reinforced with second-phase particles, including ceramic carbides, oxides, nitrides, silicates, and diamond particles. Examples of these reinforcements include SiC [21, 22], B_4C [23-25], WC [26], TiO_2 [27, 28], Al_2O_3 [19, 29], ZnO [30, 31], Y_2O_3 [32], Ni_3S_4 [33], TiN [34, 35], graphene [36], CNT [32], and diamond [33], which help produce micro- and nanocomposite coatings with enhanced microhardness, texture, self-lubrication, wear resistance, tribological characteristics, and corrosion and oxidation resistance [1, 15, 16, 37].

Metal matrix composites (MMCs) are widely employed in material manufacturing. The metallic element forms the basis of the composite, while ceramic compounds act as second-phase reinforcing particles, defining the mechanical and structural properties. As one of the leading types of composite coatings, MMCs have widespread applications in various industries [12]. They are particularly well-known for their excellent wear, abrasion, corrosion, and high-temperature resistance, as well as their remarkable hardness, rigidity, stiffness, and modulus of elasticity [18].

Nickel and its alloys offer a wide range of applications in electrodeposited coatings due to their high strength-to-weight ratio, toughness, electrical and thermal conductivity, strong optical reflectivity, and, most notably, exceptional chemical stability and corrosion resistance. Nickel's tendency to form a protective passive layer contributes to the outstanding corrosion resistance of nickel matrix coatings in aqueous, saline, mineral acids, alkaline, and organic environments [15, 16, 38-41]. As a result, nickel matrix coatings are among the most extensively researched categories of MMC coatings, thanks to their protective nickel layer, excellent corrosion resistance, reproducibility, low cost, easy maintenance, and reduced energy requirements [42, 43]. Nickel matrix coatings reinforced with ceramic micro- and nanoparticles are widely used in various industries, including gears, bearings, blades, and the coal, petroleum, chemical, petrochemical (oil and natural gas), marine, automotive, medical, and aviation sectors (e.g., aircraft parts), offering superior microhardness, modulus of elasticity, wear, and corrosion resistance [12, 34, 44].

In recent years, nanoparticles have increasingly proven to be effective reinforcing agents in composite coatings, enhancing the mechanical, tribological, corrosion, and oxidation resistance properties compared to pure metal and micro-sized composite coatings [45]. The nanocomposite electrodeposition process occurs in at least three consecutive steps: i) transport of nanoparticles in the electrolyte toward the electrode, ii) absorption onto the surface of the electrode (cathode), and iii) embedment via the metallic particles of the electrodeposits [46].

Pulse electrodeposition (PE) is the preferred method for creating nickel-based coatings on blades, cylinders, bearings, and valves. PE offers several advantages, including ease of operation, high efficiency, safety, reliability, and lower cost compared to direct current (DC) electrodeposition, reverse PE, and brushing electrodeposition [47, 48]. For example, the use of PE in fabricating Ni–W/SiC nanocoatings via a modified Watt's nickel solution demonstrates excellent anti-corrosion performance in a 3.5 wt% NaCl corrosive environment [49]. PE provides precise control over the microstructure, mechanical properties, and corrosion resistance of electrodeposited coatings. Additionally, PE allows for a higher average current density (ia) compared to the DC method, preventing the formation of dendrites in the coating morphology. The participation of reinforcing particles is also significantly higher in the pulse current (PC) method than in the DC approach [17, 50]. The pulse electrodeposition parameters include current density (i), duty cycle (%), and pulse frequency ("γ"). These factors have a significant impact on the characteristics of PC electrodeposited coatings. The PC approach represents the duty cycle as the proportion of total on-time inside a pulse cycle, expressed as a percentage [51, 52]:

$$\text{Duty cycle } (\gamma) = \frac{T_{on}}{T_{on}+T_{off}} = T_{on}.f \quad (1)$$

where *f* is pulse frequency and is indicated as the cycle time (*T*) reciprocal [51, 52]:

$$\text{Frequency (f)} = \frac{1}{T_{on}+T_{off}} = \frac{1}{T} \quad (2)$$

The mean current density (I_A) formulated in the PC technique is also described as [51]:

$$I_A = \text{peak current } (I_p) \times \text{duty cycle } (\gamma) \quad (3)$$

The electrolyte conditions in the PC approach include factors such as bath chemical composition, temperature, pH, plating time, and stirring rate. Additionally, the characteristics of the incorporated particles—such as particle size, shape, concentration, dispersion type, and other surface properties—play an important role in determining the microstructure and morphology of the coatings [15, 16]. These factors, in turn, significantly influence the enhancement or reduction of the corrosion and wear resistance of the coatings [17, 23, 44].

A review of the literature reveals that B_4C in MMCs is regarded as an ideal reinforcing agent due to its outstanding mechanical properties and high chemical stability [53]. With a melting point of 2350°C and a Mohs hardness of 9.5, B_4C is one of the most stable materials, resistant to corrosion by hot hydrogen fluoride (HF) and nitric acid (HNO3), and insoluble in both acids and water [54]. In a very recent study conducted by Ramadoss et al. [55], an aluminum hybrid metal matrix composite (AHMMC) reinforced with B_4C and BN particles significantly improved corrosion resistance due to the formation of a protective layer. The incorporation of B_4C nanoparticles into Ni-B matrix composite coatings, fabricated via the electroless method, led to a remarkable increase in the microhardness and wear resistance of the Ni-B-B_4C composite coatings [56]. Pushpanathan et al. [57] studied the effect of varying pulse current density (up to 2 A/dm²) and duty cycle (up to 30%) for pulse-electrodeposited Ni-B_4C-TiC nanocomposite coatings under a fixed pulse frequency and nanoparticle concentrations of 0.5 g/L B_4C and 1 g/L TiC. The results showed improved hardness and wear resistance compared to the pure Ni-B coating. Similarly, the findings of [24] on Ni-B-based pulse electrodeposited composite coatings reinforced with B_4C sub-micron particles on N80 steel indicated an average microhardness of 1030.61 Hv and enhanced wear resistance with a coefficient of friction (COF) of 0.22. Additionally, the coatings exhibited good corrosion resistance, with a corrosion voltage of -0.3 V and a corrosion current of -1.15 μA for Ni-B/ B_4C coatings deposited at 2 g/L

in a 3.5 wt% NaCl solution. In another study, Dong et al. [58] fabricated superhydrophobic composite coatings on Q235 steel and found that the incorporation of B_4C particles created a unique micro-nano structure, inducing rough morphology, improving corrosion resistance, and promoting coating growth, resulting in a strong barrier effect and enhanced stability. Increasing the pulse frequency from 1 to 10, 100, and 1000 Hz in Ni-W-based coatings reinforced with B_4C nanoparticles revealed a significant reduction in grain size and roughness, a decrease in Ni content, and an increase in the participation of W and B_4C in the coating. The composite coating deposited at 100 Hz demonstrated the best corrosion resistance [59]. Optimizing electroplating parameters such as electrolyte bath temperature, deposition current intensity, and plating time, with the aid of Response Surface Methodology (RSM), can greatly enhance the hardness and corrosion resistance of electroplated Ni-B_4C coatings on AZ31 Mg alloy, demonstrating the effectiveness of Ni-B_4C composite coatings [60].

To the best of our knowledge, although other researchers have explored the effects of incorporating B_4C micro- and nanoparticles into metal matrix composites—particularly nickel-based coatings produced using various methods and deposition conditions—there have been few comprehensive studies on how the operating parameters of pulse electrodeposition (PE) influence the microstructure, texture, morphology, particle incorporation rate, and corrosion properties of these composite coatings. This study aims to develop nickel-based composite coatings strengthened with B_4C nanoparticles using the PE technique. The microstructure, morphology, and corrosion characteristics of the resulting Ni-B_4C coatings are evaluated through potentiodynamic polarization tests and electrochemical impedance spectroscopy. These coatings are deposited under varying pulse parameters, including pulse current density, duty cycle, and pulse frequency. The findings of this investigation are thoroughly analyzed and discussed.

2- MATERIALS AND METHODS

The nanocomposite coatings were electrodeposited onto a copper substrate in Watt's bath electrolyte. This section outlines the essential equipment and conditions required for the electrodeposition process, examines the influencing parameters, details the surface preparation, and describes the various tests used to assess the microstructural, morphological, and corrosion characteristics. These assessments were conducted using FESEM, EDS, XRD, potentiodynamic polarization, and EIS techniques.

2-1– THE PROCURATION OF ELECTRODEPOSITION BATH

In this research, the conventional electrolyte solution for fabricating nickel-based coatings, known as Watt's bath, was used. The main component of Watt's bath is nickel sulfate ($NiSO_4 \cdot 6H_2O$), which is employed to fabricate pure nickel and nickel nanocomposite coatings reinforced with B_4C nanoparticles. Nickel chloride ($NiCl_2 \cdot 6H_2O$) is then added to enhance the ionic conductivity of the solution. During electrodeposition (also known as electroplating), an external current is applied to the solution, promoting ion movement, improving electroplating efficiency, and reducing energy consumption.

An anionic surfactant, sodium dodecyl sulfate (SDS) with the chemical formula $CH_3(CH_2)_{11}SO_4Na$, is used as a surface activation agent to prevent particle agglomeration by increasing electrostatic repulsion. SDS also alters wettability, facilitates the uniform distribution of nanoparticles in the bath, and minimizes the porosity of the coating. The surface activation mechanism charges neutral particles and, with the help of the applied current, creates optimal conditions for particle incorporation into the matrix [61]. Finally, the boric acid (H_3BO_3) is added to the solution to control the pH of the bath. All chemical compounds were utilized as-received and were procured from Merck company. The electrodeposition bath composition, production company, and coordinated concentration are characterized in Table 1.

Table 1. The electrodeposition bath's chemical composition and concentration

Chemical composition	Concentration (g/L)
$NiSO_4.6H_2O$	300
$Na_3C_6H_5O_7$	40
B_4C	5
$CH_3(CH_2)_{11}SO_4Na$ (SDS)	40
NH_3	0.3

The TEM image and the corresponding specification of B_4C nano-powders utilized in this research are illustrated in Figure 1 and tabulated in Table 2, respectively.

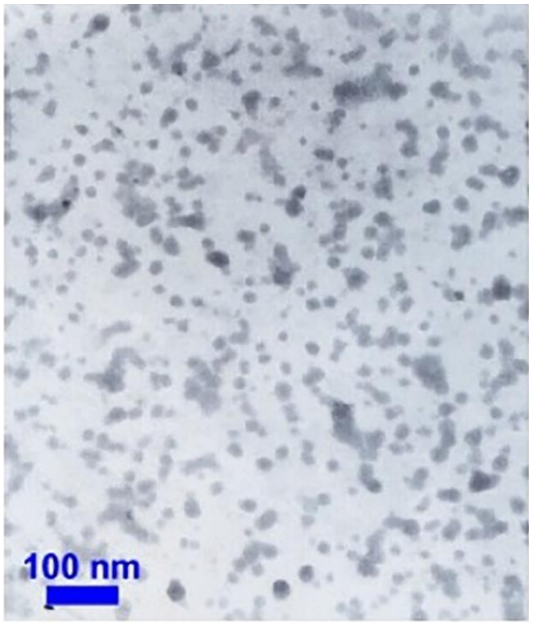

Figure 1. TEM image of B_4C nano-powders.

Table 2. The specification of B_4C nano-powders

Product Name	Boron Carbide Nanopowder (g/L)
Purity	99.0 %+
Dissociate Oxygen Content	0.8
Crystaline Phase	Monocrystalline
Particle Size	<50nm
Specific Surface Area	75 m^2/g
Loose Loading Density	0.01 g/cm^3
Color	Grey Black

2-2 – PREPARATION OF THE SUBSTRATE

To prepare the coating specimens, copper was selected as the substrate, and several samples were cut to achieve a uniform surface area. The copper substrates were ground using SiC abrasive paper from 150 to 2000 grit, then polished with alumina slurry solution (mean particle size of 1 μm) to achieve a mirror-like finish. The samples were cleaned with acetone under ultrasonication, immersed in a 15% HCl dilute solution for surface activation, and slightly corroded at the grain boundaries to enhance coating adhesion. Finally, the samples were rinsed in distilled water and absolute alcohol, dried with hot air, and made ready for use in the three-electrode electrodeposition cell.

2-3 – THE PROCESS OF ELECTRODEPOSITION

The electrodeposition bath was prepared according to the instructions detailed in Section 2-1 and poured into a 50 mL beaker. The solution was then stirred using a magnetic heater and preheated to ensure even distribution. Prior to preheating, the required amount of B_4C nanoparticles was added to the Ni-B_4C electrodeposition bath. To prevent nanoparticle agglomeration and ensure their suspension in the electrolyte, SDS was also added to the bath. The solution was stirred for 24 hours to hydrate the nanoparticles and improve their wettability. A temperature controller was used to maintain the bath temperature. The electrodeposition parameters are summarized in Table 3.

Table 3. The electrodeposition bath parameters

Electrodeposition bath parameter	Value /Degree
pH	4
Temperature (°C)	50
Stirring rate (rpm)	250

In this study, five separate specimens were prepared based ib variant electrodeposition parameters, as provided in Table 4.

Table 4. Pulse electrodeposition parameters of pure nickel and nickel-B_4C nanocomposite coating samples under variant electrodeposition conditions

Sample	B_4C nanoparticle concentration (g/l)	Maximum Current density (i_p) (A/dm^2)	Duty cycle (%)	Pulse frequency (Hz)
*Ni- B_4C (Baseline Ni -B_4C)	5	1	50	1
Ni- B_4C	5	4	50	1
Ni- B_4C	5	1	25	1
Ni- B_4C	5	1	50	10
Pure nickel (Baseline Ni)	-	1	50	1

* Baseline sample

The substrate surface area must be precisely defined for electrodeposition. To achieve this, the area not intended for coating must be insulated from contact with the electrolyte using electrical (friction) tape or nail lacquer. Just before starting the electrodeposition process, the electrolyte bath (solution) was subjected to ultrasonication to disperse all particles evenly. The electrodeposition cell was then partially immersed in the electrolyte solution, and the sample was placed into the cavity of the cell. The electrolyte was stirred at a maximum velocity of 250 rpm.

For electrodeposition, nickel served as the anode and copper as the cathode. The anode-to-cathode surface area ratio was maintained between 3 to 5 to prevent anodic polarization, and the distance between them was set to 2 to 3 cm. Pulse frequency, duty cycle, total time (T_{ON} + T_{OFF}), and On and Off times of the electrodeposition process were calculated separately to determine the required current based on the desired current density. Unlike direct current (DC) electrodeposition, pulse current (PC) electrodeposition used a conventional power supply with a current converter to produce a pulse current. The negative (-) and positive (+) poles of the power supply were connected to the cathode and anode, respectively, via electric wires to the pulse generator of the power supply.

After electrodeposition, the specimens were carefully removed from the electrolyte solution without direct hand contact and immediately immersed in distilled water, followed by ultrasonication for a brief period. This process helps to detach particles with weak bonds from the surface, improving the accuracy of subsequent analyses. After drying, the characteristics of the coated nanocomposite samples were examined using FESEM, XRD, and corrosion tests.

2-4 – ELECTROCHEMICAL CORROSION TESTS

The pure nickel and nickel-B_4C nanocomposite coating specimens were prepared for electrochemical corrosion tests. First, each coating sample was pierced with a tiny drill, connected to an electric wire, and the surrounding excess surfaces were insulated with lacquer. Following sample preparation, potentiodynamic polarization tests were conducted. The experiments were performed in a Pyrex glass three-electrode cell, with a 3.5 wt.% NaCl solution as the corrosive electrolyte. All tests were carried out at room temperature. Prior to testing, each specimen was immersed in the corrosive solution for 45 minutes to allow the surface to reach equilibrium with the corrosive components in the electrolyte. The corrosion measurements were conducted using an AUTOLAB PGSTAT-302N instrument equipped with NOVA 2.1.4 software for potentiodynamic polarization tests. The various components of the AUTOLAB PGSTAT-302N instrument, the corrosion test cell setup, and the pure nickel and Ni-B_4C coating specimens are clearly illustrated in Figures 2 and 3.

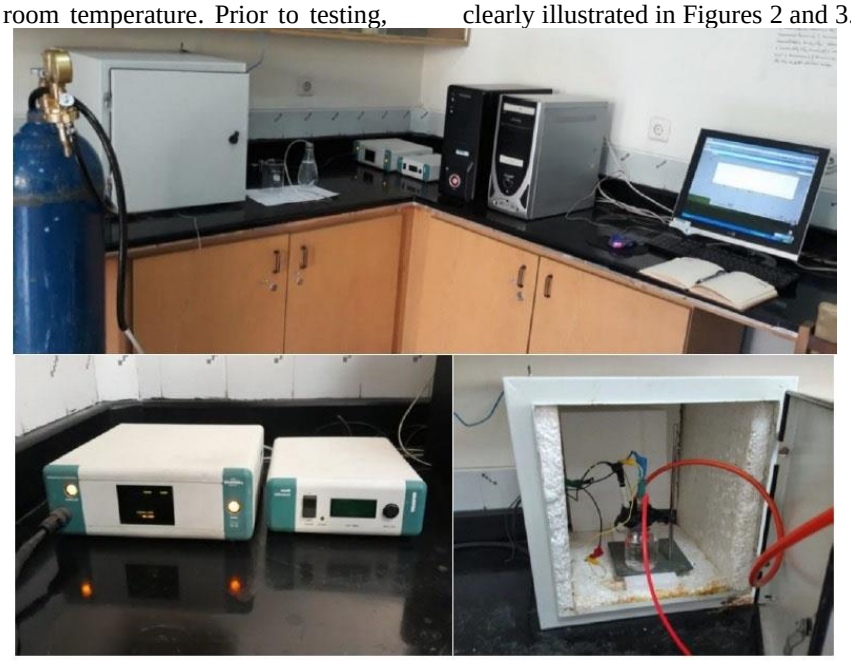

Figure 2. The AUTOLAB PGSTAT-302N instrument and corrosion cell setup.

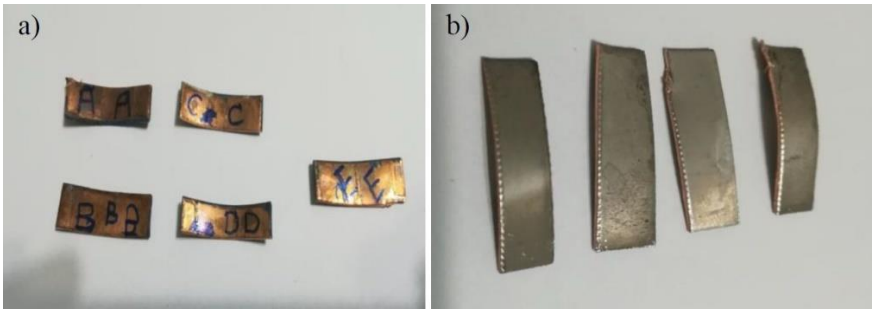

Figure 3. The coating specimens. a) The copper substrate and b) The coated surface.

In the electrochemical corrosion test, specifically the potentiodynamic polarization test, the specimen is polarized relative to its equilibrium condition. In other words, the sample potential is varied positively or negatively from the equilibrium potential or Open Circuit Potential (OCP). The OCP is the potential difference between the working electrode and the reference electrode when the sample is exposed to the electrolyte in an equilibrium state, with no measurable corrosion current. The OCP should stabilize at a constant potential with minimal fluctuations. The surface area of the sample must be accurately determined for current density calculations.

Each corrosion test involves three electrodes: a working electrode, a counter electrode, and a reference electrode, chosen according to the coating type and corrosion environment. In this research, a saturated Calomel reference electrode was used. To obtain the cathodic and anodic branch slopes, two appropriate points were selected on each branch, and the intersection of these slopes was calculated to determine the corrosion current density. The Tafel and potentiodynamic test parameters were extracted using Nova 2.1.4 software. The corrosion current density is calculated using the

following equation:

$$i_{corr} = \frac{\beta_a \beta_c}{2.303(\beta_a+\beta_c)R_p} \quad (4)$$

where β_a describes the anodic branch slope, β_c represents the cathodic branch slope, and R_p points out the polarization resistance, which is defined as the potential difference variations versus the current alterations [3]. Through the determination of corrosion current density, the corrosion rate can be obtained via the below relation:

$$CR^1\left(\frac{mm}{y}\right) = 3.27 \times i_{corr}\left(\frac{mA}{cm^2}\right) \times \frac{Ew}{D} \quad (5)$$

where EW stands for equivalent weight and D indicates density, both of which are equal to 63.5 g/mol and 8.96 g/cm^3 for nickel, respectively.

Electrochemical impedance spectroscopy (EIS) was performed after the electrodeposition process using a three-electrode cell containing a 3.5 wt.% NaCl solution. A calomel electrode was used as the reference electrode, and a counter electrode was also included. Prior to each experiment, the specimens were immersed in the corrosion cell and exposed to the electrolyte to monitor the Open Circuit Potential (OCP) for a specific period (e.g., 15 minutes) until the potential stabilized. The EIS analysis was then conducted over a frequency range from 100,000 Hz to 0.01 Hz, with a sinusoidal AC potential applied at an amplitude of ±10 mV versus OCP for all pure nickel and Ni-B_4C nanocomposite coating samples. The extracted EIS parameters were subsequently fitted using ZViewTM software (Version 3.4, Scribner Associates Inc.).

2-5 – MORPHOLOGICAL STUDIES VIA FESEM

To identify the morphology of the pure nickel and nickel-B_4C nanocomposite coating samples, FESEM analysis was performed using a MIRA3 TESCAN model instrument. Prior to the microstructural assessment and evaluation of electrical conductivity, the specimen surfaces were coated with a very thin layer of gold.

2-6 – CHEMICAL CHARACTERIZATION VIA EDS

EDS (or EDX) and MAP analysis were performed on the coating samples for chemical characterization. EDX analysis was used to determine the incorporation rate of B_4C nanoparticles in the nanocomposite coating. The weight percentages (wt.%) of Ni, B, and C in the coating matrix were calculated using EDX analysis and subsequently converted to volume percentages (vol.%). The volume percentages (vol.%) were derived using the following equations:

$$\text{The wt.\% of } B_4C = \frac{\text{Boron (B) \% obtained from EDAX} \times B_4C \text{ molar mass}}{\text{Boron molar mass}} \quad (6)$$

$$\text{The wt.\% of Ni} = 100 - \text{The wt.\% of } B_4C \quad (7)$$

where B_4C molar mass is 55.255 g/mol, B molar mass is 10.811 g/mol, and C molar mass is 12.011 g/mol. The B_4C incorporation rate (vol. %) is then calculated via Equation 8:

$$B_4C \text{ vol.\%} = \frac{100 \times \frac{\text{The wt.\% of } B_4C}{B_4C \text{ density}}}{\frac{\text{The wt.\% of Ni}}{\text{Nickel density}} + \frac{\text{The wt.\% of } B_4C}{B_4C \text{ density}}} \quad (8)$$

where B_4C density is 2.52 g/cm^3, Nickel density is 8.9 g/cm^3, and Carbon density is 2.2 g/cm^3.

2-7 – MICROSTRUCTURAL ASSESSMENT BY XRD STUDIES

To investigate the crystalline microstructure of the pure Ni and Ni-B_4C coatings, X-ray diffraction (XRD) analysis was conducted using a Philips Bruker D8 diffractometer with a copper Kα source. The reported findings were analyzed using Xpert High Score Plus software.

3- RESULTS AND DISCUSSION

3-1 – CHEMICAL COMPOSITION AND MORPHOLOGY OF Ni-B4C

The microstructure and morphology of pure nickel and nickel nanocomposite coatings reinforced with B_4C nanoparticles were evaluated using FESEM, EDS, and MAP analysis. These analyses investigated the incorporation of B_4C nanoparticles and the effects of pulse electrodeposition (PE) parameters on the microstructure of the coatings. Table 5 categorizes the specimens based on their PE parameters. The baseline sample, E, represents pure nickel, while samples A to D denote Ni-B_4C pulse electrodeposited nanocomposite coatings.

Table 5. Vol. % of B_4C nanoparticles regarding the pulse electrodeposition parameters

Sample	i (A/dm^2)	f (Hz)	γ (%)	Vol. % B_4C
A (Baseline Ni-B_4C)	1	10	50	5.5
B (Ni-B_4C)	4	10	50	2.9
C (Ni-B_4C)	1	10	25	4.6
D (Ni-B_4C)	1	1	50	3.9
E (Baseline Ni)	1	10	50	0

Figure 4a and 4b show the BSE and EDS analyses of the baseline Ni-B_4C nanocomposite coating deposited under conditions of i_{corr} = 1 A/dm^2, γ = 50 %, f = 10 Hz. The map analysis of Boron and Carbon distribution confirms the incorporation of these elements into the nickel coating matrix.

[1] Corrosion Rate (CR)

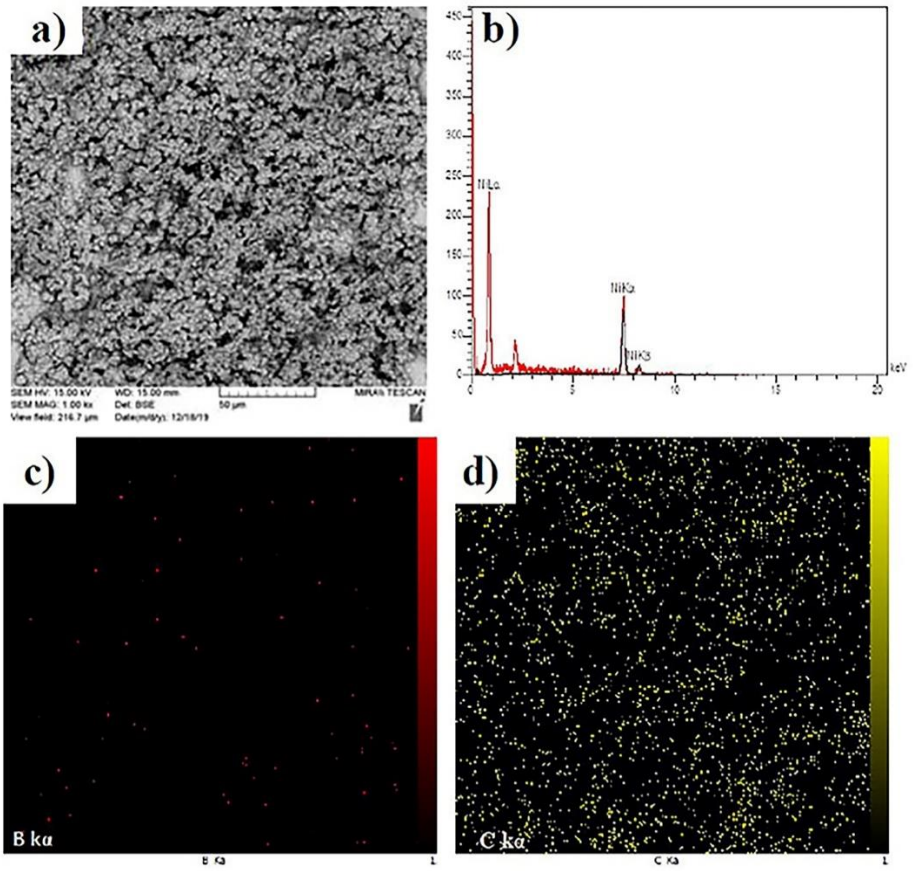

Figure 4. BSE and EDS analysis of the Ni-B_4C baseline nanocomposite coating deposited under i_{corr} = 1 A/dm^2, f = 10 Hz, γ = 50 %. a) BSE micrograph at 50µm, b) EDS spectrum, c) Boron distribution map, and d) Carbon distribution map.

The FESEM micrographs of pure nickel and Ni-B_4C nanocomposite coatings fabricated under the baseline electrodeposition conditions are shown in Figure 5a and 5b. Figure 5a demonstrates the morphology of pure Ni, which consists of fine nickel pyramids. In contrast, the incorporation of 5.5 vol.% B_4C nanoparticles into the nickel matrix transformed the coating morphology from nickel pyramids (see Figure 5a) to a spherical (nodular) microstructure (see Figure 5b). Similar microstructures have also been observed in other studies on composite coatings, such as Ni-Mo [62], Ni-Cr [63], Ni-WC [64], Ni-ZnO [31], and Ni- Si_3N_4 [33].

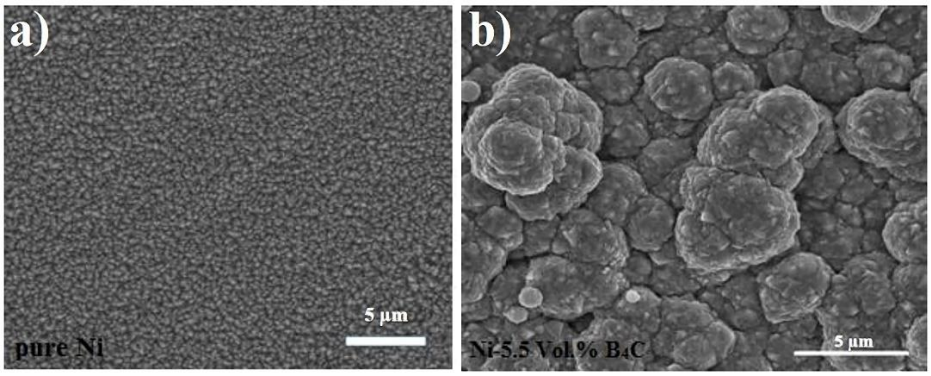

Figure 5. The FESEM micrographs of baseline pure nickel and Ni-B_4C nanocomposite coatings

The FESEM micrographs of Ni-B_4C nanocomposite coatings produced at 1 and 4 A/dm^2, under baseline conditions (f = 10 Hz, γ = 50 %.) are demonstrated in Figure 6. a and b.

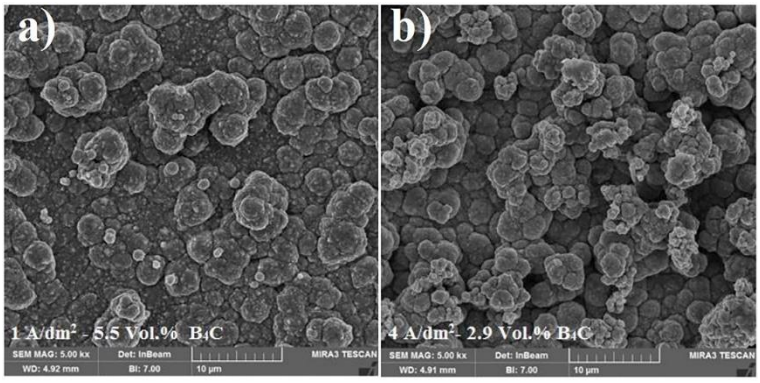

Figure 6. The FESEM micrographs of Ni-B_4C nanocomposite coatings deposited under f = 10 Hz, γ = 50 %. at: a) 1 A/dm^2 and b) 4 A/dm^2

As depicted in Figure 6, increasing the current density from 1 to 4 A/dm² resulted in changes in the microstructure and a decrease in the incorporation rate of B_4C nanoparticles, from 5.5 to 2.9 vol.%. This indicates that, despite the higher driving force, the reduction rate of deposited nanoparticles was diminished. The reduction rate of Ni^{2+} ions exceeded the adsorption rate of nanoparticles on the surface, leading to a decrease in B_4C nanoparticle incorporation [65]. In other words, while increasing the pulse current density initially leads to more deposition of B_4C nanoparticles in the coating, at higher current densities, the diffusion of Ni atoms into the matrix surpasses that of the B_4C nanoparticles, resulting in a significant reduction in B_4C incorporation. Dini et al. [66] noted that increasing the pulse current density to a certain limit raises the overpotential and increases the nucleation rate, ultimately resulting in a microstructure with finer grains. by Ebrahimi et al. [67] explained that the enhancement of electroplating current density leads to a reduction in nickel ion reduction in the microstructure and co-deposition of hydrogen at the cathode-electrolyte interface. Rashidi and Amadeh [68] also found that increasing the electroplating current density from 1 to 5 A/dm² reduced the grain size, although further increases in current density led to a nearly constant grain size.

As observed in Figure 7, increasing the duty cycle from 25% to 50% led to a higher incorporation rate of B_4C nanoparticles, from 4.6 to 5.5 vol.%. This increase can be attributed to the relationship $i_m = i_p \times \gamma$ (refer to relation 3 in the Introduction), where the average current density rises with the duty cycle, resulting in a greater amount of nanoparticles incorporated into the coating [16]. Specifically, at lower duty cycles (short TON or long TOFF), the coating tends to have high impact but may exhibit negligible porosity. In such cases, the nanoparticles embedded in the coating may have weak connections, making the coating prone to separation or peeling. Increasing the duty cycle enhances the incorporation rate of nanoparticles into the coating. However, when the duty cycle is further increased to 75%, the nanoparticle incorporation rate decreases. This is associated with a rise in current density and a significant increase in grain size [16, 50].

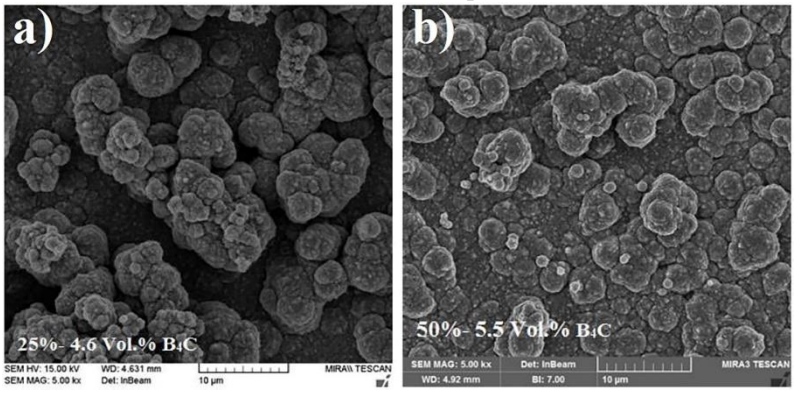

Figure 7. The FESEM micrographs of Ni-B_4C nanocomposite coatings deposited under i_{corr} = 1 A/dm^2, f = 10 Hz, at duty cycle of a) γ = 25 % and b) γ = 50 %

Figure 8 illustrates the changes in morphology as the pulse frequency increased from 1 to 10 Hz. Raising the pulse frequency from 1 to 10 Hz for the Ni-B_4C samples resulted in an increase in B_4C nanoparticle incorporation from 3.9 to 5.5 vol.%. This improvement is due to the reduction in total electrodeposition time (T_{ON}+ T_{OFF}) and the increased number of electrodeposition cycles, which leads to a higher percentage of nanoparticles being incorporated into the coating [14]. Chen et al. [69] demonstrated that increasing the pulse frequency, which results in a higher number of deposition cycles and shorter T_{ON} and T_{OFF} periods, enhances the incorporation of the secondary reinforcing phase into the matrix.

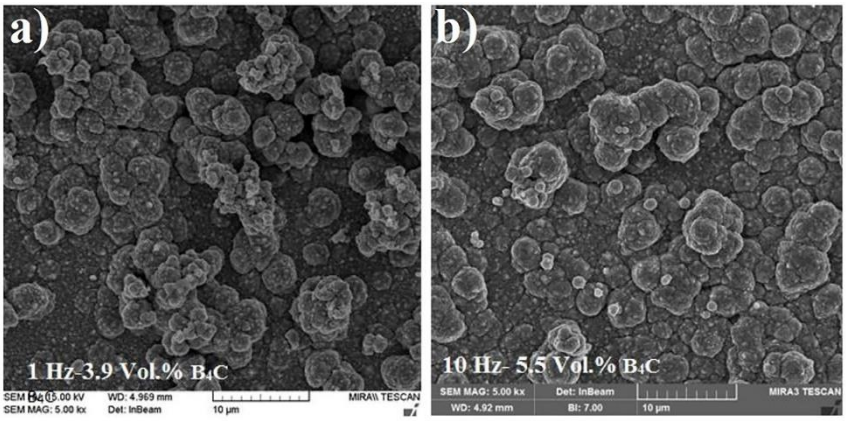

Figure 8. The FESEM micrographs of Ni-B_4C nanocomposite coatings deposited under i_{corr} = 1 A/dm^2, γ = 50 % at pulse frequencies of a) f = 1 Hz and b) f = 10 Hz

Sajjadnejad et al. [3] found that increasing the pulse current density led to a significant increase in the number of nanoparticles deposited in Ni-nanodiamond composite coatings. Similar results were reported by Lajevardi and Sharabi [70] for Ni-TiO_2 composite coatings. Additionally, our recent study on the wear and tribological properties of Ni-B_4C nanocomposite coatings showed a substantial improvement in microhardness across all Ni-B_4C specimens deposited under different electrodeposition parameters, compared to pure nickel coatings [71].

3-2- MICROSTRUCTURAL STUDIES VIA XRD ANALYSIS FINDINGS

In this section, the XRD results of pure nickel and nickel-B_4C nanocomposite coatings were determined and the effect of B_4C incorporation on the microstructure and the crystallite size of the coatings is thoroughly investigated.

The embedment of B_4C nanoparticles in the nickel matrix led to an increase in the peak broadening in XRD spectrum peaks so that the crystallite size experienced a huge reduction in the Ni- B_4C coating compared to pure Ni coating. The crystallite size of the main peaks was obtained via Scherrer's equation and the obtained results are given in Table 6. To assess the influence of B_4C nanoparticles on the coating characteristics, the size of crystallites was determined by Xpert software using Scherrer's equation as follows:

$$d = \frac{K\lambda}{\beta Cos\theta} \quad (9)$$

where D indicates the size of crystallites, k denotes the shape factor constant approximately taken as 1 for particles or crystallites and 0.94 precisely for spherical crystallites, λ describes the X-ray wavelength in nm, β represents the peak width at the half intensity or FWHM (Full Width Half Maximum) shown in radians, and θ is the diffraction angle in radians [72]. The peak broadening is initiated by crystal defects, twin boundaries, strain, and crystallite size.

Table 6- The XRD analysis results for pure Ni and Ni-B_4C nanocomposite baseline samples obtained via the Scherrer technique.

Sample	2θ (°)	(hkl)	FWHM	d (nm)
Pure Ni	44.239	(111)	0.12	73.2
	50.431	(200)	0.192	44.7
Ni-B_4C	44.898	(111)	-	32
	52.148	(200)	-	23

Figure 9 and Table 6 show the XRD spectrum for both pure Ni and Ni-B_4C coatings. The data reveal that incorporating B_4C nanoparticles into the matrix significantly reduced the relative intensity of the (111) and (200) crystal planes. Additionally, the crystallite size of nickel decreased notably for these planes, from 73.2 nm to 32 nm for (111) and from 44.7 nm to 23 nm for (200). The presence of B_4C nanoparticles increases the number of nucleation sites, which contributes to the reduction in crystallite size [3].

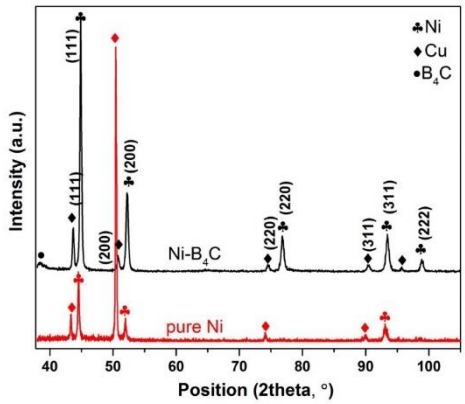

Figure 9. The XRD spectrum for pure nickel and Ni-B_4C nanocomposite coatings

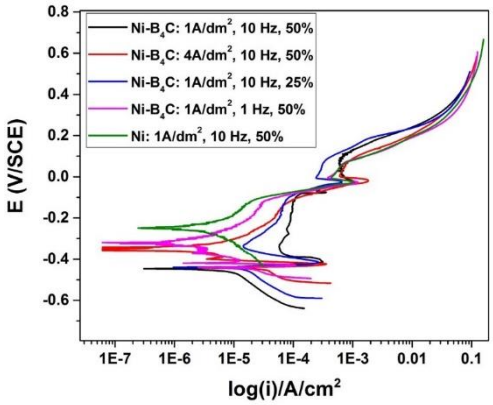

Figure 10. The potentiodynamic polarization curves for pure Ni and Ni-B_4C coatings under variant electrodeposition parameters

Li et al. [73] observed that the primary structure of nickel-diamond coatings at $2\theta = 43.2°$ is FCC, which aligns with our findings. As shown in Table 6, the inclusion of B_4C nanoparticles in the nickel coating contributes to a significant reduction in the crystallite size of the main peaks. This effect is primarily due to the B_4C nanoparticles acting as a reinforcing phase and creating additional nucleation sites within the nickel grain boundaries, resulting in a finer microstructure. Moreover, Tao et al. [74] proved nanoparticle incorporation as the main reason for peak broadening and decrease in the crystallite size of the Ni-B-Sc composite coating.

3-3 – THE CORROSION CHARACTERISTICS

The corrosion characteristics of pure nickel and nickel-B_4C nanocomposite coatings were evaluated using potentiodynamic polarization and electrochemical impedance spectroscopy (EIS).

Figure 10 shows the potentiodynamic polarization curves for both pure Ni and Ni-B_4C nanocomposite coatings. The curves reveal two distinct anodic and cathodic branches in the active region, as well as the passive and trans-passive regions beyond them.

Figure 10 illustrates the potentiodynamic polarization curve demonstrating the active-passive behavior typical of pure nickel coatings. This curve is divided into three critical regions: i. Active, ii. Passive, and iii. Transpassive. The pitting potential (E_{pit}) is the boundary between the passive region and the beginning of the transpassive region.

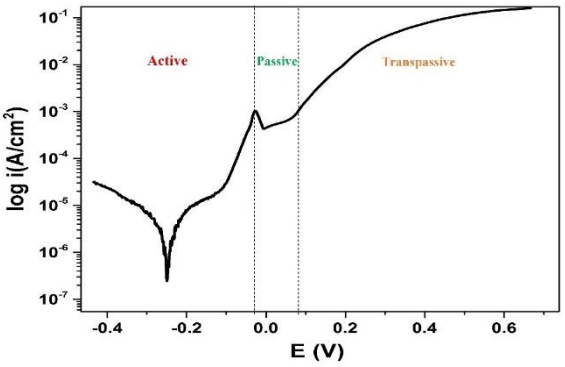

Figure 11. The typical potentiodynamic polarization curve for pure Ni coating with an active-passive corrosion behavior exhibiting active, passive, and trans-passive regions.

The extracted data from potentiodynamic polarization tests such as corrosion current density (i_{corr}), corrosion potential (E_{corr}), and pitting potential (E_{pit}) for all pure Ni and Ni-B_4C coatings under various pulse electrodeposition parameters are shown in Table 7.

Table 7- The extracted data from the potentiodynamic polarization test for all pure Ni and Ni-B_4C coatings under variant pulse electrodeposition parameters

Sample	Chemical composition of coating	B_4C concentration (g/L)	Current density (A/dm^2)	Duty cycle (%)	Pulse frequency (Hz)	B_4C Incorporation rate (vol. %)	Corrosion potential)V vs. SCE(	Corrosion current density ($\mu A/cm^2$)	Corrosion rate (mm/year)	Pitting potential (E_{pit}) – (V vs. SCE)
A	Ni-B_4C	5	1	50	10	5.5	-0.446	4.541	0.048	0.105
B	Ni-B_4C	5	4	50	10	2.9	-0.353	1.375	0.011	0.081
C	Ni-B_4C	5	1	25	10	4.6	-0.439	7.243	0.077	0.086
D	Ni-B_4C	5	1	50	1	3.9	-0.32	0.599	0.006	0.073
E	Ni	0	1	50	10	0	-0.249	2.301	0.024	0.055

Figure 10 and Table 7 show that the best corrosion resistance was observed in the D sample, a Ni-B_4C coating deposited under i = 1 A/dm², γ = 50 %, and f = 1 Hz, which had the lowest corrosion current density of 0.559 µA/cm². Interestingly, despite an incorporation rate of 5.5%, B_4C nanoparticles led to an increase in corrosion current density from 2.301 to 4.541 µA/cm² in the baseline condition (i = 1 A/dm², γ = 50 %, and f = 10 Hz). This increase is likely due to uneven distribution and participation of B_4C nanoparticles in the nickel matrix. Nonetheless, the Ni-B_4C nanocomposite coatings, specifically samples B (deposited under i = 4 A/dm², γ = 50 %, and f = 10 Hz) and D (deposited under i = 1 A/dm², γ = 50 %, and f = 1 Hz), demonstrated lower corrosion current densities and thus better corrosion resistance compared to pure nickel coatings.

Increasing the pulse current density from 1 to 4 A/dm² led to a significant reduction in corrosion current density from 4.541 to 1.375 µA/cm², while the B_4C incorporation rate decreased from 5.5 to 2.9 vol.%. This improvement is likely due to a more uniform distribution and greater compaction of the nanocomposite coating achieved at 4 A/dm². Amadeh et al. [75] observed similar trends in their study on Ni-SiC coatings, where raising the pulse current density from 2 to 8 A/dm² reduced corrosion current density significantly, although the corrosion potential shifted to a more negative value and no major changes were noted in the passive region. Sajjadnejad et al. [16] found that for Ni-diamond coatings, increasing the pulse current density from 1 to 4 A/dm² resulted in a more positive corrosion potential and lower corrosion current density. However, further increasing the current density to 10 A/dm² reduced corrosion resistance, attributed to higher participation at 4 A/dm² and reduced B_4C incorporation at higher current densities.

Increasing the duty cycle from 25% to 50% in Ni-B_4C coatings resulted in a reduction in corrosion current density from 7.243 to 4.541 µA/cm², which was associated with an increase in B_4C nanoparticle incorporation from 4.6% to 5.5% vol.%. Sajjadnejad et al. [16] observed a similar trend, noting that while increasing the duty cycle improved B_4C incorporation up to a certain point, further increases in the duty cycle led to a reduction in nanoparticle incorporation.

On the other hand, increasing the pulse frequency from 1 to 10 Hz caused a notable rise in corrosion current density from 0.599 to 4.541 µA/cm². This decline in corrosion resistance was linked to a higher B_4C incorporation rate, from 3.9% to 5.5% vol.%, which suggests that the more uniform distribution of B_4C nanoparticles at lower frequencies contributed to this effect. Shahrabi et al. [70] found similar results with Ni-TiO_2 coatings, where increasing pulse frequency improved corrosion resistance. In contrast, Sajjednejad et al. [3] observed that higher pulse frequencies led to increased overpotential and altered surface topography, which enhanced B_4C nanoparticle incorporation and improved corrosion resistance. Amadeh et al. [75] reported that raising the pulse frequency from 10 to 1000 Hz decreased corrosion current density due to increased B_4C nanoparticle incorporation in Ni-SiC coatings. Medelien et al. [76] noted that B_4C incorporation shifted the corrosion potential to more negative values and increased the electrochemical activity of the nickel coating, attributing reduced corrosion resistance to the semi-conductive behavior of B_4C. Jiang et al. found that increasing B_4C concentration from 2 to 8 g/L shifted the Tafel curves to positive potentials and enhanced corrosion resistance, which was ascribed to the uniform and compact structure of the Ni-B_4C nanocomposite coatings [77].

As seen in Table 7 and Figure 10, the incorporation of B_4C nanoparticles into the nickel matrix caused a significant positive shift in the pitting potential E_{pit} for all Ni-B_4C coatings compared to the pure nickel coating. This shift can be attributed to the inhibitory effect of B_4C particles, which help to fill surface defects and porosities, thereby preventing the diffusion of highly corrosive ions, particularly chloride ions (Cl^-), present in the NaCl corrosive environment studied in this research. Furthermore, the B_4C incorporation extended the passive region for all Ni-B_4C coatings relative to the pure nickel coating, indicating enhanced corrosion resistance.

The EIS curves including the Nyquist, Bode-magnitude, and Bode-phase plots for pure Ni and Ni-B_4C nanocomposite coating deposited under i = 1 A/dm², γ = 50 %, f = 10 Hz and i = 1 A/dm², γ = 50 %, and f = 1 Hz, respectively, are presented in Figure 12.

To achieve optimal EIS curve fitting for the pure Ni and Ni-B_4C coatings, the recommended equivalent circuit is displayed in Figure 13. The fitting was performed using ZView™ software based on the data extracted from EIS analysis. In this circuit, **Rs** represents the solution resistance, **Rct** denotes the charge transfer resistance, and **CPE_{dl}** refers to the constant phase element of the double-layer. The presence of a single capacitance loop or semicircular arc in the Nyquist plot indicates a charge transfer corrosion mechanism, while the Bode plots for both pure Ni and Ni-B_4C coatings show only one time constant. This equivalent circuit and its fitting curve were thus used for data analysis and discussion. Similar equivalent circuits were applied by Li et al. [59] and Omidvar et al. [78] for assessing the corrosion characteristics of the Ni-W-B_4C coatings and NiBP-graphite coatings, respectively.

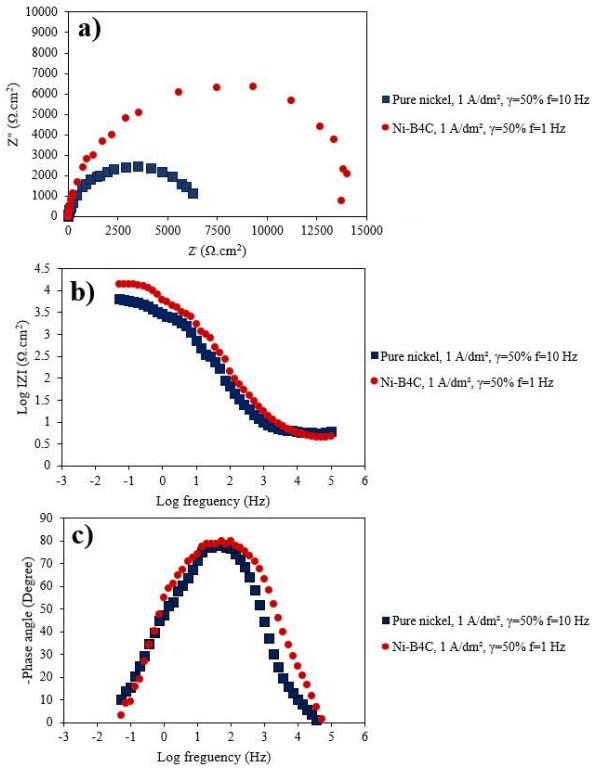

Figure 12. The Nyquist, Bode magnitude, and Bode phase plots extracted from the EIS obtained results for pure nickel deposited under i = 1 A/dm^2, γ = 50 %, f = 10 Hz and nickel-B_4C nanocomposite coating fabricated at i = 1 A/dm^2, γ = 50 %, f = 1 Hz

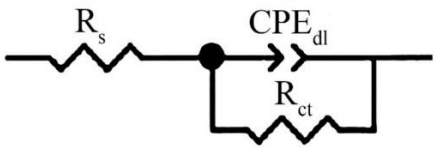

Figure 13. The equivalent circuit for fitting the EIS curves of pure Ni and Ni-B_4C coating

The values obtained by fitting the EIS curves are reported in Table 8. The table compares the pure nickel coating with the Ni-B_4C coating specimen, which exhibits the lowest corrosion current density (as presented in Table 7). The coatings were deposited under the conditions of **i = 1 A/dm², γ = 50%, f = 10 Hz** for the baseline, and **i = 1 A/dm², γ = 50%, f = 1 Hz** for the sample with minimum corrosion current density. This comparison highlights the enhanced corrosion resistance observed in the Ni-B_4C nanocomposite coating due to the optimized electrodeposition parameters.

Table 8. The electrochemical parameters obtained from the EIS analysis via the fitting curve.

Sample	R_s (Ω.cm^2)	R_{ct} (Ω.cm^2)	CPE_{dl} or Y_0 (s^n.cm^{-2}.Ω^{-1})	n
Pure Nickel (*i* = 1 A/dm^2, γ = 50 %, f = 10 Hz)	5.752	5504	3.18 × 10^{-5}	0.943
Ni-B_4C (*i* = 1 A/dm^2, γ = 50 %, f = 1 Hz)	4.744	13517	1.47 × 10^{-5}	0.935

According to Table 8, incorporating B_4C into the nickel matrix, along with lowering the pulse frequency, led to a significant increase in the charge transfer resistance (**Rct**) from 5504 Ω.cm² for pure nickel to 13515 Ω.cm² for the Ni-B_4C coating. This rise in **Rct** indicates a notable improvement in corrosion resistance, aligning with the results of corrosion current density and corrosion rate (as seen in Table 7). The reduction in the double-layer constant phase element (**CPE_{dl}**) further supports this enhancement in **Rct** and overall corrosion resistance. The **n** value, which remained close to 1, signifies near-ideal electrochemical behavior (refer to Figure 12 and Table 8).

CONCLUSION

In this study, pure nickel and Ni-B_4C nanocomposite coatings were synthesized using the pulse electrodeposition (PE) technique. The effects of B_4C nanoparticle incorporation and pulse parameters—such as pulse current density, duty cycle, and pulse frequency—on the coatings' microstructure, morphology, and nanoparticle distribution were analyzed through EDS, FESEM, and XRD methods. The corrosion behavior of the coatings was also assessed via potentiodynamic polarization and electrochemical impedance spectroscopy (EIS). Key findings include:

1) Electrodeposition was conducted with a baseline of **i = 1 A/dm², γ = 50%, f = 10 Hz**.
2) The addition of B_4C nanoparticles changed the nickel coating's morphology from a pyramid-like structure to a spherical (nodular) form.
3) Increasing the pulse current density from **1 to 4 A/dm²** reduced the incorporation of B_4C from **5.5 to 2.9 vol.%**, while increasing the duty cycle from **25% to 50%** and pulse frequency from **1 to 10 Hz** boosted B_4C incorporation from **4.6 vol.%** and **3.9 vol.%** to **5.5 vol.%**, respectively.
4) The incorporation of B_4C nanoparticles reduced the crystallite size of nickel for the **(111)** and **(200)** crystal planes from **73.2 to 32 nm** and **44.7 to 23 nm**, respectively.

5) The incorporation of B_4C nanoparticles increased the corrosion current density from **2.301 to 4.541 µA/cm²** under baseline conditions.
6) The lowest corrosion current density of **0.559 µA/cm²** (indicating the best corrosion resistance) was observed in the Ni-B_4C coating deposited under **i = 1 A/dm², γ = 50%, f = 1 Hz**. Increasing the pulse current density from **1 to 4 A/dm²** and the duty cycle from **25% to 50%** significantly reduced the corrosion current density from **4.541 to 1.375 µA/cm²** and from **7.243 to 4.541 µA/cm²**, respectively. Conversely, raising the pulse frequency from **1 to 10 Hz** increased the corrosion current density from **0.599 to 4.541 µA/cm²**, despite a rise in B_4C incorporation from **3.9 to 5.5 vol.%** due to a more uniform nanoparticle distribution at **1 Hz**.
7) The Ni-B_4C coating deposited at **1 Hz** demonstrated a higher **Rct** compared to the pure nickel coating, aligning with both EIS and potentiodynamic polarization results.

REFERENCES

1. Raghavendra, C. R., Basavarajappa, S., & Sogalad, I. (2018). Electrodeposition of Ni-nano composite coatings: a review. *Inorganic and Nano-Metal Chemistry*, *48*(12), 583-598. https://doi.org/10.1080/24701556.2019.1567537
2. Mahidashti, Z., Aliofkhazraei, M., & Lotfi, N. (2018). Review of nickel-based electrodeposited tribo-coatings. *Transactions of the Indian Institute of Metals*, *71*, 257-295. https://doi.org/10.1007/s12666-017-1175-x
3. Sajjadnejad, M., Omidvar, H., Javanbakht, M., & Mozafari, A. (2017). Textural and structural evolution of pulse electrodeposited Ni/diamond nanocomposite coatings. *Journal of Alloys and Compounds*, *704*, 809-817. https://doi.org/10.1016/j.jallcom.2016.12.318
4. Sajjadnejad, M., Haghshenas, S.M.S., Mehr Monjezi, M. (2022).Assessment of Failure Mechanisms in an Industrial Firewater Pipeline: A Case Study. *Advanced Journal of Chemistry-Section A*, *5(2)*, 81-93. https://doi.org/10.22034/ajca.2022.324623.1298
5. Sahab, A. R. M., Saad, N. H., Kasolang, S., & Saedon, J. (2012). Impact of plasma spray variables parameters on mechanical and wear behaviour of plasma sprayed Al2O3 3% wt TiO2 coating in abrasion and erosion application. *Procedia Engineering*, *41*, 1689-1695. https://doi.org/10.1016/j.proeng.2012.07.369
6. Luo, L., Yao, J., Li, J., & Yu, J. (2009). Preparation and characterization of sol–gel Al2O3/Ni–P composite coatings on carbon steel. *Ceramics International*, *35*(7), 2741-2745. https://doi.org/10.1016/j.ceramint.2009.03.019
7. Ba, K., Chahine, A., Ebn Touhami, M., Alauzun, J. G., & Manseri, A. (2020). Preparation and characterization of phosphate-nickel-titanium composite coatings obtained by sol–gel process for corrosion protection. *SN Applied Sciences*, *2*, 1-13. https://doi.org/10.1007/s42452-020-2173-x
8. Sajjadnejad, M., & Karimi Abadeh, H. (2019). Kinetics of photocatalytic degradation of methylene blue on nanostructured TiO2 coatings created by sol-gel process. *Advanced Ceramics Progress*, *5*(1), 1-8. https://doi.org/10.30501/acp.2019.93123
9. Bolelli, G., Berger, L. M., Bonetti, M., & Lusvarghi, L. (2014). Comparative study of the dry sliding wear behaviour of HVOF-sprayed WC–(W, Cr) 2C–Ni and WC–CoCr hardmetal coatings. *Wear*, *309*(1-2), 96-111. https://doi.org/10.1016/j.wear.2013.11.001
10. Bose, K., Wood, R. J. K., & Wheeler, D. W. (2005). High energy solid particle erosion mechanisms of superhard CVD coatings. *Wear*, *259*(1-6), 135-144. https://doi.org/10.1016/j.wear.2005.02.043
11. Grzesik, W., Zalisz, Z., Krol, S., & Nieslony, P. (2006). Investigations on friction and wear mechanisms of the PVD-TiAlN coated carbide in dry sliding against steels and cast iron. *Wear*, *261*(11-12), 1191-1200. https://doi.org/10.1016/j.wear.2006.03.004
12. Karmakar, R., Maji, P., & Ghosh, S. K. (2021). A review on the nickel based metal matrix composite coating. *Metals and Materials International*, *27*, 2134-2145. https://doi.org/10.1007/s12540-020-00872-w
13. Low, C. T. J., Bello, J. O., Wharton, J. A., Wood, R. J. K., Stokes, K. R., & Walsh, F. C. (2010). Electrodeposition and tribological characterisation of nickel nanocomposite coatings reinforced with nanotubular titanates. *Surface and Coatings Technology*, *205*(7), 1856-1863. https://doi.org/10.1016/j.surfcoat.2010.08.054
14. Sajjadnejad, M., Mozafari, A., Omidvar, H., & Javanbakht, M. (2014). Preparation and corrosion resistance of pulse electrodeposited Zn and Zn–SiC nanocomposite coatings. *Applied Surface Science*, *300*, 1-7. https://doi.org/10.1016/j.apsusc.2013.12.143
15. Sajjadnejad, M., Omidvar, H., & Javanbakht, M. (2017). Influence of pulse operational parameters on pure nickel electrodeposits: Part II. Microhardness and corrosion resistance. *Surface Engineering*, *33*(2), 94-101. https://doi.org/10.1080/02670844.2015.1122140
16. Sajjadnejad, M., Omidvar, H., & Javanbakht, M. (2017). Influence of pulse operational parameters on electrodeposition, morphology and microstructure of Ni/nanodiamond composite coatings. *International Journal of Electrochemical Science*, *12*(5), 3635-3651. https://doi.org/10.20964/2017.05.52
17. Sajjadnejad, M., Setoudeh, N., Mozafari, A., Isazadeh, A., & Omidvar, H. (2017). Alkaline electrodeposition of Ni–ZnO nanocomposite coatings: effects of pulse electroplating parameters. *Transactions of the Indian Institute of Metals*, *70*, 1533-1541. https://doi.org/10.1007/s12666-016-0950-4
18. Rajak, D. K., Wagh, P. H., Menezes, P. L., Chaudhary, A., & Kumar, R. (2020). Critical overview of coatings technology for metal matrix composites. *Journal of Bio-and Tribo-Corrosion*, *6*, 1-18. https://doi.org/10.1007/s40735-019-0305-x
19. Gül, H., Uysal, M., Akbulut, H., & Alp, A. (2014). Effect of PC electrodeposition on the structure and tribological behavior of Ni–Al2O3 nanocomposite coatings. *Surface and Coatings Technology*, *258*, 1202-1211. https://doi.org/10.1016/j.surfcoat.2014.07.002
20. Wang, L., Gao, Y., Xu, T., & Xue, Q. (2006). Corrosion resistance and lubricated sliding wear behaviour of novel Ni–P graded alloys as an alternative to hard Cr deposits. Applied Surface Science, 252(20), 7361-7372. https://doi.org/10.1016/j.apsusc.2005.08.040
21. Mehr, M. S., Akbari, A., & Damerchi, E. (2019). Electrodeposited Ni-B/SiC micro-and nano-composite coatings: a comparative study. Journal of Alloys and Compounds, 782, 477-487. https://doi.org/10.1016/j.jallcom.2018.12.184
22. Ma, C., He, H., Xia, F., Xiao, Z., & Liu, Y. (2023). Performance of Ni–SiC composites deposited using magnetic-field-assisted electrodeposition under different magnetic-field directions. Ceramics International, 49(22), 35907-35916. https://doi.org/10.1016/j.ceramint.2023.08.271
23. Paydar, S., Jafari, A., Bahrololoom, M. E., & Mozafari, V. (2015). Influence of BN and B4C particulates on wear and corrosion resistance of electroplated nickel matrix composite coatings. Tribology-Materials, Surfaces & Interfaces, 9(2), 105-110. https://doi.org/10.1179/1751584X15Y.0000000007
24. Zhang, Y., Zhang, S., He, Y., Li, H., He, T., Fan, Y., & Zhang, H. (2021). Mechanical properties and corrosion resistance of pulse electrodeposited Ni-B/B4C composite coatings. Surface and Coatings Technology, 421, 127458. https://doi.org/10.1016/j.surfcoat.2021.127458
25. Torkamani, A. D., Velashjerdi, M., Abbas, A., Bolourchi, M., & Maji, P. (2021). Electrodeposition of Nickel matrix composite coatings via various Boride particles: A review. Journal of Composites and Compounds, 3(7), 106-113. https://doi.org/10.52547/jcc.3.2.4

26. Mohajeri, S., Dolati, A., & Rezagholibeiki, S. (2011). Electrodeposition of Ni/WC nano composite in sulfate solution. Materials Chemistry and Physics, 129(3), 746-750. https://doi.org/10.1016/j.matchemphys.2011.04.053
27. Algul, H., Gul, H., Uysal, M., Alp, A., & Akbulut, H. (2015). Tribological properties of TiO 2 reinforced nickel based MMCs produced by pulse electrodeposition technique. *Transactions of the Indian Institute of Metals*, *68*, 79-87. https://doi.org/10.1007/s12666-014-0444-1
28. [28] Sajjadnejad, M., Karkon, S., & Haghshenas, S. M. S. (2024). Corrosion Characteristics of Zn-TiO_2 Nanocomposite Coatings Fabricated by Electro-Codeposition Process. *Advanced Journal of Chemistry, Section A*, *7*(2), 209-226. https://doi.org/10.48309/ajca.2024.418391.1425
29. Bahrololoom, M. E., & Sani, R. (2005). The influence of pulse plating parameters on the hardness and wear resistance of nickel–alumina composite coatings. Surface and Coatings Technology, 192(2-3), 154-163. https://doi.org/10.1016/j.surfcoat.2004.09.023
30. Refai, M., Hamid, Z. A., El-kilani, R. M., & Nasr, G. E. (2021). Electrodeposition of Ni–ZnO nano-composite for protecting the agricultural mower steel knives. Chemical Papers, 75, 139-152. https://doi.org/10.1007/s11696-020-01291-2
31. Sajjadnejad, M., Haghshenas, S. M. S., Targhi, V. T., Setoudeh, N., Hadipour, A., Moghanian, A., & Hosseinpour, S. (2021). Wear behavior of alkaline pulsed electrodeposited nickel composite coatings reinforced by ZnO nanoparticles. Wear, 468, 203591. https://doi.org/10.1016/j.wear.2020.203591
32. [32] Mirzamohammadi, S., Aliov, M. K., Sabur, A. R., & Hassanzadeh-Tabrizi, A. (2010). Study of wear resistance and nanostructure of tertiary Al 2 O 3/Y 2 O 3/CNT pulsed electrodeposited ni-based nanocomposite. Materials Science, 46, 76-86. https://doi.org/10.1007/s11003-010-9266-4
33. [33] Sajjadnejad, M., Abadeh, H. K., Omidvar, H., & Hosseinpour, S. (2020). Assessment of Tribological behavior of nickel-nano Si3N4 composite coatings fabricated by pulsed electroplating process. *Surface Topography: Metrology and Properties*, *8*(2), 025009. https://doi.org/10.1088/2051-672X/ab7ae5
34. Xia, F., Li, C., Ma, C., Li, Q., & Xing, H. (2021). Effect of pulse current density on microstructure and wear property of Ni-TiN nanocoatings deposited via pulse electrodeposition. Applied Surface Science, 538, 148139. https://doi.org/10.1016/j.apsusc.2020.148139
35. Xia, F., Yan, P., Ma, C., Wang, B., & Liu, Y. (2023). Effect of different heat-treated temperatures upon structural and abrasive performance of Ni-TiN composite nanocoatings. Journal of Materials Research and Technology, 27, 2874-2881. https://doi.org/10.1016/j.jmrt.2023.10.173
36. Algul, H., Tokur, M., Ozcan, S., Uysal, M., Çetinkaya, T., Akbulut, H., & Alp, A. (2015). The effect of graphene content and sliding speed on the wear mechanism of nickel–graphene nanocomposites. Applied Surface Science, 359, 340-348. https://doi.org/10.1016/j.apsusc.2015.10.139
37. [37] Mirzamohammadi, S., Khorsand, H., & Aliofkhazraei, M. (2017). Effect of different organic solvents on electrodeposition and wear behavior of Ni-alumina nanocomposite coatings. Surface and Coatings Technology, 313, 202-213. https://doi.org/10.1016/j.surfcoat.2017.01.025
38. Noorbakhsh Nezhad, A. H., Rahimi, E., Arefinia, R., Davoodi, A., & Hosseinpour, S. (2020). Effect of substrate grain size on structural and corrosion properties of electrodeposited nickel layer protected with self-assembled film of stearic acid. Materials, 13(9), 2052. https://doi.org/10.3390/ma13092052
39. Omidvar, H., Sajjadnejad, M., Stremsdoerfer, G., Meas, Y., & Mozafari, A. (2016). Composite NiB–graphite and NiB–PTFE surface coatings deposited by the dynamic chemical plating technique. Materials and Manufacturing Processes, 31(1), 24-30. https://doi.org/10.1080/10426914.2015.1004691
40. Saghafi, M., Mahboubi, F., Mohajerzadeh, S., & Holze, R. (2015). Preparation of Co-Ni oxide/vertically aligned carbon nanotube and their electrochemical performance in supercapacitors. Materials and Manufacturing Processes, 30(1), 70-78. https://doi.org/10.1080/10426914.2014.952026
41. Sajjadnejad, M., Omidvar, H., Javanbakht, M., & Mozafari, A. (2015). Characterization of pure nickel coatings fabricated under pulse current conditions. International Journal of Materials and Metallurgical Engineering, 9(8), 1061-1065. https://doi.org/10.5281/zenodo.1109912
42. Chawla, K. K., & Chawla, K. K. (1998). Metal matrix composites (pp. 164-211). Springer New York. https://doi.org/10.1007/978-1-4757-2966-5_6
43. Imanian Ghazanlou, S., Farhood, A. H. S., Ahmadiyeh, S., Ziyaei, E., Rasooli, A., & Hosseinpour, S. (2019). Characterization of pulse and direct current methods for electrodeposition of Ni-Co composite coatings reinforced with nano and micro ZnO particles. Metallurgical and Materials Transactions A, 50, 1922-1935. https://doi.org/10.1007/s11661-019-05118-y
44. Sajjadnejad, M., Haghshenas, S. M. S., Badr, P., Setoudeh, N., & Hosseinpour, S. (2021). Wear and tribological characterization of nickel matrix electrodeposited composites: A review. Wear, 486, 204098. https://doi.org/10.1016/j.wear.2021.204098
45. Dehgahi, S., Amini, R., & Alizadeh, M. (2016). Corrosion, passivation and wear behaviors of electrodeposited Ni–Al2O3–SiC nano-composite coatings. Surface and Coatings Technology, 304, 502-511. https://doi.org/10.1016/j.surfcoat.2016.07.007
46. Thiemig, D., & Bund, A. (2009). Influence of ethanol on the electrocodeposition of Ni/Al2O3 nanocomposite films. Applied Surface Science, 255(7), 4164-4170. https://doi.org/10.1016/j.apsusc.2008.10.114
47. Tabakovic, I., & Venkatasamy, V. (2018). Preparation of metastable CoFeNi alloys with ultra-high magnetic saturation (Bs= 2.4–2.59 T) by reverse pulse electrodeposition. Journal of Magnetism and Magnetic Materials, 452, 306-314. https://doi.org/10.1016/j.jmmm.2017.12.003
48. Yar-Mukhamedova, G., Sakhnenko, N., & Nenastina, T. (2018). Electrodeposition and properties of binary and ternary cobalt alloys with molybdenum and tungsten. Applied Surface Science, 445, 298-307. https://doi.org/10.1016/j.apsusc.2018.03.171
49. Li, B., Zhang, W., Zhang, W., & Huan, Y. (2017). Preparation of Ni-W/SiC nanocomposite coatings by electrochemical deposition. Journal of Alloys and compounds, 702, 38-50. https://doi.org/10.1016/j.jallcom.2017.01.239
50. Frade, T., Bouzon, V., Gomes, A., & da Silva Pereira, M. I. (2010). Pulsed-reverse current electrodeposition of Zn and Zn-TiO2 nanocomposite films. Surface and Coatings Technology, 204(21-22), 3592-3598. https://doi.org/10.1016/j.surfcoat.2010.04.030
51. Chandrasekar, M. S., & Pushpavanam, M. (2008). Pulse and pulse reverse plating—Conceptual, advantages and applications. Electrochimica Acta, 53(8), 3313-3322. https://doi.org/10.1016/j.electacta.2007.11.054
52. Yang, Y., & Cheng, Y. F. (2013). Fabrication of Ni–Co–SiC composite coatings by pulse electrodeposition—Effects of duty cycle and pulse frequency. Surface and Coatings Technology, 216, 282-288. https://doi.org/10.1016/j.surfcoat.2012.11.059
53. Bai, Q., Zhang, L., Ke, L., Zhu, P., Ma, Y., Xia, S., & Zhou, B. (2020). The effects of surface chemical treatment on the corrosion behavior of an Al-B4C metal matrix composite in boric acid solutions at different temperatures. Corrosion Science, 164, 108356. https://doi.org/10.1016/j.corsci.2019.108356
54. Clinktan, R., Ramkumar, K. R., & Sivasankaran, S. (2020). Effect of boron carbide addition on strengthening mechanisms, cold workability and instantaneous strain hardening behaviour of Cu4Si14Zn nanocomposites. Materials Science and Engineering: A, 787, 139538. https://doi.org/10.1016/j.msea.2020.139538
55. Ramadoss, N., Pazhanivel, K., Ganeshkumar, A., & Arivanandhan, M. (2023). Microstructural, mechanical and corrosion behaviour of B4C/BN-reinforced Al7075 matrix hybrid composites. International Journal of Metalcasting, 17(1), 499-514. https://doi.org/10.1007/s40962-022-00791-z
56. Rezagholizadeh, M., Ghaderi, M., Heidary, A., & Monirvaghefi, S. M. (2015). The effect of B 4 C nanoparticles on the corrosion and tribological behavior of electroless Ni-BB 4 C composite coatings. Surface engineering and applied electrochemistry, 51, 18-24. https://doi.org/10.3103/S1068375515010135

57. Pushpanathan, D. P., Alagumurthi, N., & Devaneyan, S. P. (2020). On the microstructure and tribological properties of pulse electrodeposited Ni-B4C-TiC nano composite coating on AZ80 magnesium alloy. Surfaces and Interfaces, 19, 100465. https://doi.org/10.1016/j.surfin.2020.100465
58. Dong, S., Yang, Y., Liang, T., Ma, R., Du, A., Yang, M., Fan, Y., Zhao, Z., & Cao, X. (2021). Construction and corrosion resistance of Ni-B4C superhydrophobic composite coatings on Q235 steel. Surface and Coatings Technology, 422, 127551. https://doi.org/10.1016/j.surfcoat.2021.127551
59. Li, H., He, Y., Luo, P., Fan, Y., Yu, H., Wang, Y., He, T., Li, Z., & Zhang, H. (2021). Influence of pulse frequency on corrosion resistance and mechanical properties of Ni-W/B4C composite coatings. Colloids and Surfaces A: Physicochemical and Engineering Aspects, 629, 127436. https://doi.org/10.1016/j.colsurfa.2021.127436
60. Venses, G., Sivapragash, M., Kumar, T. S., & Rex, F. M. T. (2022). Optimisation of Corrosion behaviour and hardness of Ni-B4C Composite coated AZ31 Mg alloy using RSM. Surface Topography: Metrology and Properties, 10(1), 015033. https://doi.org/10.1088/2051-672X/ac577f
61. Baghal, S. L., Amadeh, A., Sohi, M. H., & Hadavi, S. M. M. (2013). The effect of SDS surfactant on tensile properties of electrodeposited Ni–Co/SiC nanocomposites. Materials Science and Engineering: A, 559, 583-590. https://doi.org/10.1016/j.msea.2012.08.145
62. Mosayebi, S., Rezaei, M., & Mahidashti, Z. (2020). Comparing corrosion behavior of Ni and Ni-Mo electroplated coatings in chloride mediums. Colloids and Surfaces A: Physicochemical and Engineering Aspects, 594, 124654. https://doi.org/10.1016/j.colsurfa.2020.124654
63. Razaghi, Z., Rezaei, M., & Tabaian, S. H. (2020). Electrochemical noise and impedance study on the corrosion of electroplated Ni-Cr coatings in HBF4 aqueous solution. Journal of Electroanalytical Chemistry, 859, 113838. https://doi.org/10.1016/j.jelechem.2020.113838
64. Surender, M., Balasubramaniam, R., & Basu, B. (2004). Electrochemical behavior of electrodeposited Ni–WC composite coatings. Surface and Coatings Technology, 187(1), 93-97. https://doi.org/10.1016/j.surfcoat.2004.01.030
65. [65] Baghery, P., Farzam, M., Mousavi, A. B., & Hosseini, M. (2010). Ni–TiO2 nanocomposite coating with high resistance to corrosion and wear. Surface and Coatings Technology, 204(23), 3804-3810. https://doi.org/10.1016/j.surfcoat.2010.04.061
66. Dini, J. W. (1998). The materials science of coatings and substrates. Metal Finishing, 50, 47. https://www.researchgate.net/profile/Zainab-Raheem-2/publication/334737122_ELECTRODEPOSITION_The_Materials_Science_of_Coatings_and_Substrates/links/5d3eaf514585153e592ab1ea/ELECTRODEPOSITION-The-Materials-Science-of-Coatings-and-Substrates.pdf
67. Ebrahimi, F., & Ahmed, Z. (2003). The effect of current density on properties of electrodeposited nanocrystalline nickel. Journal of Applied Electrochemistry, 33, 733-739. https://doi.org/10.1023/A:1025049802635
68. Rashidi, A. M., & Amadeh, A. (2010). Effect of electroplating parameters on microstructure of nanocrystalline nickel coatings. Journal of Materials Science & Technology, 26(1), 82-86. https://doi.org/10.1016/S1005-0302(10)60013-8
69. Chen, L., Wang, L., Zeng, Z., & Xu, T. (2006). Influence of pulse frequency on the microstructure and wear resistance of electrodeposited Ni–Al2O3 composite coatings. Surface and Coatings Technology, 201(3-4), 599-605. https://doi.org/10.1016/j.surfcoat.2005.12.008
70. Lajevardi, S. A., & Shahrabi, T. (2010). Effects of pulse electrodeposition parameters on the properties of Ni–TiO2 nanocomposite coatings. Applied Surface Science, 256(22), 6775-6781. https://doi.org/10.1016/j.apsusc.2010.04.088
71. Badr, P., Sajjadnejad, M., & Haghshenas, S. M. S. (2023). Influence of Incorporating B4C Nanoparticles and Pulse Electrodeposition Parameters on the Surface Morphology and Wear Behavior of Nickel Based Nanocomposite Coatings. *Progress in Chemical and Biochemical Research*, *6*(4), 292-313. https://doi.org/10.22034/pcbr.2023.394780.1261
72. Mustapha, S., Ndamitso, M. M., Abdulkareem, A. S., Tijani, J. O., Shuaib, D. T., Mohammed, A. K., & Sumaila, A. (2019). Comparative study of crystallite size using Williamson-Hall and Debye-Scherrer plots for ZnO nanoparticles. Advances in Natural Sciences: Nanoscience and Nanotechnology, 10(4), 045013. https://doi.org/10.1088/2043-6254/ab52f7
73. Li, B., Mei, T., Chu, H., Wang, J., Du, S., Miao, Y., & Zhang, W. (2021). Ultrasonic-assisted electrodeposition of Ni/diamond composite coatings and its structure and electrochemical properties. Ultrasonics Sonochemistry, 73, 105475. https://doi.org/10.1016/j.ultsonch.2021.105475
74. Tao, Y., Ma, F., Teng, M., Jia, Z., & Zeng, Z. (2019). Designed fabrication of super high hardness Ni-B-Sc nanocomposite coating for anti-wear application. Applied Surface Science, 492, 426-434. https://doi.org/10.1016/j.apsusc.2019.06.233
75. Amadeh, A., Rahimi, A., Farshchian, B., & Moradi, H. (2010). Corrosion behavior of pulse electrodeposited nanostructure Ni–SiC composite coatings. Journal of Nanoscience and Nanotechnology, 10(8), 5383-5388. https://doi.org/10.1166/jnn.2010.1931
76. Medelien, V. (2002). The influence of B4C and SiC additions on the morphological, physical, chemical and corrosion properties of Ni coatings. Surface and coatings Technology, 154(1), 104-111. https://doi.org/10.1016/S0257-8972(01)01703-0
77. Jiang, J. B., Liu, W. D., Zhang, L., Zhong, Q. D., Wang, Y., & Zhou, Q. Y. (2012). Electrodeposition and hardness and corrosion resistance propertie of Ni/nano-B4C composite coatings. Advanced Materials Research, 399, 2055-2060. https://doi.org/10.4028/www.scientific.net/AMR.399-401.2055
78. Omidvar, H., Sajjadnejad, M., Stremsdoerfer, G., Meas, Y., & Mozafari, A. (2015). Characterization of NiBP-graphite composite coatings deposited by dynamic chemical plating. Anti-Corrosion Methods and Materials, 62(2), 116-122. https://doi.org/10.1108/ACMM-11-2013-1320
79. Javidi, M., Haghshenas, S. M. S., & Shariat, M. H. (2020). CO2 corrosion behavior of sensitized 304 and 316 austenitic stainless steels in 3.5 wt.% NaCl solution and presence of H2S. Corrosion Science, 163, 108230. https://doi.org/10.1016/j.corsci.2019.108230

Advanced Ceramics Progress: Vol. 9, No. 3, (Summer 2023) 31-37

Materials and Energy Research Center
MERC

Contents lists available at ACERP

Advanced Ceramics Progress

Journal Homepage: www.acerp.ir

Original Research Article

Improvement in Austenitic Stainless Steel Implant via Dual-Layer Coating of TaN-DLC Using Sputtering and PACVD Methods

Aziz Noori [a b], Mohammad Javad Eshraghi [c]*

[a] *MSc Student, Department of Physics, Iran University of Science and Technology, Tehran, Iran.*
[b] *MSc Student, Department of semiconductors, Materials and Energy Research Center, Karaj, Iran.*
[c] *Associate Professor, Department of Semiconductors, Materials and Energy Research Center,Karaj, Iran.*

* Corresponding Author Email: m.eshraghi@merc.ac.ir (Mohammad Javad Eshraghi)

URL: https://www.acerp.ir/article_176463.html

ARTICLE INFO

Article History:

Received 12 May 2023
Received in revised form 7 July 2023
Accepted 30 July 2023

Keywords:

SS316L Implant,
Sputtering,
PACVD,
Dense Grains,
Adhesion Test

ABSTRACT

In order to improve the properties and performance of SS316L implants in the current study, their surface was coated using two methods of sputtering and Plasma-Assisted Chemical Vapor Deposition (PACVD). To this end, TaN and Diamond-Like Carbon (DLC) layers were applied using sputtering and PACVD methods, respectively. Structural examinations by Field-Emission Scanning Electron Microscopy (FESEM) showed that the TaN layer was formed in a compact and quasi-spherical morphology. The final DLC layer was also formed in a compact and spherical morphology. Raman spectroscopic results showed that the D and G peaks with suitable heights were at 1356 cm^{-1} and 1588 cm^{-1}, respectively, indicating the successful DLC formation. Atomic Force Microscopy (AFM) images indicated that the grain size was in the range of 20-35 nanometers, and the presence of very fine DLC grains contributed to reducing the surface roughness to Ra=1.02 µm, indicating a 67.5% reduction. Cell adhesion test results up to 48 hours confirmed the better performance of DLC than that of TaN. Thus, the TaN-DLC two-layer coating is introduced as a new coating that can be used to improve the performance of implants.

https://doi.org/10.30501/acp.2023.396200.1125

1. INTRODUCTION

Medical implants are recognized as one of the important innovations in medical industry. These implants are used as the therapeutic artificial substitutes for patients who are in need for replacement of their body parts caused by serious injuries or chronic diseases. To create high-quality and durable implants, there is a need to use materials that are compatible with the human body characterized by suitable mechanical properties such as strength, elasticity, and hardness as well as a designed structure that follows a method of production that incurs less cost and time. For example, implants are made from polymer, metal, ceramic, or a combination of these materials [1-3].

Implants made of biocompatible materials are one of the suitable solutions for temporary or permanent replacement of defective or damaged bones in the human body [4]. While medical-grade stainless steels are generally known for their corrosion resistance and high mechanical strength, their potential long-term lifespan and potential side effects such as the release of metal ions in the human body are an important concern. In recent years, SS316 has become one of the most widely used biomaterials for implants due to its easy design and manufacturing, good mechanical properties, and resistance to corrosion as well as its lower cost than

Please cite this article as: Noori, A., Eshraghi, M., "Improvement in Austenitic Stainless Steel Implant via Dual-Layer Coating of TaN-DLC Using Sputtering and PACVD Methods", ***Advanced Ceramics Progress***, Vol. 9, No. 3, (2023), 31-37. https://doi.org/10.30501/acp.2023.396200.1125

titanium alloys. However, its insufficient wear performance limits its direct use as a prosthesis [5,6]. One possible solution to prevent the destruction of implants is to use alternative materials such as polymeric and ceramic composites. These materials are highly resistant to wear that have high biocompatibility properties [7-8].

Research has shown that these materials can reduce the level of wear and consequently reduce the production of metal ions in the human body. Surface modification techniques enhance the resistance to the destruction of metal implant surfaces and improve biological materials [9-11]. Due to their unique physical and chemical properties, Diamond-Like Carbon (DLC) coatings are attractive alternative biocompatible coatings to their traditional counterparts. Since DLC is typically identified as an amorphous hydrogenated carbon (a-C:H) with hybridization of sp^2 and sp^3 bonds, they possess properties such as high hardness, low friction coefficient, good wear resistance, chemical inertness, and high electrical resistance [12-13]. Use of DLC coatings in biological implants proved to be quite useful due to several advantages such as their wear resistance, high load-bearing capacity, antibacterial properties, and ability to facilitate bone absorption. Additionally, these coatings can also act as a barrier to other biological materials and reduce their wear [12]. Therefore, their application as the biological coatings in medical implants is promising that can also improve the performance and longevity of implants. However, one of the drawbacks of the DLC coatings is their lack of adhesion. The formation of an interlayer of metal carbide or nitride (such as Ti, Ta, Si, etc.) can increase the adhesion of DLC coatings to the metal surface. This interlayer is usually created using Physical Vapor Deposition (PVD) or Chemical Vapor Deposition (CVD) [14-15]. This layer acts as a bridge between the DLC coating and metal surface and prevents the coating from separating from the metal surface, hence improved adhesion [16-17].

Wang et al. [18] demonstrated that adding a titanium carbide or nitride interlayer between steel and DLC film improved the bonding strength by increasing the Ti-C bonding strength due to the formation of strong covalent bonds between Ti and C. Lee [19] showed that use of duplex coatings significantly improved the tribological performance. In fact, the anti-wear performance of the duplex coatings is almost ten times higher than that of single-layer DLC films. In addition, duplex coatings have better resistance to damage than others. These improvements result from the combination of both mechanical and tribological properties of the interlayer. Wu's study [20] also showed that use of a Ti-C interlayer in a DLC film had a significant improvement in both wear resistance and friction coefficient. Moreover, this interlayer could reduce the scratch cracks and create greater adhesion. Overall, use of Ti-C interlayer helped improve the performance of the DLC film. The TaN coating, as an interlayer, can indeed modify the surface roughness and provide a smoother surface. This in turn allows the DLC coating to be applied on a more even and uniform surface. As a result, the DLC coating exhibits improved mechanical properties and better performance.

The aim of this study is to investigate the formation of the DLC coating in the absence of TaN interlayer as well as in the presence of TaN interlayer and to examine its biocompatibility.

2. MATERIALS AND METHODS

This research used SS316 stainless steel samples with the dimensions of 2x20x20 mm. Initially, the samples were grinded with sandpaper up to the number 5000 and then polished with 0.01-micrometer diamond paste for 30 minutes. The MSS160 RF magnetron sputtering device and a 99.999% pure Ta target were employed to coat the samples at the base pressure of 2.8×10^{-3} mbar, power of 185 W for 60 minutes, and temperature of 350 degrees Celsius with a 30Ar/10N2 gas mixture. Then, the samples were coated using the Hindivac MSPT12 PACVD system under the working pressure of 45 mTorr, power of 150 W, and deposition time of 60 minutes using a gas mixture of 3 Ar/1 C_2H_2.

To examine the structure of the samples, a TESCAN MIRA3 Field Emission Scanning Electron Microscope (FESEM) was used, and the surface roughness and topography of the samples were examined using an Atomic Force Microscope (AFM). To determine the type and amount of bonding, an Upright microscope (CW YAG: DPSS Nd laser model) at the power ranging from 10-90 mW, resolution of 6 cm^{-1}, and wavelength of 512 nm was used to investigate the bonding types and amounts.

In this study, the MG63 cells from the Pasteur Institute of Iran were prepared. The RPMI culture medium with 10% FBS serum was used for cell growth. The cells were then maintained in an incubator at 37 degrees of Celsius with the humidity of 95% and injected CO_2 level of 5%. The biocompatibility of each coating, cell survival rate, and growth were qualitatively tested using the MTT assay through which, the activity of the mitochondrial dehydrogenase enzymes in live cells was examined. In this test, the (MTT) solution is affected by the dehydrogenase enzymes present in the mitochondria of the cell and is converted into insoluble purple formazan. The amount of the produced formazan is naturally proportional to the number of live cells. The intensity of coloration is examined by a simple spectrophotometric test. DAPI staining was used to estimate the number of live cells on the coatings.

3. RESULTS AND DISCUSSION

Figure 1 illustrates the FESEM images of the cross-section surface of TaN coating formed by magnetron sputtering and a TaN-DLC bilayer coating created by the

combination of magnetron sputtering and PACVD methods. As evident in Figure 1(a), a uniform TaN coating with the thickness of about 700 nm was formed on the substrate. Given the nature of the magnetron sputtering process where nucleation occurs as a result of the ballistic atom bombardment towards the substrate, growth becomes universal, and there is no sign of the preferred growth [21]. In other words, the TaN coating grows uniformly on the underlying substrate.

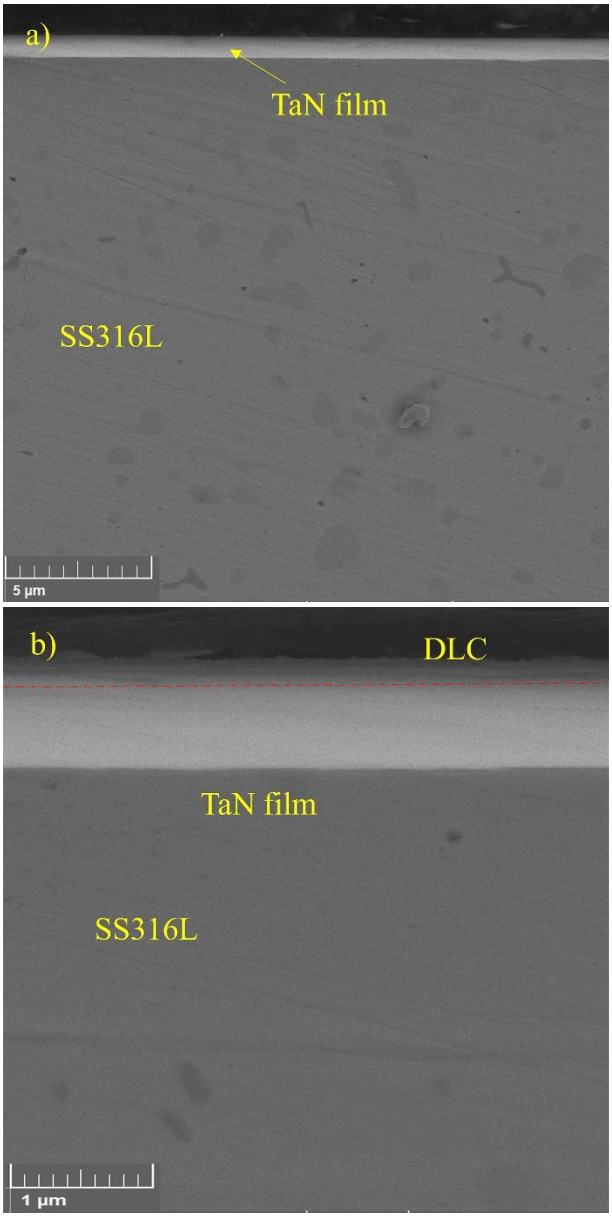

Figure 1. FESEM images of the cross-section surface of coatings: (a) TaN, and (b) TaN-DLC

This results in the homogeneity of the TaN coating, meaning that all points of the coating grow in the same manner and at the same rate. Figure 1(b) shows the formation of a thin DLC layer with an approximate thickness of 150 nm on the interlayer of TaN. As observed in the high magnification of this figure, the upper layer of the coating was formed completely uniformly. Accordingly, the TaN-DLC bilayer coating was formed on the SS316L substrate.

Figure 2 shows the FESEM surface morphology of the coatings. Since the magnetron sputtering process is a relatively fast process, the structure of the TaN coating can be amorphous, semi-crystalline, and crystalline with stable and semi-stable phases [22].

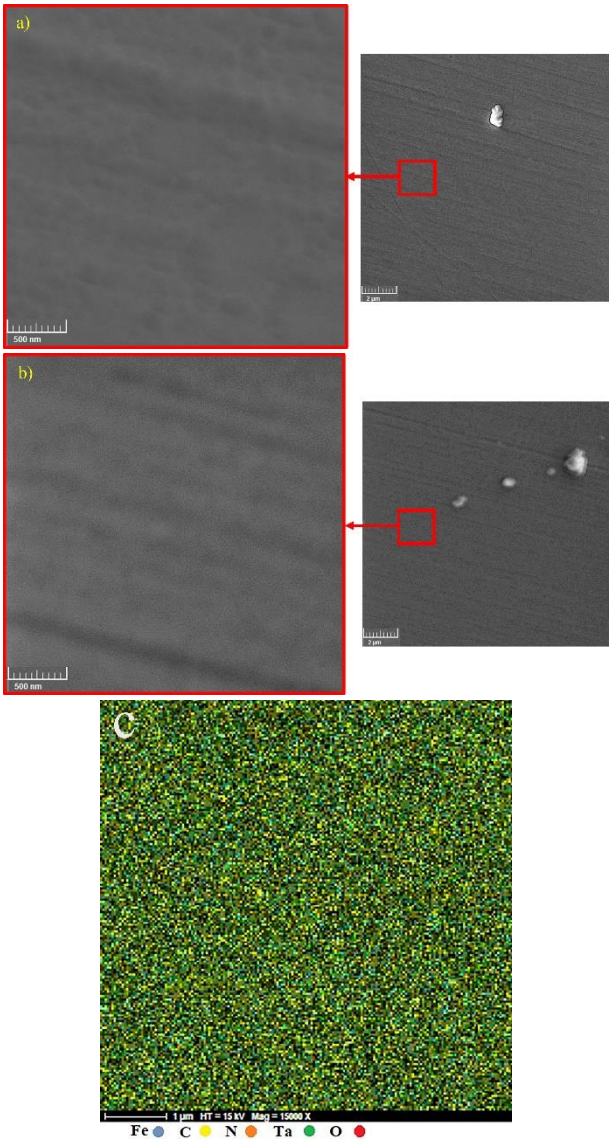

Figure 2. FESEM images of coating morphology: a) TaN, and b) TaN-DLC, and c) MAP of TaN-DLC.

Due to the high speed of the process, nucleation dominates over growth, and the coating grains, which are very uniform and small, form the coating morphology, as demonstrated in Figure 2(a).

There is no trace of grain or inconsistency in the magnified image. This indicates the formation of a healthy coating without any secondary phases or

impurities. Figure 2(b) also shows the morphology of the TaN-DLC coating. In this sample, the coating is completely uniform and devoid of any defects. Generally, since the thickness value in thin film coatings is quite small, the morphology of the coating is affected by the topography of the substrate. In fact, the grooves resulting from grinding and polishing make the coating cones grow in parallel bands. Since the grinding and polishing effects were less observed in the preparation of the substrate in this study, TaN and consequently DLC coatings were formed completely smoothly.

The TaN coating is formed as a result of bombardment by the ballistic launch of atoms on the surface, which appears as some natural pits or craters in the process. However, DLC coating is formed on the substrate surface based on vapor phase movement as a result of which, all the pores and grooves are filled. A comparison between both samples in Figure 2 shows that the number of grooves or craters in samples with TaN-DLC bilayer coating is less than that with TaN coating. This issue has an impact on the surface roughness, which will be discussed further below.

Typically, thin film coatings of Ta are formed in a columnar structure on the substrate; this is the reason why their morphology appears in spherical or semi-spherical forms. However, followed by addition of C and N and formation of TaC or TaN, due to the high density of the resulting coating, there will be no sign of a columnar structure in the microscopical images of the cross-sectional surface. The FESEM images of the cross-sectional surface in Figure 1 can prove this statement.

In the present study, interstitial N atom in Ta atoms of dense coating causes an enhancement in the mechanical coating properties. On the contrary, incorporation of N into the system leads to a distortion in the lattice, which on the one hand prevents the growth of coating grains and on the other hand, increases the mechanical properties of the system due to its fine structure. The distortion or strain created in the lattice results in a severe plastic deformation within the lattice. This process, along with the high speed of the coating process, i.e., rapid ballistic bombardment of Ta atoms, creates a localized amorphous field within the structure. In fact, the created coating is a combination of crystalline and amorphous structures, as already proven in previous studies [23,24]. The conditions needed for the formation of the TaN phase with long-range order cannot be provided by the combination of amorphous and crystalline phases. In other words, the non-observance state of the morphology of the coating results from several reasons such as the high volume of the amorphous phase, severe fineness, and removal of columnar structure, all indicating the formation of a dense coating.

The presence of both crystalline and amorphous phases in the coating creates a balance between softness and brittleness, hence an increase in the mechanical properties. Amorphous phases improve both corrosion resistance and toughness while crystalline phases enhance the hardness and strength. As the grain size and crystallite size decrease, the grain boundary suppression and mismatch increase, ultimately resulting in an increase in hardness [24]. Lack of coherence between the coating phases through the creation of anti-phase boundaries also leads to an increase in hardness.

DLC coating morphology includes carbon nanoclusters. These clusters are formed by the extensive aggregation of carbon atoms on the interlayer of TaN. The slow deposition rate in PACVD facilitates the formation of larger clusters, as shown in Figure 2(b). This phenomenon is consistent with the results from the previous research [25]. The FESEM image in Figure b(2) shows the formation of very small grains in the nanometer order, which undoubtedly affects the roughness and mechanical properties of the coating.

Figure 3 shows the Raman pattern of the thin DLC layer formed on the interlayer of TaN. As demonstrated in this image, the peak D is formed at 1356 cm^{-1}, indicating simple bonds between the carbon-carbon atoms, and the band peak G is formed at 1588 cm^{-1}, indicating vibrations of the six-membered carbon rings. These two peaks, along with these two characteristics, are indicative of the successful formation of the thin DLC layer [26,28].

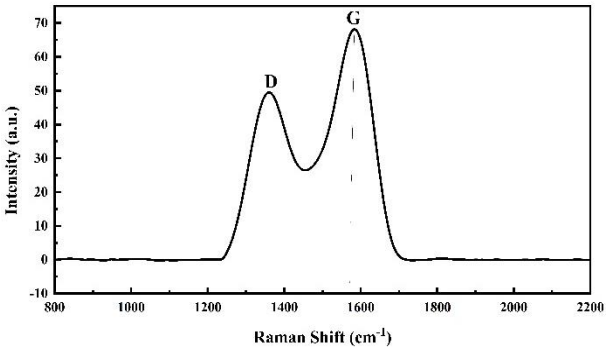

Figure 3. Raman spectroscopy pattern of the thin DLC film on the TaN interlayer

A prominent peak G can be detected in the graph in Figure 3 due to the tension of the bond bands of all sp^2 paired atoms in the rings and chains of the structure. The low-height peak D also indicates the vibrational modes of sp^2 atoms in the ring structure. The position of the peak G is of great importance since it affects the I_D/I_G and sp^2/sp^3 ratios [28]. As the sp^2/sp^3 ratio increases, the position of the peak G also alters, compared to the ID/IG ratio in an amorphous structure. In general, the type of carbon obtained from ethylene prevents the growth of poly crystalline film and leads to the formation of amorphous DLC coating [29].

Upon reducing the value of peak G, the proportion of sp^3 linkages will change, and the breakage of graphite in the low coverage system will decrease. The sp^3 degree is

highly important because it indicates the presence of residual stress in the system and prevents the formation of large clusters in the DLC film, as shown in Figure 2(b). Proper clustering increases the value of the peak G and consequently increases the disorder in the system by increasing the sp^3 content and causes the formation of an amorphous structure. This happens while with an increase in the I_D/I_G ratio, less sp^3 content remains in the structure [30].

The presence of H_2 in the system increases the value of peak D, and the loss of H_2 also causes the DLC network to graphitize. During the coating process, H_2 molecules penetrate the coating in a reverse manner and leave the coating. At this moment, the non-bonding sp^2 atoms are connected to each other and form six-membered rings to minimize the energy within the system. Once the sp^2 atoms are rearranged, the occurrence of a short-range order and stability of the amorphous structure can be ensured [31].

Figure 4 illustrates the AFM images of the two samples, i.e., TaN and TaN/DLC.

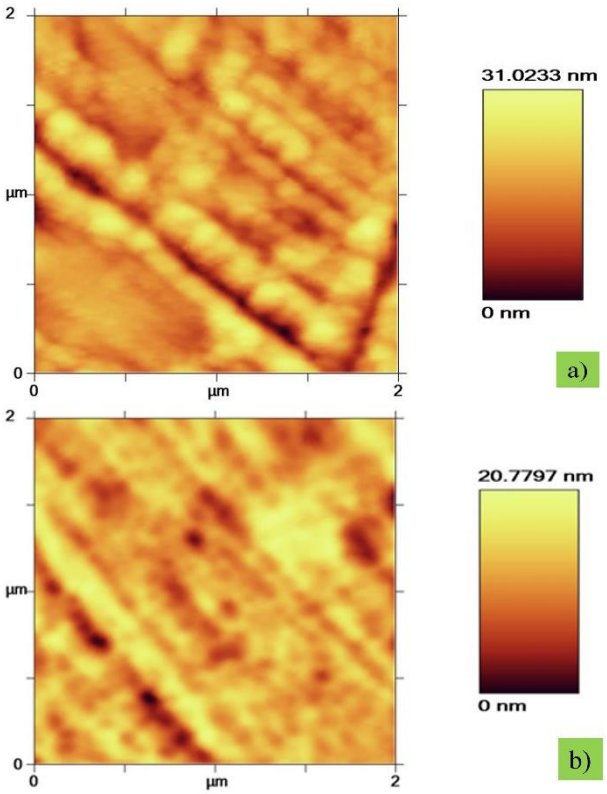

Figure 4. AFM images of coated samples: a) TaN, b) TaN-DLC

At the first glance, it is clear that the surface roughness can be reduced by applying the thin DLC layer. The grain size of TaN is about 30 nm with the surface roughness of Ra = 3.14 µm, which was later reduced by 21 nm and Ra = 1.02 µm after applying the DLC layer. The presence of the fine grains also leads to an increase in the strength and a decrease in the surface roughness mainly because the probability of obtaining the desired surface roughness is significantly reduced in the presence of uniform fine grains.

Figure 5 shows the adhesion, spreading, and morphology of the MG63 cells on two TaN and TaN-DLC samples after 48 hours of culture. As observed in this figure, the number of the remaining cells on the TaN-DLC sample is higher than that of the TaN sample. However, upon closer examination, it can be seen that the cells are growing and expanding very well and uniformly in all directions. On the surface of the TaN-DLC sample, mesenchymal cells are spreading and adhering to the substrate in all directions. This event marks the beginning of cell spread to the surface by filopodia which indicates a stronger cellular adhesion and better cell growth on the DLC layer than those of the TaN layer.

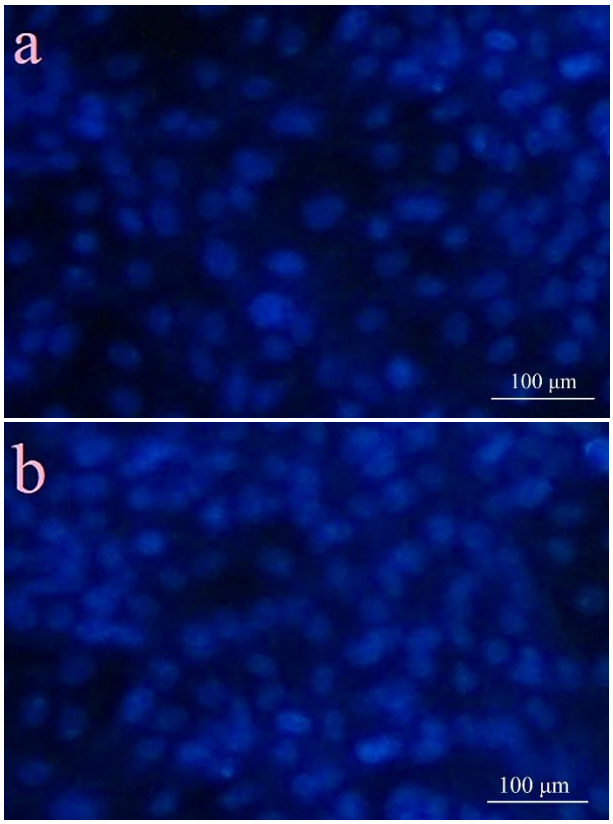

Figure 5. Fluorescent microscope images with DAPI staining of live cells a) TaN coating b) TaN-DLC coating

4. CONCLUSION(S)

The main findings of the current research are summarized in the following:

1. Once the two sputtering and PACVD methods are combined, it is possible to successfully produce a TaN-DLC bilayer coating on the SS316L substrate as a coating that can be used for an implant.
2. Both coating layers were formed uniformly with the surface roughness of Ra = 3.14 µm for the interlayer TaN layer and Ra = 1.02 µm for the top DLC layer, indicating a 67.5% reduction in the surface

roughness.
3. Both coating layers were formed with nanoscale quasi-spherical nodules.
4. The higher surface smoothness of the DLC coating resulted from its much finer grains as well as its wider amorphous range than those of TaN.
5. The DLC surface showed significantly better adhesion and cell growth for MG63 cells.

ACKNOWLEDGMENTS

This research work was supported by a research Grant (No.G282839) from Materials and Energy Research Center (MERC), Karaj, Iran

REFERENCES

1. Singh, D., Singh, R., Boparai, K. S., Farina, I., Feo, L., & Verma, A. K. (2018). "In-vitro studies of SS 316 L biomedical implants prepared by FDM, vapor smoothing and investment casting" ***Composites Part B: Engineering***, 132, 107-114. https://doi.org/10.1016/j.compositesb.2017.08.019
2. Gurappa, I. (2002). "Characterization of different materials for corrosion resistance under simulated body fluid conditions" ***Materials Characterization***, 49(1), 73-79. https://doi.org/10.1016/S1044-5803(02)00320-0
3. Okazaki, Y., & Gotoh, E. (2008). "Metal release from stainless steel, Co–Cr–Mo–Ni–Fe and Ni–Ti alloys in vascular implants" ***Corrosion Science***, 50(12), 3429-3438. https://doi.org/10.1016/j.corsci.2008.09.002
4. Wang, N., Dheen, S. T., Fuh, J. Y. H., & Kumar, A. S. (2021). "Cytotoxicity of Ti/SS316/Mg Particles on Human Osteoblasts" ***In Materials Science Forum*** (Vol. 1047, pp. 128-133). Trans Tech PublicationsLtd. https://doi.org/10.4028/www.scientific.net/MSF.1047.128
5. Thakur, A., Kumar, A., Kaya, S., Marzouki, R., Zhang, F., & Guo, L. (2022). "Recent advancements in surface modification, characterization and functionalization for enhancing the biocompatibility and corrosion resistance of biomedical implants" ***Coatings***, 12(10), 1459. https://doi.org/10.3390/coatings12101459
6. Chakraborty, R., Sengupta, S., Saha, P., Das, K., & Das, S. (2016). "Synthesis of calcium hydrogen phosphate and hydroxyapatite coating on SS316 substrate through pulsed electrodeposition" ***Materials Science and Engineering: C***, 69, 875-883. https://doi.org/10.1016/j.msec.2016.07.044
7. Harun, W. S. W., Asri, R. I. M., Alias, J., Zulkifli, F. H., Kadirgama, K., Ghani, S. A. C., & Shariffuddin, J. H. M. (2018). "A comprehensive review of hydroxyapatite-based coatings adhesion on metallic biomaterials", ***Ceramics International***, 44(2), 1250-1268. https://doi.org/10.1016/j.ceramint.2017.10.162
8. Qin, W., Kolooshani, A., Kolahdooz, A., Saber-Samandari, S., Khazaei, S., Khandan, A., & Toghraie, D. (2021). "Coating the magnesium implants with reinforced nanocomposite nanoparticles for use in orthopedic applications" ***Colloids and Surfaces A: Physicochemical and Engineering Aspects***, 621, 126581. https://doi.org/10.1016/j.colsurfa.2021.126581
9. Correa, D. R. N., Rocha, L. A., Donato, T. A. G., Sousa, K. S. J., Grandini, C. R., Afonso, C. R. M., & Hanawa, T. (2020). "On the mechanical biocompatibility of Ti-15Zr-based alloys for potential use as load-bearin". https://doi.org/10.1016/j.jmrt.2019.11.051
10. Focșăneanu, S. C., Vizureanu, P., Sandu, A. V., & Bălțatu, M. S. (2017). "Zirconia dental implant materials" ***In Materials Science Forum*** (Vol. 907, pp. 99-103). Trans Tech Publications Ltd. https://doi.org/10.4028/www.scientific.net/MSF.907.99
11. Abdullah, H. A., Al-Ghaban, A., & Anaee, R. (2021). "Deposition of CeO_2/TCP thin film on stainless steel 316 L by RF sputtering" ***Engineering and Technology Journal***, 39(4), 625-631. https://doi.org/10.30684/etj.2021.168140
12. Allen, M., Myer, B., & Rushton, N. (2001). "In vitro and in vivo investigations into the biocompatibility of diamond-like carbon (DLC) coatings for orthopedic applications" ***Journal of Biomedical Materials Research***, 58(3), 319-328. https://doi.org/10.1002/1097-4636(2001)58:3%3C319::AID-JBM1024%3E3.0.CO;2-F
13. Jelínek, M., Smetana, K., Kocourek, T., Dvořánková, B., Zemek, J., Remsa, J., & Luxbacher, T. (2010). "Biocompatibility and sp3/sp2 ratio of laser created DLC films" ***Materials Science and Engineering: B***, 169(1-3), 89-93. https://doi.org/10.1016/j.mseb.2010.01.010
14. Song, R., Chen, S., Liu, Z., Huo, C., & Chen, Q., "Effect of W-doping on the structure and properties of DLC films prepared by combining physical and chemical vapor deposition", ***Diam. Relat. Mater***., (2023), 109687. https://doi.org/10.1016/j.diamond.2023.109687
15. Huang, B., Liu, L.T., Han, S., Du, H.M., Zhou, Q, & Zhang, E.G., "Effect of deposition temperature on the microstructure and tribological properties of Si-DLC coatings prepared by PECVD", ***Diam. Relat. Mater***., 129 (2022), 109345. https://doi.org/10.1016/j.diamond.2022.109345
16. Y. Su, X. Gui, D. Xie, S.Y. Li, H. Sun, Y. Leng, N. Huang, The "Effect of a TiN Interlayer on the Tribological Properties of Diamond-like Carbon Films Deposited on 7A04 Aluminum Alloy", ***IEEE Trans. Plasma Sci.***, 39 (2011) 3144–3148. https://doi.org/10.1109/TPS.2011.2169091
17. F. Cemin, L.T. Bim, C.M. Menezes, C. Aguzzoli, M.E.H. Maia da Costa, I.J.R. Baumvol, F. Alvarez, C. a. Figueroa, "On the hydrogenated silicon carbide (SiCx:H) interlayer properties prompting adhesion of hydrogenated amorphous carbon (a-C:H) deposited on steel", ***Vacuum***, 109 (2014) 180–183. https://doi.org/10.1016/j.vacuum.2014.07.015
18. Wang, Keliang, Hui Zhou, Kaifeng Zhang, Xingguang Liu, Xingguo Feng, Yanshuai Zhang, Gong Chen, and Yugang Zheng. "Effects of Ti interlayer on adhesion property of DLC films: A first principle study", ***Diamond and Related Materials***, 111 (2021): 108188. https://doi.org/10.1016/j.diamond.2020.108188
19. Li, W., Zhao, Y., He, D., Song, Q., Sun, X., Wang, S., Zhai, H., Zheng, W. and Wood, R.J., 2022. "Optimizing mechanical and tribological properties of DLC/Cr3C2-NiCr duplex coating via tailoring interlayer thickness", ***Surface and Coatings Technology***, 434, p.128198. https://doi.org/10.1016/j.surfcoat.2022.128198
20. Wu, Y.M., Liu, J.Q., Cao, H.T., Wu, Z.Y., Wang, Q., Ma, Y.P., Jiang, H., Wen, F. and Pei, Y.T., 2020. "On the adhesion and wear resistance of DLC films deposited on nitrile butadiene rubber: A Ti-C interlayer". ***Diamond and Related Materials***, 101, p.107563. https://doi.org/10.1016/j.diamond.2019.107563
21. Samiee, M., Seyedraoufi, Z.S., Shajari, Y. and Eshraghi, M.J., 2020. "Effect of TiO_2 Thin Film Coating on AZ91D Alloy and Investigation of Corrosion Behavior, Mechanical Properties, and Biocompatibility", ***Journal of Bio-and Tribo-Corrosion***, 6, pp.1-10. https://doi.org/10.1007/s40735-020-00391-6
22. "Enhanced of Nano-mechanical Properties of NiTi Alloy by Applied Nanostructured Tantalum Nitride Coating with Magnetron Sputtering method", ***Iranian Journal of Ceramic Science & Engineering***, 2020; 8 (4) :15-27 URL: http://ijcse.ir/article-1-736-fa.html
23. Yang, Y.H., Chen, D.J. and Wu, F.B., 2016. "Microstructure, hardness, and wear resistance of sputtering TaN coating by controlling RF input power", ***Surface and Coatings Technology***, 303, pp.32-40. https://doi.org/10.1016/j.surfcoat.2016.03.034
24. Liu, K.Y., Lee, J.W. and Wu, F.B., 2014. "Fabrication and tribological behavior of sputtering TaN coatings", ***Surface and Coatings Technology***, 259, pp.123-128. https://doi.org/10.1016/j.surfcoat.2014.03.024
25. Zeng, C., Chen, Q., Xu, M., Deng, S., Luo, Y. and Wu, T., 2017. "Enhancement of mechanical, tribological and morphological properties of nitrogenated diamond-like carbon films by gradient nitrogen doping", ***Diamond and Related Materials***, 76, pp.132-140. https://doi.org/10.1016/j.diamond.2017.05.004

26. Dwivedi, N., Kumar, S., Tripathi, R.K., Malik, H.K. and Panwar, O.S., 2011. "Field emission, morphological and mechanical properties of variety of diamond-like carbon thin films", ***Applied Physics A***, 105, pp.417-425. https://doi.org/10.1007/s00339-011-6556-0
27. Corbella, C., Pascual, E., Oncins, G., Canal, C., Andujar, J.L. and Bertrán, E., 2005. "Composition and morphology of metal-containing diamond-like carbon films obtained by reactive magnetron sputtering", ***Thin Solid Films***, 482(1-2), pp.293-298. https://doi.org/10.1016/j.tsf.2004.11.178
28. Calderon, N.Z., Ampuero, J.L., La Rosa-Toro, A., Gacitúa, W. and Pujada, B.R., 2020, May. "Dependence of the mechanical properties of Cr-DLC films on the acetylene flow and substrate bias", ***In Journal of Physics: Conference Series*** (Vol. 1558, No. 1, p. 012008). IOP Publishing. https://doi.org/10.1088/1742-6596/1558/1/012008
29. Chen, C., Tang, W., Li, X., Wang, W. and Xu, C., 2020. "Structure and cutting performance of Ti-DLC films prepared by reactive magnetron sputtering", ***Diamond and Related Materials***, 104, p.107735. https://doi.org/10.1016/j.diamond.2020.107735
30. Zeng, C., Chen, Q., Xu, M., Deng, S., Luo, Y. and Wu, T., 2017. "Enhancement of mechanical, tribological and morphological properties of nitrogenated diamond-like carbon films by gradient nitrogen doping", ***Diamond and Related Materials***, 76, pp.132-140. https://doi.org/10.1016/j.diamond.2017.05.004
31. Catena, Alberto, Qiaochu Guo, Michael R. Kunze, Simonpietro Agnello, Franco M. Gelardi, Stefan Wehner, and Christian B. Fischer, "Morphological and chemical evolution of gradually deposited diamond-like carbon films on polyethylene terephthalate: from subplantation processes to structural reorganization by intrinsic stress release phenomena", ***ACS applied materials & interfaces***, 8, no. 16 (2016): 10636-10646. https://doi.org/10.1021/acsami.6b

Advanced Ceramics Progress: Vol. 9, No. 3, (Summer 2023) 38-42

Materials and Energy Research Center
MERC

Contents lists available at ACERP

Advanced Ceramics Progress

Journal Homepage: www.acerp.ir

Original Research Article

Construction of 0D/3D $ZnWO_4$-MoS_2 Heterojunction with Enhanced Charge Carrier Separation for Decomposition of Organic Pollutants under Visible Light Irradiation

Mousa Farhadian [a]*, Allireza. Akbarpour [b]

[a] *Assistant Professor, Department of Materials Engineering, Faculty of Engineering, University of Maragheh, Maragheh, East Azerbayjan, Iran.*
[b] *Professor, Department of Materials Engineering, Faculty of Engineering, University of Maragheh, Maragheh, East Azerbayjan, Iran.*

* Corresponding Author Email: m.farhadian@maragheh.ac.ir (M. Farhadian) URL: https://www.acerp.ir/article_183888.html

ARTICLE INFO

Article History:

Received: 14 October 2023
Revised: 07 November 2023
Accepted: 26 November 2023

Keywords:
MoS_2,
$ZnWO_4$,
Photocatalyst,
Heterojunction

ABSTRACT

In the present research, 0D/3D $ZnWO_4$-MoS_2 heterojunction was prepared through a two-step hydrothermal procedure and applied for degradation of MB dye from aqueous solution under visible light irradiation. XRD and FESEM analyses were conducted to conform the successful incorporation of $ZnWO_4$ nanoparticles into the flowerlike MoS_2 structure. Based on the obtained results, heterojunction with 30% wt. of $ZnWO_4$ revealed the best photocatalytic performance compared to the other heterojunction samples. This improvement is mainly attributed to the p-n heterojunction effect where the photoinduced electrons and holes could can be effectively separated on the different semiconductors, thus facilitating the formation of radical active species and resulting in efficient enhancement of photocatalytic performance. Moreover, the results obtained from DRS analysis confirmed that visible light absorption of the heterojunction samples decreased as the $ZnWO_4$ content exceeded 30% wt., which corresponds to the shielding effect of the UV-responsive $ZnWO_4$ component. Hydroxyle radicals was determined as the main active species responsible for photodecomposition of MB.

https://doi.org/10.30501/acp.2023.419323.1136

1. INTRODUCTION

MoS_2 is a two-dimensional (2D) semiconductor material that has received significant attention owing to its unique properties [1,2]. As a photocatalyst, MoS_2 can absorb visible light energy to promote chemical reactions, making it a potential solution for energy conversion and environmental remediation. MoS_2 exhibits excellent catalytic activity due to its high surface area, strong adsorption ability, and tunable bandgap [3–5]. Additionally, its layered structure and strong interlayer interactions result in efficient charge separation and transfer [6]. MoS_2-based photocatalysts have been studied due to their wide applications in hydrogen evolution, water splitting, and degradation of organic pollutants [7]. Further research on MoS_2 as a photocatalyst may lead to the development of more efficient and sustainable technologies for various industrial and environmental applications [8]. Although MoS_2 has shown great potential as a photocatalyst, there are still some limitations that need to be addressed. Some of the notable limitations of MoS_2 as a photocatalyst include poor charge carrier mobility, limited light absorption, and chemical instability [9].

As an n-type semiconductor, $ZnWO_4$ has the ability to absorb Ultraviolent (UV) light energy to promote the chemical reactions and degrade the pollutants [10–12]. It enjoys some unique properties including high surface area, stability under harsh conditions, and efficient

Please cite this article as: Farhadian, M, Akbarpour, A. "Construction of 0D/3D ZnWO4-MoS2 heterojunction with enhanced charge carrier separation for decomposition of organic pollutants under solar light irradiation", Advanced Ceramics Progress, Vol. 9, No. 3, (2023), 38-42. https://doi.org/10.30501/acp.2023.419323.1136

charge separation, which contributes to its high photocatalytic activity [13]. The combination of $ZnWO_4$ with MoS_2 semiconductors can broaden the absorption spectrum, hence more solar energy consumption. In addition, the $ZnWO_4/MoS_2$ heterojunction can promote charge separation, leading to more efficient electron-hole pair generation. This happens mainly because $ZnWO_4$ has a higher conduction band position than MoS_2, which facilitates the transfer of electrons from MoS_2 to $ZnWO_4$. The combination of $ZnWO_4$ and MoS_2 can improve the stability and durability of the photocatalyst. $ZnWO_4$ has good chemical stability that protects MoS_2 from oxidation or corrosion under harsh reaction conditions [14]. Overall, application of $ZnWO_4$ as a co-catalyst with MoS_2 can lead to improved photocatalytic performance, enhanced charge separation and transfer, and elevated stability and durability.

In this study, 0D $ZnWO_4$ nanoparticles was loaded on 3D flowerlike MoS_2 microspheres and applied for decomposition of Methylen Blue (MB) dye from aqueous solution through simple hydrothermal method. The pure and hybrid photocatalysts were characterized, and their chemical, structural, and optical characteristics were examined.

2. MATERIALS AND METHODS

In this study, $(NH_4)_6Mo_7O_{27}$, CH_4N_2S, $Na_2WO_4.2H_2O$, $Zn(NO_3)_2{\cdot}6(H_2O)$, ammonia solution (25%), and ethanol were purchased from Merck (Germany) and used without further purification.

The flower-like MoS_2 microspheres were synthesized by a one-step hydrothermal reaction using hexaammonium heptamolybdate tetrahydrate and thiourea as the starting materials. In a typical synthesis, 1.24 g of hexaammonium heptamolybdate tetrahydrate and 2.28 g of thiourea were dissolved in 36 ml deionized water under vigorous stirring for 30 min to form a homogeneous solution. The solution was then transferred into a 50 ml Teflon-lined stainless-steel autoclave and sealed tightly, heated at 220 ^oC for 6 h and then, naturally cooled down to room temperature. Black precipitates were collected by centrifugation and washed with distilled water and absolute ethanol for several times, and finally dried in vacuum at 60 °C for 24 h.

To prepare $ZnWO_4/MoS_2$ heterojunction with various weight ratio of $ZnWO_4$ content, $Zn(NO_3)_2.6H_2O$, $Na_2WO_4.2H_2O$, and CTAB were dissolved in the mixed solution of DMF (40 ml)/H_2O (10 ml). Then, 0.4 g MoS_2 was added to the clear solution and ultrasonically treated for 1 h until a homogeneous mixture was obtained. It was then transformed to the teflon-lined stainless steel autoclave and heat-treated at 180 ^oC for 12 h. The final product was filtered, collected, washed three times with ethanol and deionized water, and then dried in vacuum oven at 80 ^oC for 12 h. The $ZnWO_4/MoS_2$ nanocomposites were denoted as 10ZM, 20ZM, 30ZM, and 40ZM, where the number represents the weight percent of loaded $ZnWO_4$ nanoparticles on the surface of MoS_2.

3. RESULTS AND DISCUSSION

3.1. FE-SEM images

Figure 1 represents the SEM images of MoS_2 flower-like microspheres and $ZnWO_4/MoS_2$ heterojuntion sample with 30 wt.% $ZnWO_4$ content (M30Z). As shown in Figures 1a and 1b, the hierarchical MoS_2 flowerlikes with approximately 1 μm in diameter are formed. In addition, $ZnWO_4$ nanoparticles of approximately 20 nm in diameter are homogeneously integrated among the MoS_2 layers, as demonstrated in Figures 1c and 1d. In these figures, the MoS_2 microflowers retained their original shapes after their combination with $ZnWO_4$ nanoparticles, representing excellent stability of the prepared MoS_2 hierarchical microstructures.

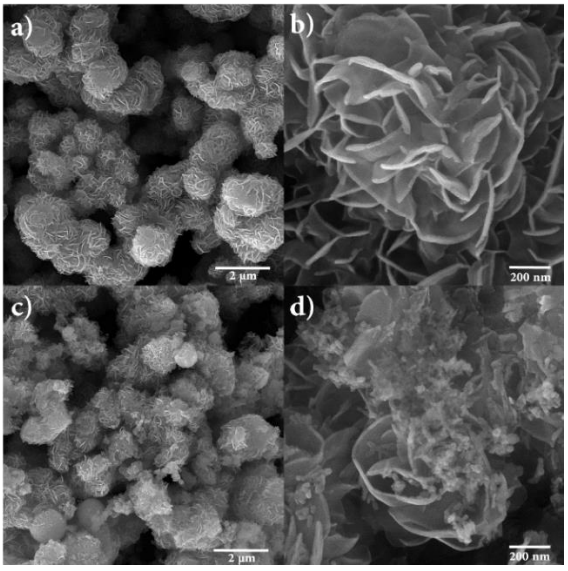

Figure 1. FESEM images of (a, b) MoS_2 microsphere and (c, d) $ZnWO_4/MoS_2$ heterojunction

3.2. XRD

XRD analysis was conducted to study the phase structure of the prepared samples. As seen in Figure 2, the peaks at 2θ=14.5° (002), 34.2° (100), 39.0° (103), 49.5° (105), and 59.0° (110) are attributed to the hexagonal structure of MoS_2 (JPCDS No.00.037-1492). The peaks observed in the XRD pattern of pure $ZnWO_4$ can be attributed to its monoclinic phase (JPCDS No.00.015-0774). Further, the detected peaks of $ZnWO_4$ appear in the XRD pattern of the heterojunction samples, indicating the successful combination of $ZnWO_4$ nanoparticles with the MoS_2 structure. No other peaks are detected in the XRD patterns of heterojunction samples, confirming the formation of the composite samples with no other impurities.

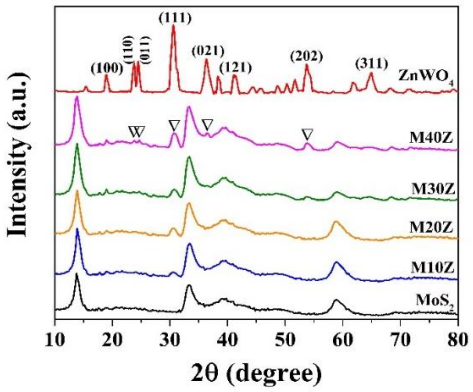

Figure 2. XRD patterns of the pure and heterojunction samples.

3.3 Optical properties

The optical properties of the prepared samples were measured by Diffuse Reflectance Spectroscopy (DRS). As observed in Figure 3, compared with pure MoS_2, the optical absorption edge of the heterojunction samples was shifted to the shorter wavelengths as the $ZnWO_4$ content increased which is attributed to the larger band gap of $ZnWO_4$, indicating the construction of heterojunction at the interface of MoS_2 and $ZnWO_4$. The energy band gap (E_g) of the samples was calculated using Kubelka-Munk equation $(\alpha h\upsilon)^n = A(h\upsilon - Eg)$, the obtained results of which are represented in Figure 4. Accordingly, Eg of heterojunction samples increased upon increasing the $ZnWO_4$ content, compared to pristine MoS_2. The presence of both MoS_2 with narrow band gap and $ZnWO_4$ as a UV-responsive semiconductor benefits broader light absorption and heterojunction effect, which ultimately improve the photocatalytic performance.

3.4 Photocatalytic activity

The photocatalytic performance of the samples was evaluated through photodecomposition of MB from aqueous solution under visible light irradiation. The obtained results are shown in Figure 5. Apparently, MoS_2 exhibits poor photocatalytic activity mainly due to the fast recombination rate of the electron-hole pairs, resulting from its narrow band gap. However, as $ZnWO_4$ is loaded on the surface of MoS_2 structure, the photodegradation activity is enhanced. This improvement results from the heterojunction effect where the produced electrons and holes in MoS_2 can be effectively separated and then, the lifespan of the charge carriers is prolonged, thus facilitating the formation of active species. As seen, photocatalytic decomposition of MB increased up to 30% wt. $ZnWO_4$ content and then decreased. Indeed, $ZnWO_4$ component is not able to absorb visible light spectrum due to its larger band gap. It seems that the higher ZWO_4 nanoparticles loading can cover the optical active sites of the MoS_2 hierarchical and decrease the visible light absorption (Figure 3), resulting in the degraded photocatalytic performance of the M40Z heterojunction sample. To evaluate the stability of the optimum sample (M30Z), recycling experiments were conducted and shown in Figure 6. The results revealed that the photocatalytic degradation percentage of the M30Z sample only decreased approximately 5%, showing good chemical stability.

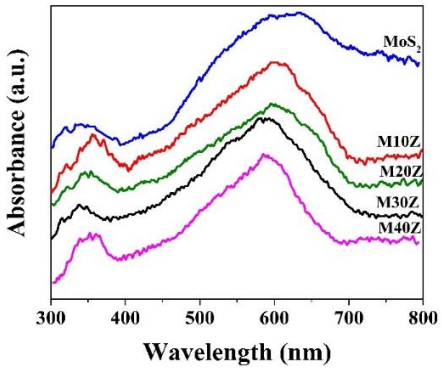

Figure 3. DRS plots of pure MoS_2 and prepared heterojunctions.

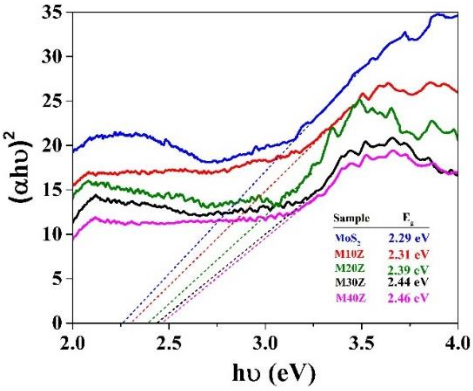

Figure 4. Tauc Plots of pure MoS_2 and prepared heterojunctions.

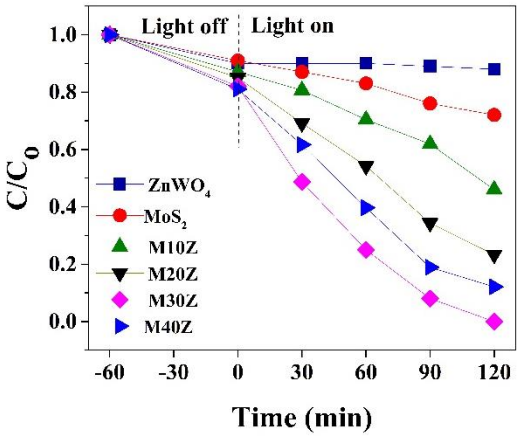

Figure 5. Photocatalytic decomposition of MB from aqueous solution over prepared pure and heterojunction samples under visible light irradiation.

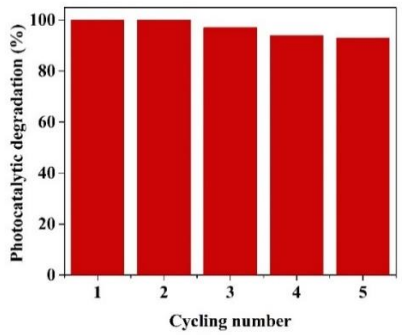

Figure 6. Recycling evaluation of M30Z sample toward MB decomposition under visible light irradiation.

3.5 Photocatalytic mechanism

To study the photocatalytic mechanism of the prepared heterojunction, radical trapping experiments were conducted to determine the active species responsible for the photocatalytic degradation of MB. To this end, triethanolamine (TEA), benzoquinone (BQ), and isopropyl alcohol (IPA) were separately added as the scavengers of holes, superoxide radicals and hydroxide radicals, respectively. As shown in Figure 7, the photodegradation of MB was slightly reduced in the presence of BQ, indicating that the superoxide radicals had no significant role in the photocatalytic decomposition of MB. In addition, the significant reduction in the photocatlytic performance in the presence of IPA denote that hydroxyle radicals are the main species for photodecomposition of MB. In addition, the photoinduced holes are also involved in the photodegradation of MB.

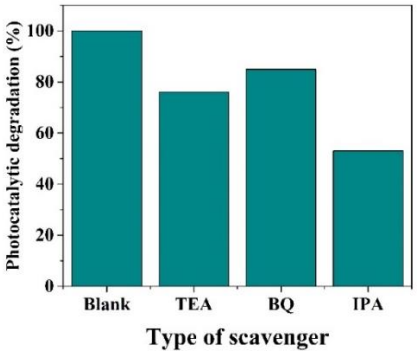

Figure 7. Photocatalytic degradation of MB in the presence of various scavengers.

4. CONCLUSION

In summary, hierarchical $ZnWO_4$-MoS_2 heterojunction samples with different $ZnWO_4$ contents were successfully prepared by a simple two-step hydrothermal method, and served toward photocatalytic degradation of MB dye from aqueous solutions under visible light irradiation. Based on the obtained results, $ZnWO_4$-MoS_2 heterojunction with 30 mol. % content of $ZnWO_4$ revealed 8.33 times enhancement after 120 min irradiation compared to pure MoS_2. This improvement is mainly attributed to the heterojunction effect during which, photoinduced electrons and holes over MoS_2 were effectively separated and easily participated for the radical species production. Further, recycling experiments showed that the fabricated $ZnWO_4$-MoS_2 revealed only around 5% reduction in the MB photodegradation which represents that sufficient numbers of bonding are formed at their interface. Further, the results indicated that hydroxyle radical along with the photoinduced holes are the main species toward photocatalytic degradation of MB. The obtained results verify that the prepared $ZnWO_4$-MoS_2 heterojunction can be a promising visible-light-activated photocatalyst for efficient degradation of dye contaminants from wastewater.

ACKNOWLEDGEMENTS

The author wish to acknowledge University of Maragheh for the all support throughout this work.

REFERENCES

1. Waghchaure, R. H., Adole, V. A., Jagdale, B. S., & Koli, P. B. (2022). Fe^{3+} modified zinc oxide nanomaterial as an efficient, multifaceted material for photocatalytic degradation of MB dye and ethanol gas sensor as part of environmental rectification. ***Inorganic Chemistry Communications***, 140, 109450. https://doi.org/10.1016/j.inoche.2022.109450
2. Khan, I., Saeed, K., Zekker, I., Zhang, B., Hendi, A. H., Ahmad, A., ... & Khan, I. (2022). Review on methylene blue: Its properties, uses, toxicity and photodegradation. ***Water***, 14(2), 242. https://www.mdpi.com/2073-4441/14/2/242#
3. Bahadoran, A., Farhadian, M., Hoseinzadeh, G., & Liu, Q. (2021). Novel flake-like Z-Scheme Bi_2WO_6-$ZnBi_2O_4$ heterostructure prepared by sonochemical assisted hydrothermal procedures with enhanced visible-light photocatalytic activity. ***Journal of Alloys and Compounds***, 883, 160895. https://doi.org/10.1016/j.jallcom.2021.160895
4. Koli, P. B., Kapadnis, K. H., Deshpande, U. G., & Patil, M. R. (2018). Fabrication and characterization of pure and modified Co_3O_4 nanocatalyst and their application for photocatalytic degradation of eosine blue dye: a comparative study. ***Journal of Nanostructure in Chemistry***, 8, 453-463. https://doi.org/10.1007/s40097-018-0287-0
5. Ahire, S. A., Bachhav, A. A., Jagdale, B. S., Patil, A. V., Koli, P. B., & Pawar, T. B. (2023). Amalgamation of ZrO_2-PANI Nanocomposite Polymeric Material: Characterization and Expeditious Photocatalytic Performance Towards Carbol Fuchsin (CF) Dye and Kinetic Study. ***Journal of Inorganic and Organometallic Polymers and Materials***, 33(5), 1357-1368. https://doi.org/10.1007/s10904-023-02590-3
6. Koli, P. B., Kapadnis, K. H., & Deshpande, U. G. (2019). Transition metal decorated Ferrosoferric oxide (Fe_3O_4): An expeditious catalyst for photodegradation of Carbol Fuchsin in environmental remediation. ***Journal of Environmental Chemical Engineering***, 7(5), 103373. https://doi.org/10.1016/j.jece.2019.103373
7. Koli, P. B., Shinde, S. G., Kapadnis, K. H., Patil, A. P., Shinde, M. P., Khairnar, S. D., ... & Ingale, R. S. (2021). Transition metal incorporated, modified bismuth oxide (Bi_2O_3) nano photo catalyst for deterioration of rosaniline hydrochloride dye as resource for environmental rehabilitation. ***Journal of the Indian Chemical Society***, 98(11), 100225. https://doi.org/10.1016/j.jics.2021.100225

8. Li, W., Wang, L., Zhang, Q., Chen, Z., Deng, X., Feng, C., ... & Sun, M. (2019). Fabrication of an ultrathin 2D/2D C_3N_4/MoS_2 heterojunction photocatalyst with enhanced photocatalytic performance. ***Journal of Alloys and Compounds***, 808, 151681. https://doi.org/10.1016/j.jallcom.2019.151681
9. Khalid, N. R., Kamal, M. R., Tahir, M. B., Rafique, M., Niaz, N. A., Ali, Y., ... & Muhammad, S. (2021). Fabrication of direct Z-scheme MoO_3/N–MoS_2 photocatalyst for synergistically enhanced H_2 production. ***International Journal of Hydrogen Energy***, 46(80), 39822-39829. https://doi.org/10.1016/j.ijhydene.2021.09.230
10. Li, Z., Meng, X., & Zhang, Z. (2018). Recent development on MoS_2-based photocatalysis: A review. Journal of Photochemistry and Photobiology C: ***Photochemistry Reviews***, 35, 39-55. https://doi.org/10.1016/j.jphotochemrev.2017.12.002
11. Sun, J., Li, X., Guo, W., Zhao, M., Fan, X., Dong, Y., ... & Fu, Y. (2017). Synthesis methods of two-dimensional MoS_2: A brief review. ***Crystals***, 7(7), 198. https://www.mdpi.com/2073-4352/7/7/198#
12. Liang, Z., Shen, R., Ng, Y. H., Zhang, P., Xiang, Q., & Li, X. (2020). A review on 2D MoS_2 cocatalysts in photocatalytic H_2 production. Journal of Materials Science & Technology, 56, 89-121. https://doi.org/10.1016/j.jmst.2020.04.032
13. Huang, S., Chen, C., Tsai, H., Shaya, J., & Lu, C. (2018). Photocatalytic degradation of thiobencarb by a visible light-driven MoS_2 photocatalyst. ***Separation and Purification Technology***, 197, 147-155. https://doi.org/10.1016/j.seppur.2018.01.009
14. Yuan, Y. J. *et al*. "The role of bandgap and interface in enhancing photocatalytic H_2 generation activity of 2D-2D black phosphorus/MoS_2 photocatalyst", ***Applied Catalysis B: Environmental***, Vol. 242, (2019), 1–8. https://doi.org/10.1016/j.apcatb.2018.09.100
15. Yuan, Y., Guo, R. T., Hong, L. F., Ji, X. Y., Li, Z. S., Lin, Z. D., & Pan, W. G. (2021). Recent advances and perspectives of MoS_2-based materials for photocatalytic dyes degradation: a review. Colloids and Surfaces A: Physicochemical and Engineering Aspects, 611, 125836. https://doi.org/10.1016/j.colsurfa.2020.125836
16. Cui, E., Yu, G., Huang, H., & Li, Z. (2017). Current advances in MoS_2/semiconductor heterojunction with enhanced photocatalytic activity. ***Current Opinion in Green and Sustainable Chemistry***, 6, 42-47. https://doi.org/10.1016/j.cogsc.2017.05.009
17. Abubakar, H. L., Tijani, J. O., Abdulkareem, S. A., Mann, A., & Mustapha, S. (2022). A review on the applications of zinc tungstate ($ZnWO_4$) photocatalyst for wastewater treatment. Heliyon. https://doi.org/10.1016/j.heliyon.2022.e09964
18. Fu, H., Lin, J., Zhang, L., & Zhu, Y. (2006). Photocatalytic activities of a novel $ZnWO_4$ catalyst prepared by a hydrothermal process. ***Applied Catalysis A: General***, 306, 58-67. https://doi.org/10.1016/j.apcata.2006.03.040
19. Andrade, A. O., da Silveira Lacerda, L. H., Júnior, M. L., Sharma, S. K., da Costa, M. M., Alves, O. C., ... & Almeida, M. A. (2023). Enhanced photocatalytic activity of BiOBr/$ZnWO_4$ heterojunction: A combined experimental and DFT-based theoretical approach. ***Optical Materials***, 138, 113701. https://doi.org/10.1016/j.optmat.2023.113701
20. Rathi, V., Panneerselvam, A., & Sathiyapriya, R. (2020). Graphitic carbon nitride (g-C_3N_4) decorated $ZnWO_4$ heterojunctions architecture synthesis, characterization and photocatalytic activity evaluation. ***Diamond and Related Materials***, 108, 107981. https://doi.org/10.1016/j.diamond.2020.107981
21. Atla, R., & Oh, T. H. (2021). Solar light-driven 2D MoS_2 nanoflake-supported 1D $ZnWO_4$ nanorod heterostructure: Efficient separation of charge carriers for removing toxic organic pollutants. ***Journal of Environmental Chemical Engineering***, 9(6), 106427. https://doi.org/10.1016/j.jece.2021.106427
22. Liang, L., Liu, H., Tian, Y., Hao, Q., Liu, C., Wang, W., & Xie, X. (2016). Fabrication of novel $CuWO_4$ hollow microsphere photocatalyst for dye degradation under visible-light irradiation. ***Materials Letters***, 182, 302-304. https://doi.org/10.1016/j.matlet.2016.05.166
23. Geetha, G. V., Sivakumar, R., Sanjeeviraja, C., & Ganesh, V. (2021). Photocatalytic degradation of methylene blue dye using $ZnWO_4$ catalyst prepared by a simple co-precipitation technique. ***Journal of sol-gel science and technology***, 97, 572-580. https://doi.org/10.1007/s10971-021-05480-7
24. Geetha, G. V., Keerthana, S. P., Madhuri, K., & Sivakumar, R. (2021). Effect of solvent volume on the properties of $ZnWO_4$ nanoparticles and their photocatalytic activity for the degradation of cationic dye. ***Inorganic Chemistry Communications***, 132, 108810. https://doi.org/10.1016/j.inoche.2021.108810
25. Rani, A., Singh, K., Patel, A. S., Chakraborti, A., Kumar, S., Ghosh, K., & Sharma, P. (2020). Visible light driven photocatalysis of organic dyes using SnO_2 decorated MoS_2 nanocomposites. ***Chemical Physics Letters***, 738, 136874. https://doi.org/10.1016/j.cplett.2019.136874
26. Kao, L. H., Chuang, K. S., Catherine, H. N., Huang, J. H., Hsu, H. J., Shen, Y. C., & Hu, C. (2023). MoS_2-coupled coniferous ZnO for photocatalytic degradation of dyes. ***Journal of the Taiwan Institute of Chemical Engineers***, 142, 104638. https://doi.org/10.1016/j.jtice.2022.104638

Advanced Ceramics Progress: Vol. 9, No. 3, (Summer 2023) 43-49

Materials and Energy Research Center
MERC

Contents lists available at ACERP

Advanced Ceramics Progress

Journal Homepage: www.acerp.ir

Original Research Article

A Transparent and Simple Synthesis of Superhydrophobic Coating Based on ZnO Microsheet/Epoxy Resin

Faezeh Afshari [a], Zohreh GolshanBafghi [a], Ramin Mir Mohammadi [b], Negin Manavizadeh [c] *

[a] *Graduate Master Student, Nanostructured Electronic Devices Laboratory, Faculty of Electrical Engineering, K. N. Toosi University of Technology, Tehran, Iran.*
[b] *Graduate Student, Faculty of Civil and Environmental Engineering, Amirkabir University of Technology, Tehran, Iran.*
[c] *Associate Professor, Nanostructured Electronic Devices Laboratory, Faculty of Electrical Engineering, K. N. Toosi University of Technology, Tehran, Iran.*

* Corresponding Author Email: manavizadeh@kntu.ac.ir (Negin Manavizadeh) URL: https://www.acerp.ir/article_206108.html

ARTICLE INFO

Article History:

Received: 07 October 2023
Revised: 15 December 2023
Accepted: 07 September 2024

Keywords:

Atmospheric Soiling,
Leakage Current Test,
Porcelain Insulator,
Self-Cleaning,
Zinc Oxide,
Nanostructures,
Oleic Acid

ABSTRACT

Environmental conditions and pollution significantly impact the performance of the power system. In dusty and foggy environments, the risks of degradation, leakage current, and pollution flashovers increase. Based on environmental and practical concerns, self-cleaning coatings present a promising solution to prevent power system failure. The current research uses a spray-coating method to apply a robust ZnO nanosheet/Epoxy resin superhydrophobic film onto a porcelain insulator. Hydrophilic ZnO nanosheet is successfully synthesized and modified with oleic acid using a simple wet chemical method. The water contact angle for ZnO/resin coating insulators was obtained at 153º. The obtained results demonstrate that wettability remains unchanged under ultraviolet illumination. A sandpaper abrasion test was then employed to determine the high strength of double-layer ZnO/resin coatings. While coating the glass, the water contact angle was obtained as 151º on the double-layer coated glass. The results further show that compared to the uncoated glass, the coated glass slide transmits 51% visible light. A robust ZnO/resin superhydrophobic coating with high mechanical stability and constant wettability can be effectively used for power line components. ZnO/resin coating can be applied to insulators in soiling sites, preventing contamination fouling. The results also indiacte that the leakage current of the insulator decreases by approximately 42% when using superhydrophobic ZnO/resin coating.

https://doi.org/10.30501/acp.2024.419694.1133

1. INTRODUCTION

Environmental conditions have significant practical effects on the safety and stability of power system operation [1,2]. The rapid growth of industrial sites and chemical parks has contributed to an increase in dusty weather [3]. The accumulation of impurities on insulators and wires raises the risk of degradation, pollution flashover, and leakage currents [4,5]. Additionally, foggy environments and humid weather lead to the a combination of the water layers and contaminants, thus increasing the current leakage [6,7]. Photovoltaic system efficiency is also significantly reduced by the accumulation of pollution layers on solar panels [8–10]. Dry weather and dust storms promote the deposition of particulates on the power system components [11].

Please cite this article as: Afshari, F., GolshanBafghi, Z., Mir Mohammadi, R., Manavizadeh, N. "A Transparent and Simple Synthesis of Superhydrophobic Coating Based on ZnO Microsheet/Epoxy Resin", ***Advanced Ceramics Progress***, Vol. 9, No. 3, (2023), 43-49. https://doi.org/10.30501/acp.2024.419694.1133

Various methods have been employed to mitigate the pollution problems in power lines. Water jet cleaning is a standard method for transmission line cleansing [12]. In deserts and other impassable areas, external insulator washing and photovoltaic panel cleansing are expensive and require significant water and labor sources [13]. Aerodynamic insulators can be used in specific areas such as dry regions, where wind assists in cleaning the insulators [14]. Another method is using insulators with silicone or grease coatings. However, these coatings lose their dielectric and viscosity properties and require regular change, depending on the environmental conditions [15]. Room Temperature Vulcanized (RTV) coating offer effective anti-pollution properties but it shows poor performance and low mechanical stability after a while [16]. Other methods involves coatings with specific wettability properties, such as self-cleaning coatings that prevent particle accumulation [17]. The self-cleaning coatings, based on different materials such as aluminum nitride, titanium dioxide, zinc oxide, and hafnium oxide, imprve the electrical stability of insulators [18–20].

Zinc oxide (ZnO) is a non-toxic semiconductor with a wide bandgap (Eg=3.37 eV) and thermal stability [21–23]. ZnO can be synthesized into several dimensional nanostructures that exhibit photocatalytic activity and different wettability behaviors, namely hydrophobicity and hydrophilicity [24,25]. Hydrophobic surfaces have a Water Contact Angle (WCA) greater than 90°, while superhydrophobic surfaces have a WCA above 150°. In contrast, hydrophilic coatings have a WCA of less than 90 [26]. While hydrophobic surfaces are cleaned by rolling water droplets on the surface, hydrophilic surfaces are covered by water sheets that clean the surface. Self-cleaning coatings with hydrophobic properties prevent surfaces from becoming wet. Superhydrophobic coatings help avoid the formation of contaminant layers and water films on insulator surfaces. Oleic acid, a low-surface-energy material, is available in various animal and vegetable fats and oils [27]. Modifying ZnO nanoparticles with oleic acid produces superhydrophobic coatings [28]. The simple and low-cost hydrothermal method is used to modify nanoparticles with oleic acid [29].

ZnO self-cleaning coatings can be fabricated through different methods, such as wet-chemical deposition, sol-gel process, hydrothermal spray coating, and Chemical Bath Deposition (CBD) [25,30–34]. Among these methods, spray coating deposition is a simple and cost-effective method for self-cleaning coatings. One challenge faced by older power sites is the replacement of uncoated insulator. To be specific, replacing coated insulators at such sites can be costly, making the spray coating method particularly effective for depositing ZnO/resin self-cleaning coatings onto existing insulators.

Of note, self-cleaning coatings must be highly durable in contaminated and windy environments. ZnO/resin self-cleaning coatings offer a simple and least complex solition for surface coatings. Epoxy resin provides high mechanical stability and good adhesion to treated ZnO nanoparticles (np) [35]. ZnO superhydrophobic np/resin coating has been considered for application on insulators in transmission lines located in extremely dry areas.

In this study, the spray-coating method is used to deposit a superhydrophobic ZnO/epoxy resin self-cleaning coating on a porcelain insulator. The ZnO coating is characterized using a Scanning Electron Microscope (FESEM) to analyze the surface morphology. The wettability of ZnO/resin self-cleaning coating is evaluated by measuring the WCA. The spectra of the ZnO/resin coating Energy are analyzed using an Dispersive X-Ray Analyzer (EDX). Leakage current tests are conducted on the insulator with self-cleaning coating, and the influence of the ZnO/resin coating on the electrical properties of the insulator is analyzed. A visible light transmission test is done to study the transparency of the layer on the glass surface. Finally, a sandpaper abrasion test assesses the mechanical stability and adherence of the coating.

All chemicals used in the experiment were of analytical grade. Zinc nitrate hexahydrate ($Zn(NO_3)_2.6H_2O$) (Aldrich, USA), Sodium hydroxide (NaOH) (Merck, Germany), Oleic acid ($C_{18}H_{34}O_2$) (Merck, Germany), Resin epoxy (Gando, Iran), and Ethanol (C_2H_5OH) (Merck, Germany) were used as reagents. A 0.99 M zinc nitrate hexahydrate solution in deionized (DI) water was prepared to synthesize hydrophilic ZnO nanosheets. In a separate beaker, 2 M sodium hydroxide was dissolved in deionized water. The zinc nitrate solution was then steadily added to the NaOH solution dropwise at a low stirring speed. Subsequently, the blended solution was vigorously stirred at room temperature for 2 hours. The mixed solution was then centrifuged for 10 minutes, and the white precipitates were collected using filter paper. The residue was rinsed with ethanol and DI water three times. Finally, the collected ZnO microstructures were dried in a vacuum at 140-150℃. Fig. 1(a,b) represents the schematic of the ZnO nanosheet production.

To prepare superhydrophobic ZnO nanosheets, 0.14 M ZnO hydrophilic nanosheet and 40 mg oleic acid were dissolved in 6 ml ethanol, as shown in Fig. 1(c). The final solution was stirred at 80 ℃ for 90 minutes. For the first layer, the resin and hardener (in a 3:1 ratio) were dissolved in 10 ml of absolute pure ethanol for the first layer. Subsequently, the epoxy resin mixture was stirred at room temperature for 30 minutes to ensure a precise and uniform solution.

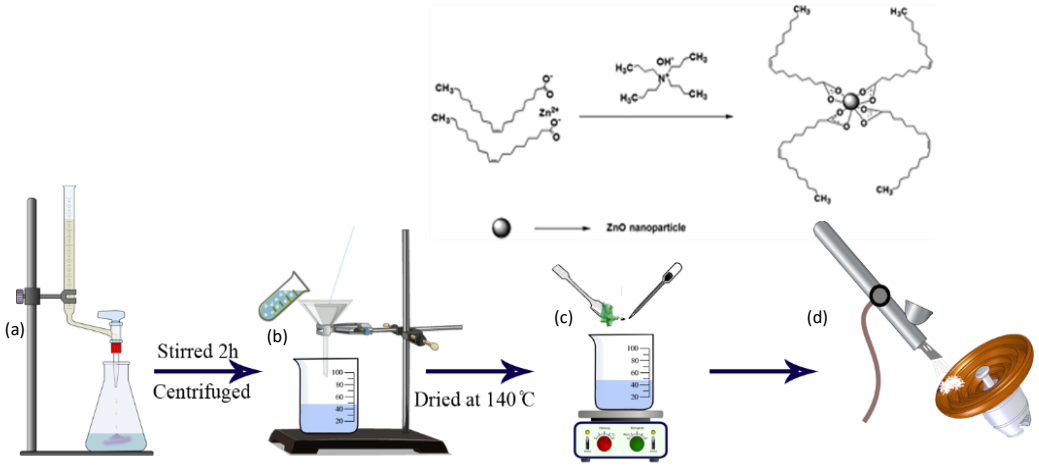

Figure 1: Schematic of superhydrophobic ZnO/resin coating process on insulator surface.

Porcelain insulators and glass slides were chosen as substrates. As a preliminary step, the substrates were cleaned with acetone, ethanol, and DI water. To apply a double-layer coating, the resin and ethanol solution were first sprayed onto the substrates by a spray gun. The airbrush was held at an optimal distance from the substrates to ensure complete surface coverage. The thickness of the coating layer is controlled by adjusting the pressure of the airbrush. For approximately 20 minutes, while the resin was not fully cured, ZnO superhydrophobic nanosheets in ethanol solution were sprayed onto the substrates. The coated surfaces were then allowed to dry at room temperature for 24 hours. The schematic of the superhydrophobic ZnO/resin synthesis process is illustrated in Fig. 1. As shown in Fig. 1(d), when oleic acid combines with zinc oxide, the long chains surround ZnO nanosheets.

The morphological and structural characteristics of the ZnO superhydrophobic coating were investigated using Field Emission Scanning Electron Microscopy (FESEM) images obtained by Hitachi S-4160 (20 kV, Japan). The chemical compositions of the coated surfaces were analyzed by Energy-Dispersive X-ray Spectroscopy (EDS). A UV/visible spectrometer (Perkin-Elmer, Lambda EZ201, USA) was also utilized to study the detector's response to different wavelengths. In addition, electrical properties were examined through leakage current tests. Here, the leakage current was measured on the grounding conductor connected to the insulator. The voltage applied to the conductor varied between 0 kV and approximately 20 kV, and the current was measured using an auto-ranging digital multimeter with true RMS capabilities. The mechanical stability of the self-cleaning coating was measured using a sandpaper abrasion test. A medium sandpaper with about 100-120 grit and a 100-g weight was also used for the stability test.

3. RESULTS AND DISCUSSION

Spray-coating is a simple method for providing a self-cleaning coating on various substrates. This scalable method can be used for power lines in non-laboratory environments. In addition, the spray method facilitates the deposition of multilayer coatings on substrates. In this study, double-layer ZnO nanosheets and epoxy resin coatings were applied to cover the porcelain insulator and glass slide, respectively. The morphology of superhydrophobic coatings containing ZnO nanosheets and ZnO nanosheets/epoxy resin deposited on substrates was investigated by SEM analysis. Fig. 2(a) shows that the modified ZnO nanosheets are well-formed with different lengths and widths with an average thickness of 100 nm. As shown in Fig. 2(b), the ZnO/resin film fully envelops the porcelain insulator. SEM analysis indicates that the epoxy resin layer containing ZnO nanosheets is more uniform than the superhydrophobic ZnO nanosheets.

Moreover, superhydrophobic ZnO nanosheets exhibited different textures within the epoxy resin, as presented in Fig. 2(b). A cross-section image of ZnO nanosheets/resin coating displays the trapping of superhydrophobic ZnO nanosheets in the resin layer (Fig. 2(c)). This double-layer coating allows the ZnO nanosheets to impart super hydrophobicity behavior and high stability.

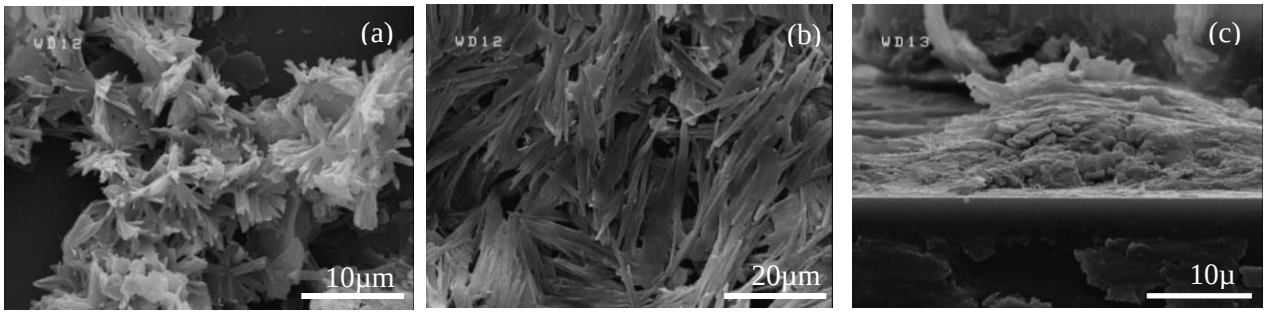

Figure 2: SEM images of (a) ZnO superhydrophobic microsheets, (b) ZnO NS/Resin superhydrophobic coating and (c) ZnO NS/Resin Coating cross section.

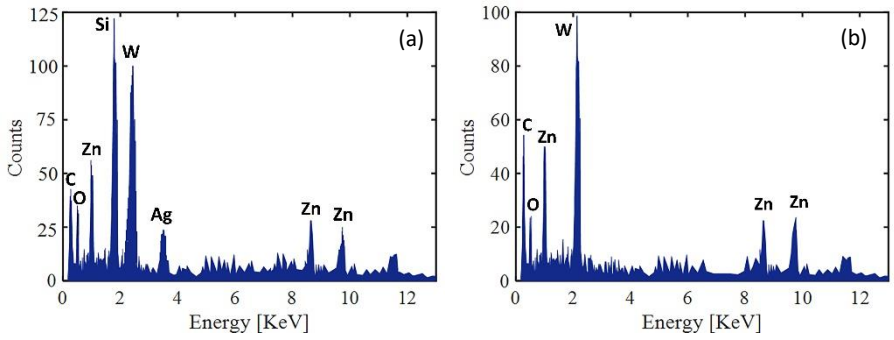

Figure 3. EDS analysis of (a) modified ZnO nanosheets and (b) ZnO/resin coating.

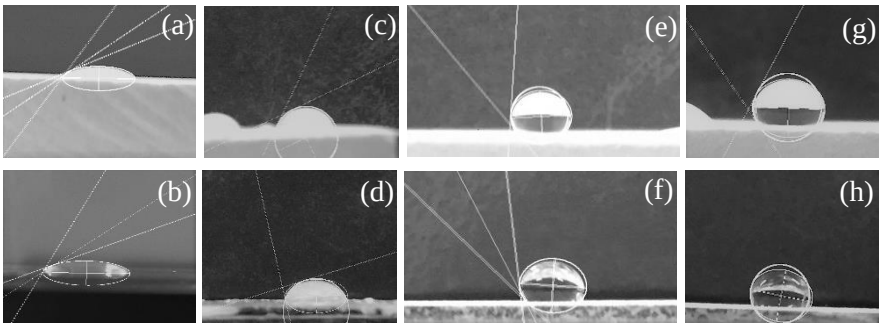

Figure 4. Water droplet on (a) porcelain insulator, (b) glass substrate, (c) resin coating on porcelain, (d) resin coating on glass substrate, (e) double-layer ZnO/resin coating on porcelain insulator, (f) double-layer ZnO/resin coating glass substrate, (g) porcelain with double-layer coating and (h) glass with double-layer coating after sandpaper abrasive test.

In the present research, EDS analysis was employed to determine the chemical composition of ZnO coating. According to the EDS results, zinc, oxygen, and carbon were observed, confirming the successful formation of modified zinc oxide nanosheets (Fig. 3). The other elements detected originated from the coating layer used for EDS analysis and the substrate. Further, the EDS analysis revealed the atomic percentage of zinc and oxygen atoms as 13.7% and 86.3%, respectively (Fig. 3(a)). In contrast, the atomic percentages of zinc and oxygen atoms in the ZnO/resin film were 18.7% and 81.3%, respectively (Fig. 3(b)). As shown in Fig. 3(b), there are two peaks in the EDS spectrum attributed to tungsten (W) and carbon (C) elements in the epoxy resin. Silicon (Si) and silver (Ag) peaks in the EDS spectrum are attributed to the substrate and EDS tests. Additionally, the similarity between the EDS spectrums indicates that the ZnO structures remained stable even after being mixed with resin epoxy.

The wettability is the most crucial figure of merit in characterizing the coatings. The WCA measurement was used to assess the wettability of double-layer ZnO/resin coating deposited on the porcelain insulator and glass substrates. According to Fig.4 (a,b), the WCA values for porcelain and glass without coating were obtained as 25±5˚ and 30±5˚, respectively, indicating that the initial substrates were hydrophilic. For comparison, the WCA of the pure resin coating was measured on porcelain and glass substrates. As shown in Fig.4, the WCAs of porcelain and glass substrate with resin coating were 60±5˚ and 50±5˚, respectively. On the contrary, the WCAs of the coated porcelain insulator and coated glass

reached 153.7±5˚ and 151.2±5˚, respectively (Fig. 4). These results show that the pure resin coating possesses hydrophilic properties while double-layer ZnO/resin coating exhibits superhydrophobic characteristics on both surfaces. As shown in Figs. 4 (g) and 4(h), the WCAs did not change on either substrate following the sandpaper abrasive test. For several times, both porcelain insulator and glass slide with superhydrophobic coating were exposed to ultraviolet (UV) light and according to the results, the WCA of the surfaces did not change with UV exposure. Additionally, there was no crack in the wettability behavior after UV exposure, a critical characteristic for some hydrophilic materials. The combination of pollution and water accelerates the aging process and increases the risk of leakage current.

Figure 5. Leakage currents test for (a) Uncoated and (b) coated insulators.

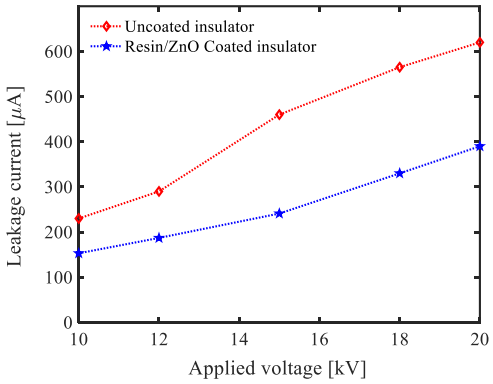

Figure 6. Leakage currents versus applied voltage for superhydrophobic ZnO/resin self-cleaning coating on insulator surface.

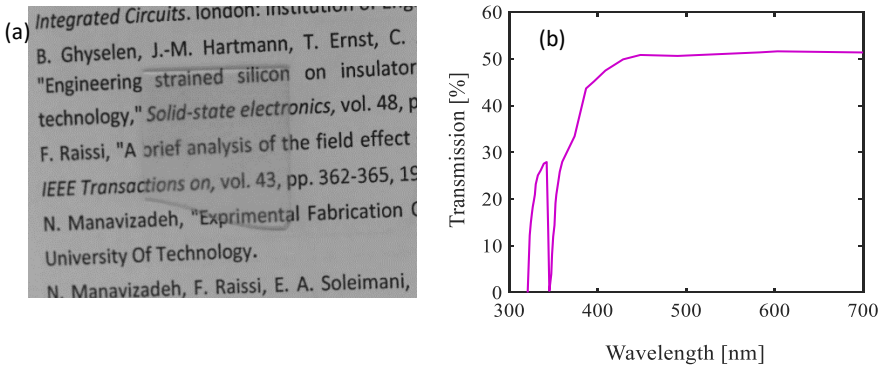

Figure 7: (a) small glass slide with ZnO/resin superhydrophobic coating and (b) transmittance of glass with ZnO/resin coating in optical spectra.

In humid conditions, leakage currents flow across the surface of contaminated insulators. Lower leakage currents reduce the need for repairs in the distribution system and minimize the energy loss. The leakage current of coated and uncoated insulators was measured in a power transition simulation. Both types of insulators were connected to the power lines, and their surfaces were sprayed with water (Fig. 5). The leakage current was then measured for both coated and uncoated insulators under wet conditions, the results of which are

plotted in Fig. 6 at different applied voltages. For the uncoated insulators, at 15 kV, the leakage current reached approximately 460 µA. By comparison, for the coated insulators at 15 kV voltage, leakage current dropped to 241 µA. Overall, the leakage currents in the coated insulators decreased by 42%, compared to uncoated ones.

The performance of solar panels is similarly affected by dusty weather conditions. The double-layer ZnO/resin superhydrophobic coating prevents dirt accumulation on the surface. Fig. 7(a) shows a glass slide with a double-layer ZnO/resin coating. Moreover, the transparency of ZnO/resin superhydrophobic coating makes it suitable for use in lighting applications. The transmission spectra show that the average transmittance of the coated substrate was 51% in the visible range of 400–700 nm (Fig. 7(b)).

Self-cleaning coatings are utilized in various places, specifically outdoors, where high mechanical stability is required. In this regard, a sandpaper abrasion test was conducted. The coating surface was subjected to a 100-g weight during the test. The sandpaper was then moved over a distance of 15 cm with a pressure of 5 kPa, and the scratching action was repeated 100 times. Afterward, the water contact angle was measured. The WCA of both the porcelain insulators and glass surfaces with ZnO/resin coating showed no significant change after 100 abrasion cycles, and the coating maintained its superhydrophobic properties.

4. CONCLUSION(S)

The robust double-layer zinc oxide superhydrophobic/resin coating was fabricated by spray-coating on a porcelain insulator and glass slide. Zinc oxide nanosheets were successfully synthesized by the one-step wet chemical method and further enhanced by oleic acid during a hydrothermal process, resulting in superhydrophobic behavior. In contaminated environments, the coating deposition on the insulator surface reduces replacement costs and offers significant technical and economic benefits. SEM analysis revealed that the double-layer modified ZnO nanosheets/resin coated the insulator densely and uniformly. The Water Contact Angles (WCAs) were approximately 153.7±5° and 151.2±5° on the porcelain insulator and glass slide with ZnO/resin coating, respectively. Double-layer ZnO/resin coating on glass and porcelain insulator surfaces represents superhydrophobic behavior. The superhydrophobic coating prevents water from flowing on the surface of the substrate. One of the most notable features of the coating is its stability in superhydrophobic behavior even after ultraviolet exposure.

According to the electrical results, the leakage current on the insulator surface decreased by about 42%. For the uncoated porcelain insulator at 15 kV, the leakage current was 460 µA while the coated porcelain showed a reduced current of about 241 µA at the same voltage. The double-layer ZnO/resin superhydrophobic coating also demonstrated high mechanical stability during the sandpaper abrasion test. Further, the transmission spectra of the coated glass showed 51% optical transmittance in the visible range of 400–700 nm—allowing potential applications in lighting such as solar panels. Self-cleaning ZnO/resin coatings are considerably suitable for reducing pollution in porcelain insulators, wires, and other components. The simple implementation method, high strength, and constant superhydrophobic behavior of double-layer ZnO/resin coating make it an effective solution for power line systems in polluted environments.

REFERENCES

1. Qiao X, Zhang Z, Jiang X, Sundararajan R, You J. DC pollution flashover performance of HVDC composite insulator under different non-uniform pollution conditions. *Electric Power Systems Research*. 2020;185:106351. https://doi.org/10.1016/j.epsr.2020.106351
2. Salem AA, Lau KY, Rahiman W, et al. Pollution Flashover Voltage of Transmission Line Insulators: Systematic Review of Experimental Works. *IEEE Access*. 2022;10:10416-10444. https://doi.org/10.1109/ACCESS.2022.3143534
3. Zhang D, Meng F. Research on the Interrelation between Temperature Distribution and Dry Band on Wet Contaminated Insulators. *Energies*. 2019;12(22):4289. https://doi.org/10.3390/en12224289
4. Orellana L, Ardila-Rey J, Avaria G, Davis S. Danger assessment of the partial discharges temporal evolution on a polluted insulator using UHF measurement and deep learning. *Engineering Applications of Artificial Intelligence*. 2023;124:106573. https://doi.org/10.1016/j.engappai.2023.106573
5. Maraaba L, Al-Soufi K, Ssennoga T, Memon A, Worku M, Alhems L. Contamination Level Monitoring Techniques for High-Voltage Insulators: A Review. *Energies*. 2022;15(20):7656. https://doi.org/10.3390/en15207656
6. Honarvar Nazari H, Dhakal TP. Influence of Ag-doping on the performance of Cu2ZnSnS4 solar cells. *Solar Energy*. 2023;253:321-331. https://doi.org/10.1016/j.solener.2023.02.001
7. Guo Y, Jiang X, Liu Y, Meng Z, Li Z. AC flashover characteristics of insulators under haze–fog environment. *IET Generation, Transmission & Distribution*. 2016;10(14):3563-3569. https://doi.org/10.1049/iet-gtd.2016.0284
8. Kazem HA, Chaichan MT, Al-Waeli AHA, Sopian K. A review of dust accumulation and cleaning methods for solar photovoltaic systems. *Journal of Cleaner Production*. 2020;276:123187. https://doi.org/10.1016/j.jclepro.2020.123187
9. Shahryari AM, Bafghi ZG, Manavizadeh N. Efficiency Enhancement of Heterojunction IBC Solar Cell: Surface Passivation. In: *2022 30th International Conference on Electrical Engineering (ICEE)*. IEEE; 2022:808-811. https://doi.org/10.1109/ICEE55646.2022.9827127
10. Fan S, Wang Y, Cao S, Sun T, Liu P. A novel method for analyzing the effect of dust accumulation on energy efficiency loss in photovoltaic (PV) system. *Energy*. 2021;234:121112. https://doi.org/10.1016/j.energy.2021.121112
11. Liu Y, Kong X, Du B, Li J, Sun J. Numerical Investigation on Collision of Pollution Particles on Outdoor Insulators. *IEEE Access*. 2019;7:56974-56985. https://doi.org/10.1109/ACCESS.2019.2914075
12. Alghamdi, Bahaj, Blunden, Wu. Dust Removal from Solar PV Modules by Automated Cleaning Systems. *Energies*. 2019;12(15):2923. https://doi.org/10.3390/en12152923
13. Goto S, Nakamura M, Nannyakkara N, Taniguchi T. Accurate decision-making for timely washing of substation insulators, based on a pollution model. *Control Engineering Practice*. 1997;5(12):1683-1689. https://doi.org/10.1016/S0967-0661(97)10022-3

14. Liu Y, Wu G, Guo Y, et al. Pollution agglomeration characteristics on insulator and its effect mechanism in DC electric field. *International Journal of Electrical Power & Energy Systems*. 2020;115:105447. https://doi.org/10.1016/j.ijepes.2019.105447
15. Dai W, Liu P, Chen X, et al. Application of Self-Cleaning Ceramic and Glass Insulators for Electricity Transmission. In: Zhang X, Tryk D, Irie H, Fujishima A, eds. *Handbook of Self-Cleaning Surfaces and Materials*. 1st ed. Wiley; 2023:545-561. https://doi.org/10.1002/9783527690688.ch23
16. Ramirez I, Cherney EA, Jarayam S. Comparison of the erosion resistance of silicone rubber and EPDM composites filled with micro silica and ATH. *IEEE Trans Dielect Electr Insul*. 2012;19(1):218-224. https://doi.org/10.1109/TDEI.2012.6148521
17. Mi X, Liang N, Xu H, et al. Toughness and its mechanisms in epoxy resins. *Progress in Materials Science*. 2022;130:100977. https://doi.org/10.1016/j.pmatsci.2022.100977
18. Barandehfard F, Aluha J, Ntho TA, Gitzhofer F. Synthesizing AlN Coatings Using Suspension Plasma Spraying: Effect of Promotional Additives and Aluminum Powder Particle Size. *J Therm Spray Tech*. 2022;31(7):2091-2111. https://doi.org/10.1007/s11666-022-01414-z
19. Yu J, Liu Y, Huang B, et al. Rapid hydrophobicity recovery of contaminated silicone rubber using low-power microwave plasma in ambient air. *Chemical Engineering Journal*. 2023; 465:142921. https://doi.org/10.1016/j.cej.2023.142921
20. Castaño JG, Velilla E, Correa L, Gómez M, Echeverría F. Ceramic insulators coated with titanium dioxide films: Properties and self-cleaning performance. *Electric Power Systems Research*. 2014;116:182-186. https://doi.org/10.1016/j.epsr.2014.06.009
21. Rezaie S, Bafghi ZG, Manavizadeh N. Carbon-doped ZnO nanotube-based highly effective hydrogen gas sensor: A first-principles study. *International Journal of Hydrogen Energy*. 2020;45(27):14174-14182. https://doi.org/10.1016/j.ijhydene.2020.03.050
22. Golshan Bafghi Z, Manavizadeh N. Low power ZnO nanorod-based ultraviolet photodetector: Effect of alcoholic growth precursor. *Optics & Laser Technology*. 2020;129:106310. https://doi.org/10.1016/j.optlastec.2020.106310
23. Rezaie S, Bafghi ZG, Manavizadeh N, Kordmahale SB. Highly Sensitive Detection of Dissolved Gases in Transformer Oil With Carbon-Doped ZnO Nanotube: A DFT Study. *IEEE Sensors Journal*. 2022;22(1):82-89. https://doi.org/10.1109/JSEN.2021.3126654
24. Afshari F, Bafghi ZG, Manavizadeh N, Nadimi E. H2O Absorption on Mono and Multilayer Zinc Oxide Nanoribbon: A First Principles Study. In: *2019 27th Iranian Conference on Electrical Engineering (ICEE)*. ; 2019:92-96. https://doi.org/10.1109/IranianCEE.2019.8786684
25. Afshari F, Golshan Bafghi Z, Manavizadeh N. Unsophisticated one-step synthesis super hydrophilic self-cleaning coating based on ZnO nanosheets. *Appl Phys A*. 2021;128(1):75. https://doi.org/10.1007/s00339-021-05222-0
26. Li J, Han X, Li W, Yang L, Li X, Wang L. Nature-inspired reentrant surfaces. *Progress in Materials Science*. 2023;133:101064. https://doi.org/10.1016/j.pmatsci.2022.101064
27. Paraskar PM, Prabhudesai MS, Hatkar VM, Kulkarni RD. Vegetable oil based polyurethane coatings – A sustainable approach: A review. *Progress in Organic Coatings*. 2021;156:106267. https://doi.org/10.1016/j.porgcoat.2021.106267
28. Cirisano F, Ferrari M. Sustainable Materials for Liquid Repellent Coatings. *Coatings*. 2021;11(12):1508. https://doi.org/10.3390/coatings11121508
29. Hu H, Liang H, Fan J, et al. Assembling Hollow Cactus-Like ZnO Nanorods with Dipole-Modified Graphene Nanosheets for Practical Room-Temperature Formaldehyde Sensing. *ACS Appl Mater Interfaces*. 2022;14(11):13186-13195. https://doi.org/10.1021/acsami.1c20680
30. Wang X, Ahmad M, Sun H. Three-Dimensional ZnO Hierarchical Nanostructures: Solution Phase Synthesis and Applications. *Materials*. 2017;10(11):1304. https://doi.org/10.3390/ma10111304
31. Amudhavalli B, Mariappan R, Prasath M. Synthesis chemical methods for deposition of ZnO, CdO and CdZnO thin films to facilitate further research. *Journal of Alloys and Compounds*. 2022;925:166511. https://doi.org/10.1016/j.jallcom.2022.166511
32. Yang M, Liu W, Jiang C, et al. Facile construction of robust superhydrophobic cotton textiles for effective UV protection, self-cleaning and oil-water separation. *Colloids and Surfaces A: Physicochemical and Engineering Aspects*. 2019;570:172-181. https://doi.org/10.1016/j.colsurfa.2019.03.024
33. Baldelli A, Ou J, Li W, Amirfazli A. Spray-On Nanocomposite Coatings: Wettability and Conductivity. *Langmuir*. 2020;36(39):11393-11410. https://doi.org/10.1021/acs.langmuir.0c01020
34. Rezaie MN, Manavizadeh N, Nayeri FD, Bidgoli MM, Nadimi E, Boroumand FA. Effect of seed layers on low-temperature, chemical bath deposited ZnO nanorods-based near UV-OLED performance. *Ceramics International*. 2018;44(5):4937-4945. https://doi.org/10.1016/j.ceramint.2017.12.086
35. Sari MG, Saeb MR, Shabanian M, et al. Epoxy/starch-modified nano-zinc oxide transparent nanocomposite coatings: A showcase of superior curing behavior. *Progress in Organic Coatings*. 2018;115:143-150. https://doi.org/10.1016/j.porgcoat.2017.11.016

Advanced Ceramics Progress: Vol. 9, No. 3, (Summer 2023) 50-56

Materials and Energy Research Center
MERC

Contents lists available at ACERP

Advanced Ceramics Progress

Journal Homepage: www.acerp.ir

Original Research Article

Enhancing the Electrical Properties of Bismuth Titanate Ceramics Using Zinc Oxide Nanoparticles as Sintering Aid

Fatemeh Alidoosti Shahraki [a], Hajar Ahmadimoghadam [b] *

[a] *MSc, Department of Materials Engineering, Faculty of Engineering, University of Shahrekord, Shahrekord, Iran.*
[b] *Associate Professor, Department of Materials Engineering, Faculty of Engineering, University of Shahrekord, Shahrekord, Iran.*

* Corresponding Author Email: hajar.ahmadi@sku.ac.ir (H. Ahmadimoghadam)

URL: https://www.acerp.ir/article_205719.html

ARTICLE INFO

Article History:

Received: 10 May 2024
Revised: 31 May 2024
Accepted: 7 September 2024

Keywords:

Bismuth Titanate,
Zinc Oxide Nanoparticles,
Sintering,
Dielectric Properties,
Microstructure

ABSTRACT

In this study, bismuth titanate (BIT) powder was synthesized through solid-state synthesis method. Then, the effect of zinc oxide (ZnO) nanoparticles as a sintering aid on the electrical properties of BIT ceramic was investigated. The weight percentages of ZnO used in this study were 0.3, 0.6, and 1.2. Disc-shaped samples were prepared using the uniaxial pressing method and sintered at the temperatures of 1025, 1075, and 1125 °C for 1, 2, and 5 h at the heating rates of 3, 5, and 10 °C/min. The highest density values were achieved under the optimal sintering conditions of 1075 °C, 2 h, and a heating rate of 5 °C/min. Addition of ZnO nanoparticles improved the densification of the BIT ceramics. In the sample containing 1.2 wt.% of ZnO, a secondary phase of Zn_2TiO_4 was identified. Incorporation of ZnO nanoparticles resulted in an increase in the dielectric constant, a reduction in dielectric loss, and improvement in the piezoelectric and ferroelectric properties of the BIT ceramics. These enhancements contributed to increased density and reduced electrical conductivity. The best results were obtained with the sample containing 0.6 wt.% of nano ZnO characterized by a high dielectric constant (312), low dielectric loss ($\tan\delta$ = 0.01), high piezoelectric coefficient (d_{33} = 21 pC/N), and high remnant polarization (4.25 μC/cm^2).

https://doi.org/10.30501/acp.2024.456603.1152

1. INTRODUCTION

Layered ferroelectric bismuth-containing structures (BLSFs) have received significant attention over the past two decades owing to their outstanding electrical properties as lead-free piezoelectric materials at high temperatures. They also allow for customized properties by adjusting the chemical composition and number of layers. BLSF ceramics, with their high Curie temperature (T_C), fatigue resistance, and thermal stability, can be used at temperatures above 400 °C. The general formula for BLSFs is $(Bi_2O_2)^{2+}(A_{n-1}B_nO_{3n+3})^{2-}$, which consists of perovskite-like layers $(A_{n-1}B_nO_{3n+3})^{2-}$ separated by $(Bi_2O_2)^{2+}$ layers along the crystallographic c-axis. In this formula, n ($1 \leq n \leq 5$) denotes the number of perovskite layers. BLSF crystal structures have a large c/a ratio based on the value of n ($c/a \approx 1.5(n+1)$), thus resulting in the formation of plate-like grains with a high aspect ratio and significant anisotropy in their electrical properties [1-3]. It has been reported that achieving highly oriented and textured grains through techniques such as applying pressure during the solid-state sintering process and directionally controlled grain growth would lead to improved electrical properties [1,4].

Among the BLSF family, bismuth titanate ($Bi_4Ti_3O_{12}$, n=3, BIT) has received significant attention due to its high curie temperature (approximately 670 °C), strong inherent polarization, and notable fatigue resistance. BIT ceramics, as a suitable choice for high-temperature

Please cite this article as: Alidoosti Shahraki, F. & Ahmadimoghadam, H. (2023). "Enhancing the Electrical Properties of Bismuth Titanate Ceramics Using Zinc Oxide Nanoparticles as Sintering Aid" ***Advanced Ceramics Progress***, Vol. 9, No. 3, (2023), 50-56. https://doi.org/10.30501/acp.2024.456603.1152

piezoelectric applications, demonstrate excellent performance in non-volatile random-access memories (NvRAMs) [2]. However, BIT ceramics have some drawbacks including their relatively low piezoelectric coefficient (d_{33} less than 10 pC/N) due to the challenge of achieving easy polarization caused by its high leakage current. Additionally, the high dielectric loss (tan δ) and low electrical resistivity at elevated temperatures, attributed to oxygen vacancies resulting from bismuth volatilization during the sintering process, can limit the potential applications of BIT ceramics [1,5].

In recent years, several technologies have been introduced to overcome the limitations of BIT ceramics, thereby improving their properties. Some of these solutions include hot pressing, spark plasma sintering, directional grain growth, and use of dopants and additives [4, 6-8]. Among these methods, application of dopants and additives is more accessible and practical since it can significantly modify the sintering process, microstructure, and electrical properties of BIT ceramics [9,10]. Studies have shown that substituting cations in the B position greatly enhanced the piezoelectric properties of BLSFs [2,5,11]. Moreover, substituting V^{5+} cations for Ti^{4+} through the reduction of oxygen and bismuth vacancies led to reduced current leakage, easier domain movement, and increased polarization, thereby improving the ferroelectric and dielectric properties of BIT ceramics [12]. The introduction of Fe^{3+} ions into the Ti^{4+} position of the BIT structure has proved to enhance its ferroelectric properties and ferromagnetism [13]. Similarly, simultaneous use of Nb^{5+} and Fe^{3+} cations in the B position of the BIT structure results in a decrease in the dielectric constant and induction of ferromagnetism [2]. Additionally, W/Cr co-doped $Bi_4Ti_3O_{12}$ ceramics exhibited an improvement in their piezoelectric coefficient and an increase in their electrical resistance due to the lattice distortion [14]. It was reported that addition of zinc oxide to bismuth potassium titanate ($(Bi_{0.5}K_{0.5})TiO_3$) ceramic resulted in grain growth and increased density. When added in amounts less than 2 wt%, it improved the dielectric constant and piezoelectric coefficient. These improvements were attributed to the formation of oxygen vacancies and distortion of the crystal lattice [15]. The simultaneous use of W/Zn dopants has resulted in an increase in the electrical conductivity and a decrease in the dielectric constant of bismuth titanate ceramic [16]. Research has demonstrated that the incorporation of zinc oxide has the potential to enhance the piezoelectric and dielectric properties of various ceramics, including sodium potassium niobates and barium titanates [17,18].

Although a great deal of research has been conducted on the effect of different cations as dopants on the electrical properties of BIT ceramics, there is limited research on additives as sintering aids. In this respect, the main objective of this study was to investigate the effect of zinc oxide nanoparticles (ZnO) as a sintering aid on the properties of BIT ceramics. BIT powder was synthesized using the solid-state method, and varying amounts (0.3, 0.6, and 1.2 wt.%) of ZnO nanoparticles were added. The current study also examined the impact of nano ZnO additive on the microstructure and dielectric properties of BIT ceramics.

2. MATERIALS AND METHODS

Bismuth oxide (Bi_2O_3) and titanium oxide (TiO_2) with the purity of 99.9% were used for the synthesis of bismuth titanate powder (BIT) with the chemical formula of $Bi_4Ti_3O_{12}$. The raw materials were accurately weighed according to the BIT stoichiometry and then mixed in a planetary mill with zirconia balls in ethanol at a speed of 250 rpm for 5 hours. Subsequently, the resulting powder was calcined at 850 ºC for 3 hours. Zinc oxide nanoparticles (99.9%, ≤70 nm, Advanced Materials US) were added to the synthesized BIT powder in weight percentages of 0.3, 0.6, and 1.2. A planetary mill operating at 300 rpm for 5 hours ensured a uniform mixture of BIT powder and nano zinc oxide. Disc-shaped samples were fabricated using the uniaxial pressing method at the pressure of 200 MPa with the diameter of 1 cm and thickness of approximately 2 mm. The samples were labeled as follows: BIT (sample without additive), BIT-0.3 Zn (sample with 0.3 wt.% nano ZnO), BIT-0.6 Zn (sample with 0.6 wt.% nano ZnO), and BIT-1.2 Zn (sample with 1.2 wt.% nano ZnO). In order to determine the optimal sintering conditions, the samples were heated at the temperatures of 1025, 1075, and 1125 ºC for 1, 2, and 5 hours at the heating rates of 3, 5, and 10 ºC/min.

The density of the samples was determined using the Archimedes immersion method following the ASTM C20-87 standard. In this experiment, X-Ray Diffraction (XRD) (Asenware model AW-XDM 300, Cu-kα radiation with a wavelength of 1.5418 Å) and Scanning Electron Microscopy (FE-SEM, model 450 FEG, FEI QUANTA) were employed to examine the phase and microstructure of the samples, respectively. Dielectric properties, including dielectric constant and dielectric loss (tanδ), were measured using an LCR-meter model OCT1010 at room temperature within the frequency range of 100 Hz to 100 kHz. The sample surfaces were initially coated with silver paste using a brush and then heated at 400 ºC for ten minutes. A piezometer (Berlincourt quasistaticmeter model) was used to measure the piezoelectric coefficient at room temperature and frequency of 100 Hz. The polarization versus electric field (P–E) ferroelectric hysteresis loops were recorded at a frequency of 50 Hz at room temperature using a Sawyer–Tower circuit.

3. RESULTS AND DISCUSSION

Variations in the density of the samples, expressed as the weight percentage of nano ZnO, at different sintering temperatures are shown in Figure 1. The sintering time was 2 hours, and the heating rate was 5 ºC/min. As shown

in Figure 1, use of nano ZnO additive has notably improved the density of BIT ceramics. The density of BIT ceramic increases as the amount of nano ZnO increases. Previous studies have stated that ZnO in bismuth titanate-based ceramics enhances densification by creating a liquid phase during the sintering process. This liquid phase, which contains a high concentration of bismuth oxide, forms in a small amount during sintering through the reaction between bismuth oxide and ZnO at the eutectic temperature of approximately 750 ºC [16,19]. According to Equation 1, replacement of Zn^{2+} ions results in the creation of oxygen vacancies ($V_O^{\bullet\bullet}$), which facilitates atomic diffusion during sintering and improves densification [20]. The BIT-0.6 Zn and BIT-1.2 Zn samples share quite similar density values. The highest density values were achieved when the samples were sintered at the temperature of 1075 ºC. Therefore, the optimal sintering temperature can be considered as 1075 ºC. The densification of ceramics during sintering occurs through the mechanism of atomic diffusion, and temperature is the main parameter that affects the diffusion of atoms [20]. Therefore, the low densities of the samples sintered at 1025 ºC may be attributed to the insufficient atoms diffusion. According to the results, the density of the samples sintered at the temperature of 1125 ºC is lower than that of samples sintered at 1075 ºC, which can be attributed to the increased volatility of bismuth oxide at higher temperatures [21]. Based on Figure 1, the density of BIT ceramics is highly dependent on the sintering temperature. At temperatures lower than the optimum temperature, density significantly decrease due to insufficient diffusion while at temperatures higher than the optimum temperature, it happens due to the increased volatility of bismuth oxide.

$$ZnO \xrightarrow{TiO_2} Zn''_{Ti} + V_O^{\bullet\bullet} + O_O \quad (1)$$

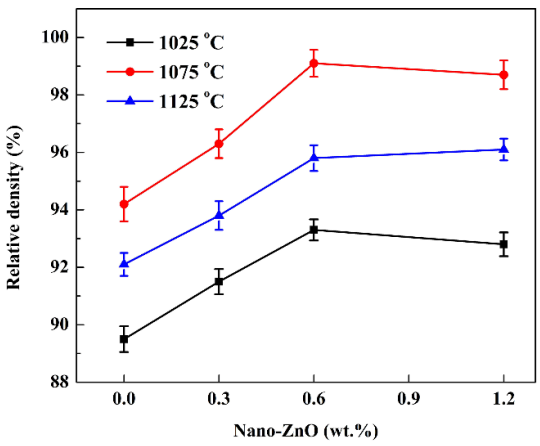

Figure 1. Variations in density of samples as a function of ZnO amount at different sintering temperatures.

Figure 2 illustrates the changes in the sample density, represented as weight percentage of nano ZnO, at different storage times during sintering. The samples were sintered at an optimal temperature of 1075 ºC for various durations at the heating rate of 5 ºC/min. According to the obtained results, the duration of maintaining the samples at the sintering temperature has a significant effect on the density of BIT ceramics. The optimal duration is determined to be 2 hours, as increasing the sintering time from 1 to 2 hours leads to an increase in sample density. However, if the duration is extended to 5 hours, a significant decrease would be observed in the sample density, even lower than the samples sintered for only 1 hour. This decrease in the density during the extended sintering times can be attributed to the increased volatility of bismuth oxide.

The density variations of the samples at different heating rates, in terms of the amount of nano ZnO, are shown in Figure 3. These samples were sintered at different heating rates at the optimal temperature of 1075 ºC for 2 hours. According to the results, the heating rate significantly affects the density of the BIT ceramic. The optimal heating rate, as indicated in Figure 3, is 5 ºC/min, hence the highest density for the samples. The samples sintered at a lower heating rate of 3 ºC/min had a lower density. At lower heating rates, coarsening and excessive grain growth dominate during sintering. In this case, not only the porosity remains in the body but also its size increases, hence a decrease in density [20]. The reduction in density at high heating rates (10 ºC/min) can be attributed to the internal stresses caused by the significant difference in the growth rates perpendicular and parallel to the plane of the layered BLSF structures. This substantial difference in the growth rates at high heating rates can generate internal stresses and microcracks, ultimately resulting in density reduction [21].

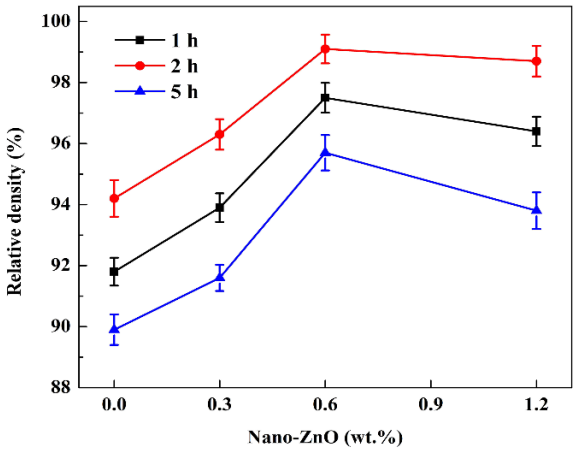

Figure 2. Variations in density of samples as a function of ZnO amount with different sintering times.

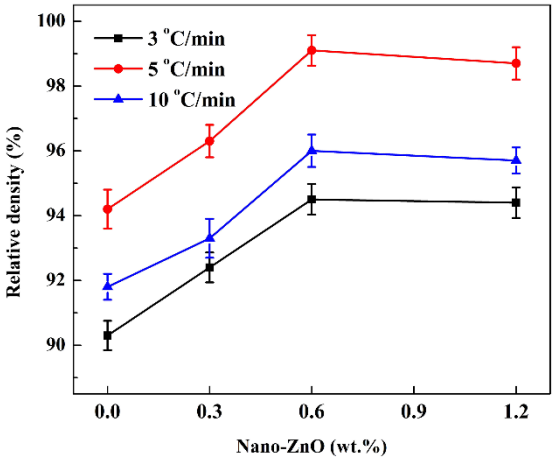

Figure 3. Variations in sample density as a function of the amount of ZnO with different heating rates

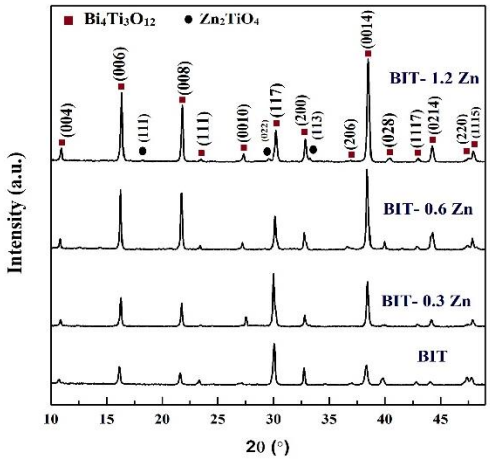

Figure 4. XRD patterns of sintered samples

Figure 4 shows the XRD patterns of the samples sintered under optimized conditions with different weight percentages of ZnO. The identified diffraction peaks in the patterns correspond to the $Bi_4Ti_3O_{12}$ phase with an orthorhombic structure (JCPDS No. 96-591-0229). No secondary phases or impurities are observed in the BIT-0.3 Zn and BIT-0.6 Zn samples. A comparison of the ionic radii of Zn^{2+} (0.74 Å), Ti^{4+} (0.605 Å), and Bi^{3+} (1.03 Å) shows that the possibility of substituting Zn^{2+} ions in the B-site of the perovskite layer of BIT instead of Ti^{4+} ions is higher than other ones. Zn^{2+} ions are smaller than Bi^{3+} ions for occupying the A-site [16, 19]. Therefore, there is a possibility of Zn^{2+} ions entering the crystal lattice of BIT and forming a solid solution. In the BIT-1.2 Zn sample, in addition to the peaks corresponding to the $Bi_4Ti_3O_{12}$ phase, three other peaks with low intensity are detected. These peaks correspond to the Zn_2TiO_4 phase with a cubic structure (JCPDS No. 96-900-1693). This phase has been reported in zinc-doped bismuth titanate compounds [15,16,19]. Of note, the solubility limit of Zn in the base BIT ceramics is less than 1 wt% [15,16]. The XRD patterns indicate that addition of ZnO has a significant effect on the peak intensities, hence a decrease in the intensity of the (117) peak and an increase in the intensities of the (006), (008), and (0014) peaks as the amount of added ZnO increases. This can indicate changes in the microstructure and grain orientation of the BIT ceramic in the presence of ZnO additives [16].

The SEM images of the fractured surfaces of both BIT and BIT-0.6 Zn samples are illustrated in Figure 5. Clearly, addition of ZnO has a significant effect on the microstructure of the BIT ceramic. The BIT-0.6 Zn sample is characterized by a dense microstructure, and the BIT sample by porosities. The grain morphology is characterized by plate-like and layered structures, with a noticeable difference in grain orientation between the BIT-0.6 Zn and BIT samples. Previous studies have demonstrated that additives in the BIT ceramics can induce preferential grain growth and grain orientation [1,4,9].

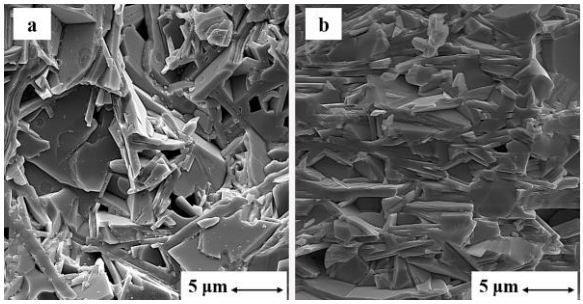

Figure 5. SEM images of fracture surfaces of samples: (a) BIT and (b) BIT -0.6 Zn

Figure 6 illustrates the variations in the dielectric constant of the samples, which were measured at room temperature in the frequency range of 100 Hz to 100 kHz. The results indicate that addition of nano ZnO increases the dielectric constant of the BIT ceramic. The highest dielectric constant values were obtained in the BIT-0.6 Zn sample. Additionally, the dependence of the dielectric constant on the frequency in the samples with ZnO additive is lower than that in the pure BIT sample. The improvement in the dielectric constant in the presence of nano ZnO additive can be attributed to higher density and lower porosity in these samples [22]. Several studies have also indicated that changes in the grain growth direction can enhance the dielectric properties [16]. Given the difference in the ionic radii between Zn^{2+} (0.74 Å) and Ti^{4+} ions (0.605 Å), substitution of Zn^{2+} ions at the B site can cause lattice distortion and local deformation of the unit cell. Preethi et. al. reported that lattice distortion resulting from the substitution of solute atoms with different radii in the structure increased the dielectric constant [23]. In addition, the decrease in the dielectric constant values of the BIT-1.2 Zn sample could

be attributed to the presence of the secondary phase Zn_2TiO_4 in this sample. They also remarked that the Zn_2TiO_4 phase had a very low dielectric constant [19].

Figure 7 shows the variations in the dielectric loss of the sample, measured at room temperature in the frequency range of 100 Hz to 100 kHz. The results indicate that incorporation of ZnO reduces the dielectric loss of the BIT ceramic. The BIT-0.6 sample had the lowest dielectric loss values and followed by addition of ZnO, the dielectric loss values in the BIT -1.2 Zn sample increased, compared to the other two samples. However, the dielectric loss values in the BIT -1.2 Zn sample remained lower than those of the pure BIT ceramic. The increase in the dielectric loss of the BIT-1.2 Zn sample can be attributed to the presence of the Zn_2TiO_4 impurity phase.

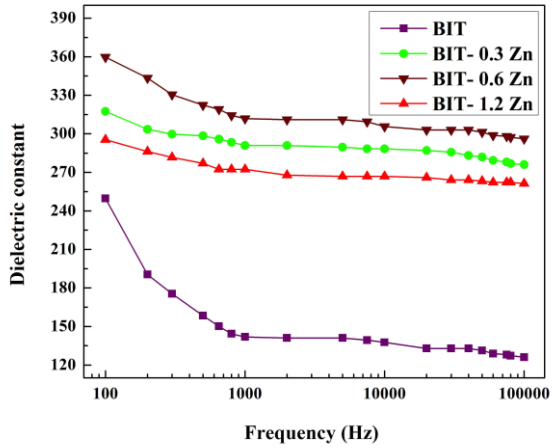

Figure 6. Frequency dependence of dielectric constant for samples measured at room temperature

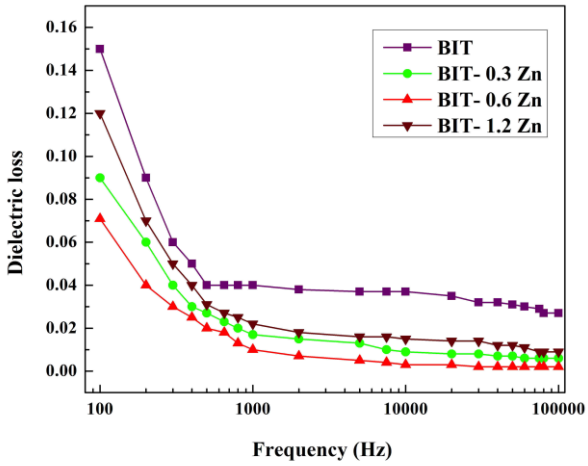

Figure 7. Frequency dependence of dielectric loss for samples measured at room temperature

Figure 8 shows the dielectric constant and dielectric loss of the samples, measured at the frequency of 1 kHz, as a function of the amount of ZnO. The results indicate a significant improvement in the dielectric properties of the BIT ceramic when using ZnO additive. Among the samples, the BIT -0.6 Zn sample demonstrates the highest dielectric constant and the lowest dielectric loss. Notably, the dielectric constant value for the BIT -0.6 Zn sample is 312, while for the BIT sample, it is 142. The dielectric loss value for the BIT sample was reduced from 0.04 to 0.01 in the BIT -0.6 Zn sample. The enhancement in the dielectric properties in the presence of ZnO nanoparticles can be attributed to higher density, lattice distortion in the crystal structure, and grain orientation [4,5].

The ac conductivity (σ_{ac}) of the dielectric materials is calculated using Equation 2 where ε_0 represents the permittivity of vacuum, ε' the permittivity of the material, $\tan\delta$ the dielectric loss, and ω ($2\pi f$) the angular frequency of the applied ac field [24]. The graph of the ac conductivity calculated from Equation 2 for the samples as a function of frequency is shown in Figure 9.

$$\sigma_{ac} = \varepsilon_0 \varepsilon' \omega \tan\delta \quad (2)$$

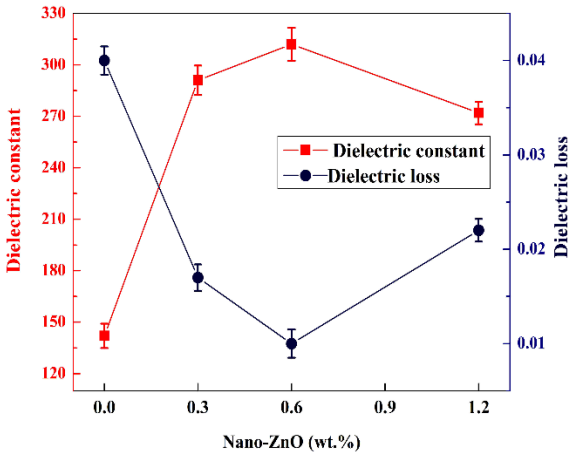

Figure 8. Dielectric constant and dielectric loss of samples as a function of ZnO amount measured at 1 kHz

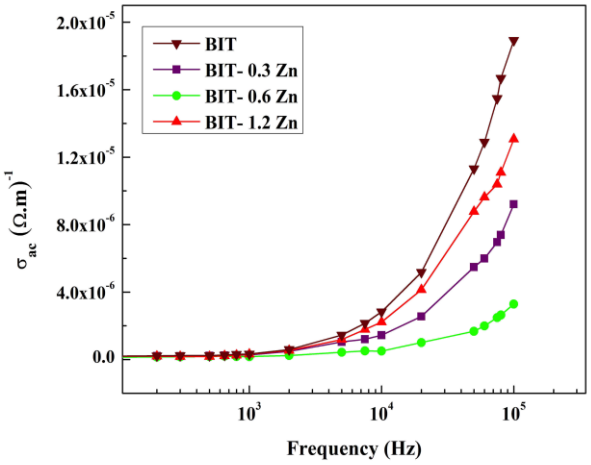

Figure 9. Frequency dependence of the ac conductivity for samples

The ac conductivity values for all samples remain constant at low frequencies and represent the dc conductivity of the dielectric material. The ac conductivity increases as the applied field frequency increases. Beyond a certain frequency known as the hopping frequency (occurring at around 10^4 Hz for the samples), there is a significant increase in the ac conductivity, indicating the presence of a frequency hopping region. This behavior can be justified by the Maxwell-Wagner surface model according to which, charge carriers become trapped at grain boundaries, structural defects, and imperfections within the material, impeding their free movement. As the frequency increases, the charge carriers gain sufficient energy to overcome these barriers, resulting in a substantial increase in ac conductivity [10,24]. According to Figure 9, addition of ZnO nanoparticles leads to a decrease in the ac conductivity of the BIT ceramic. The BIT-0.6 Zn sample had the lowest ac conductivity values. According to Equation 2, the ac conductivity is determined by the permittivity and dielectric loss of the samples. Followed by addition of ZnO nanoparticles, the permittivity increases while the dielectric loss decreases, resulting in a reduction in ac conductivity. Therefore, the impact of ZnO nanoparticles on reducing the dielectric loss is more significant than the increase in the permittivity, hence a decrease in ac conductivity. This decrease, which is indicative of an increase in the electrical resistance, can contribute to the enhancement of dielectric properties.

Figure 10 represents the variations in the piezoelectric coefficient (d_{33}) for the samples as a function of the amount of zinc oxide nanoparticles. A significant limitation of BIT ceramics is their low piezoelectric coefficient. According to the obtained results, addition of zinc oxide nanoparticles improves the piezoelectric coefficient of the BIT ceramic. Figure 11 shows the polarization hysteresis loop for the BIT and BIT -0.6 Zn samples. It also indicates that the saturation and remnant polarization values for the BIT -0.6Zn sample are 12 μC/cm^2 and 4.25 μC/cm^2, respectively while for the BIT sample, they are 8.5 μC/cm^2 and 2.32 μC/cm^2, respectively. The coercive field value for both samples is obtained as approximately 14 kV/cm. According to Equation 1, substituting Zn^{2+} ions at the B site creates oxygen vacancies which, along with Zn^{2+} ions, induce local distortions in the perovskite unit cells. Additionally, the electric dipoles from $Zn_{Ti}^{''}$-$V_O^{\bullet\bullet}$ defects and elastic dipoles from the disorder of the unit cell caused by oxygen vacancies are formed. These dipoles have good excitation capabilities that contribute to the improvement in the dielectric properties. Further, the disorder of the unit cell facilitates the alignment of ferroelectric domains during polarization, resulting in improved piezoelectric and ferroelectric properties [15, 16].

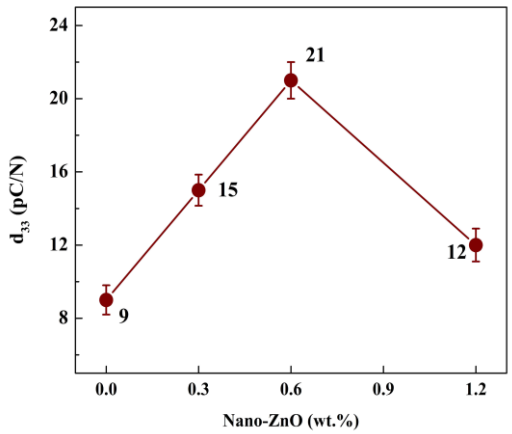

Figure 10. Piezoelectric coefficient of samples as a function of the amount of ZnO

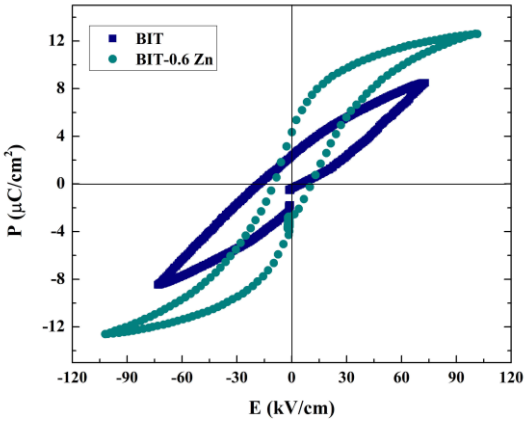

Figure 11. Polarization hysteresis loop for BIT and BIT -0.6 Zn samples

4. CONCLUSIONS

This study investigated the impact of zinc oxide nanoparticles as the sintering aid (at concentrations of 0.3, 0.6, and 1.2 wt %) on different properties of bismuth titanate ceramic. The findings of this study were summarized as follows:

1. To achieve high-density samples, the optimal sintering conditions required were determined as the temperature of 1075 °C, holding time of 2 hours, and heating rate of 5 °C/min.
2. Incorporation of ZnO nanoparticle sintering aid enhanced the densification of the BIT ceramic.
3. Addition of 1.2 wt% ZnO resulted in the formation of a secondary phase (Zn_2TiO_4) in the BIT ceramic.
4. The ZnO sintering aid additive modified the grain growth orientation in the microstructure of the BIT ceramic.
5. The ZnO sintering aid significantly increased the dielectric constant and decreased the dielectric loss of the BIT ceramic. The sample with 0.6 wt% ZnO exhibited a maximum dielectric constant of 312,

which was approximately twice that of the pure BIT sample at the frequency of 1 kHz.

6. A high piezoelectric coefficient of 21 pC/N was observed in the sample with 0.6 wt% ZnO, which was more than twice that of the pure BIT sample.
7. The remnant polarization value of the sample with 0.6 wt% ZnO, 4.2 μC/cm^2, was approximately 82% higher than that of the pure BIT sample.

REFERENCES

1. Jiang, D., Zhou, Z., Liang, R., Dong, X., "Highly orientated $Bi_4Ti_3O_{12}$ piezoceramics prepared by pressureless sintering", ***Journal of the European Ceramic Society,*** Vol. 41(2), (2021),1244-1250. https://doi.org/10.1016/j.jeurceramsoc.2020.09.039
2. Lavado, C., Stachiotti, M. G.,"Fe^{3+}/Nb^{5+} co-doping effects on the properties of Aurivillius $Bi_4Ti_3O_{12}$ ceramics", Journal ***of Alloys and Compounds,***Vol.731, (2018),914-919. https://doi.org/10.1016/j.jallcom.2017.10.112
3. Badge, S. K., Deshpande, A. V., "Study of dielectric and ferroelectric properties of Bismuth Titanate ($Bi_4Ti_3O_{12}$) ceramic prepared by sol-gel synthesis and solid state reaction method with varying sintering temperature", ***Solid State Ionics***, Vol. *334*, (2019), 21-28. https://doi.org/10.1016/j.ssi.2019.01.028
4. Hong, S. H., Trolier-McKinstry, S., Messing, G. L., "Dielectric and electromechanical properties of textured niobium-doped bismuth titanate ceramics", ***Journal of the American Ceramic Society***, Vol. *83*(1), (2000), 113-118. https://doi.org/10.1111/j.1151-2916.2000.tb01157.x
5. Xie, X., Zhou, Z., Liang, R., Dong, X., "Significantly enhanced piezoelectric performance in $Bi_4Ti_3O_{12}$-based high-temperature piezoceramics via oxygen vacancy defects tailoring", ***Journal of Materiomics***, Vol. *7*(1), (2021),59-68. https://doi.org/10.1016/j.jmat.2020.08.003
6. Liu, J., Shen, Z., Yan, H., Reece, M. J., Kan, Y., Wang, P., "Dielectric, piezoelectric, and ferroelectric properties of grain-orientated $Bi_{3.25}La_{0.75}Ti_3O_{12}$ ceramics", ***Journal of applied physics***, Vol. 102(10), (2007), 104107. https://doi.org/10.1063/1.2812697
7. Zhang, H., Yan, H., Zhang, X., Reece, M.J., Liu, J., Shen, Z., Kan, Y. Wang, P., "The effect of texture on the properties of $Bi_{3.15}Nd_{0.85}Ti_3O_{12}$ ceramics prepared by spark plasma sintering", ***Materials Science and Engineering:A***, Vol. 475, (2008), 92-95. https://doi.org/10.1016/j.msea.2006.12.144
8. Zhang, H., Ke, H., Luo, H., Guo, P., Yang, B., Jia, D., Zhou, Y., "Effects of spark plasma sintering on ferroelectricity of $0.8Bi_{3.15}Nd_{0.85}Ti_3O_{12}$-0.2 $CoFe_2O_4$ composite ceramic", ***Journal of the European Ceramic Society***, Vol. 38(5), (2018), 2353-2359. https://doi.org/10.1016/j.jeurceramsoc.2018.01.011
9. Bokolia, R., Thakur, O. P., Rai, V. K., Sharma, S. K., Sreenivas, K. J. C. I., "Dielectric, ferroelectric and photoluminescence properties of Er^{3+} doped $Bi_4Ti_3O_{12}$ ferroelectric ceramics", ***Ceramics International***, Vol. 41(4),(2015),6055-6066. https://doi.org/10.1016/j.ceramint.2015.01.062
10. Subohi, O., Bowen, C. R., Malik, M. M., Kurchania, R., "Dielectric spectroscopy and ferroelectric properties of magnesium modified bismuth titanate ceramics", ***Journal of Alloys and Compounds***, Vol. 688, (2016), 27-36. https://doi.org/10.1016/j.jallcom.2016.07.173
11. Hou, J., Kumar, R. V., Qu, Y., Krsmanovic, D., "B-site doping effect on electrical properties of $Bi_4Ti_{3-2x}Nb_xTa_xO_{12}$ ceramics", ***Scripta Materialia***, Vol. 61,(2009),664-667. https://doi.org/10.1016/j.scriptamat.2009.06.012
12. Badge, S. K., Deshpande, A. V., "Effect of vanadium doping on structural, dielectric and ferroelectric properties of bismuth titanate ($Bi_4Ti_3O_{12}$) ceramics", ***Ceramics International***, Vol. 45, (2019), 15307-15313. https://doi.org/10.1016/j.ceramint.2019.05.021
13. Chen, X. Q., Yang, F. J., Cao, W. Q., Wang, H., Yang, C. P., Wang, D. Y., Chen, K., "Enhanced multiferroic characteristics in Fe-doped $Bi_4Ti_3O_{12}$ ceramics," ***Solid state communications***, Vol. 150, (2010),1221-1224. https://doi.org/10.1016/j.ssc.2010.04.002
14. Chen, Y., Pen, Z., Wang, Q., Zhu, J., "Crystalline structure, ferroelectric properties, and electrical conduction characteristics of W/Cr co-doped $Bi_4Ti_3O_{12}$ ceramics," ***Journal of alloys and compounds***, Vol. 612, (2014),120-125. https://doi.org/10.1016/j.jallcom.2014.05.136
15. Lee, Y. C., Lee, T. K., Jan, J. H., "Piezoelectric properties and microstructures of ZnO-doped $Bi_{0.5}Na_{0.5}TiO_3$ ceramics", ***Journal of the European ceramic society***, Vol. 31, (2011), 145-3152. https://doi.org/10.1016/j.jeurceramsoc.2011.05.010
16. Villegas, M., Jardiel, T., Caballero, A. C., "Effect of ZnO on the microstructure and electrical properties of WO_3–$Bi_4Ti_3O_{12}$ ceramics", ***Journal of the European Ceramic Society***, Vol. 29, (2009), 737-742. https://doi.org/10.1016/j.jeurceramsoc.2008.06.026
17. Hayati, R., Bazargan-Lari, R., Zamani, A., Balak, Z., "Studying the effects of nano sintering additives on microstructure and electrical properties of potassium-sodium niobate piezoceramics," ***Advanced Ceramics Progress***, Vol.4,(2018),7-15. 10.30501/ACP.2018.91120
18. Slimani, Y., Selmi, A., Hannachi, E., Almessiere, M. A., Baykal, A., Ercan, I., "Impact of ZnO addition on structural, morphological, optical, dielectric and electrical performances of $BaTiO_3$ ceramics," ***Journal of Materials Science: Materials in Electronics,*** Vol. 30, (2019), 9520-9530. https://doi.org/10.1007/s10854-019-01284-2
19. Chou, C. S., Wu, C. Y., Yang, R. Y., Ho, C. Y., "Preparation and characterization of the bismuth sodium titanate ($Na_{0.5}Bi_{0.5}TiO_3$) ceramic doped with ZnO", ***Advanced Powder Technology***, Vol. 23, (2012), 358-365. https://doi.org/10.1016/j.apt.2011.04.015
20. Rahaman, M. N., (2017), *Ceramic processing and sintering*. CRC press, https://doi.org/10.1201/9781315274126
21. Xie, S., Xu, J., Chen, Y., Jiang, L., Tan, Z., Nie, R., Xu, Q., Wang, Q. Zhu, J., "Poling effect and sintering temperature dependence on fracture strength and fatigue properties of bismuth titanate based piezoceramics', ***Ceramics International***, Vol. 44, (2018), 20432-20440. https://doi.org/10.1016/j.ceramint.2018.08.037
22. Badge, S. K., & Deshpande, A. V. "Effect of pressure of pelletization on dielectric properties of Bismuth Titanate prepared by sol-gel synthesis", ***Advanced Powder Technology***, Vol. 29, (2018), 555-562. https://doi.org/10.1016/j.apt.2017.11.011
23. Preethi, T. M., Ratheesh, R., "Synthesis and dielectric properties of a new class of $MX_6Ti_6O_{19}$ (M= Ba, Sr and Ca; X= Mg and Zn) ceramics", ***Materials Letter***s, Vol. 57, (2003), 2545-2552. https://doi.org/10.1016/S0167-577X(02)01309-5
24. Mesrar, M., Elbasset, A., Echatoui, N. S., Abdi, F., Lamcharfi, T. D., "Studies of structural, dielectric, and impedance spectroscopy of KBT-modified sodium bismuth titanate lead-free ceramics", ***ACS omega***, Vol. *7*, (2022), 37142-37163. https://doi.org/10.1021/acsomega.2c03139

Advanced Ceramics Progress

Volume 9, Number 3, Summer 2023

CONTENTS

Journal Home Page: www.acerp.ir